Brigham Young University
BYU ScholarsArchive

All Theses and Dissertations

2013-03-22

Experimental Analysis of Energy-Based Acoustic Arrays for Measurement of Rocket Noise Fields

Jarom Henry Giraud
Brigham Young University - Provo

Follow this and additional works at: https://scholarsarchive.byu.edu/etd

 Part of the Astrophysics and Astronomy Commons, and the Physics Commons

BYU ScholarsArchive Citation

Giraud, Jarom Henry, "Experimental Analysis of Energy-Based Acoustic Arrays for Measurement of Rocket Noise Fields" (2013). *All Theses and Dissertations*. 3950.
https://scholarsarchive.byu.edu/etd/3950

This Thesis is brought to you for free and open access by BYU ScholarsArchive. It has been accepted for inclusion in All Theses and Dissertations by an authorized administrator of BYU ScholarsArchive. For more information, please contact scholarsarchive@byu.edu, ellen_amatangelo@byu.edu.

Experimental Analysis of Energy-Based Acoustic Arrays for Measurement of Rocket Noise Fields

Jarom H. Giraud

A thesis submitted to the faculty at
Brigham Young University
in partial fulfillment of the requirements for the degree of

Master of Science

Kent L. Gee, Chair
Scott D. Sommerfeldt
Jonathan D. Blotter

Department of Physics and Astronomy

Brigham Young University

March 2013

Copyright © 2013 Jarom H. Giraud

All Rights Reserved

ABSTRACT

Experimental Analysis of Energy-Based Acoustic Arrays for
Measurement of Rocket Noise Fields

Jarom H. Giraud
Department of Physics and Astronomy, BYU
Master of Science

Microphone arrays are useful for measuring acoustic energy quantities (e.g. acoustic intensity) in the near-field of a full-scale solid rocket motor. Proper characterization of a rocket plume as a noise source will allow for more accurate predictions in engineering models that design for protection of structures, payloads and personnel near the rockets. Acoustic intensity and energy density quantities were measured in three rocket noise fields and have shown that the apparent source region of the rocket becomes smaller and moves upstream as frequency increases. Theoretical results accounting for some scattering and finite-difference errors arising in these types of energy-based measurements have been previously discussed by other authors. This thesis includes results from laboratory experiments which confirm some of this previous theoretical work as well as gives insight into the physical limitation of specific microphone array designs. Also, calibrations for both magnitude and directional response of the microphones are demonstrated. Of particular interest is the efficacy of phase calibration of array microphones for the low-frequency regime below 200 Hz.

Keywords: acoustics, intensity, energy density, low-frequency, calibration, rocket noise

ACKNOWLEDGMENTS

Just as the lamp gives us light and we praise the invention of electricity for illuminating our dark nights, I want to recognize that without the supportive and driving forces in my life, this thesis would be dim and incomplete. My wife, Teri is my biggest supporter. She encouraged me as hope ran low, helped me drive for success by teaching the power of setting goals, moved my family across the country so I would have more time to work, and relentlessly encouraged me to succeed. Kent Gee has been my mentor, instructor, taskmaster, boss, advisor and friend. His infectious enthusiasm for learning has inspired me in my studies of acoustics and he has helped greatly improve my abilities as a researcher. This thesis would not have been possible without his belief in my abilities and willingness to give up sleep to help his student succeed. Scott Sommerfeldt and Jonathan Blotter have been supportive committee members and offered valuable insights into my research and the contents of this thesis. Fellow students, Derek Thomas, Curtis Wiederhold, Alan Wall, Troy Taylor and many others have helped me understand my research and acquire the data used in these analyses. This work was done in conjunction with Blue Ridge Research and Consulting (BRRC) and NASA who are also working to better understand rocket noise environments. For all these supporters, my abilities, inspiration and opportunities which were a part of this thesis, I am grateful to God.

Contents

List of Figures

1 Introduction

1.1 Overview

Large solid rocket motors, such as those used for sending equipment and personnel into space, generate intense acoustic levels during firing. The most common acoustic models for rocket noise prediction are the distributed source methods described in NASA report SP-8072[1]. As shown in Figure 1.1, these models attempt to predict rocket acoustics by modeling the exit plume as a series of discrete sources with an assigned amplitude and frequency content. The accuracy of these models is directly tied to the present-day understanding of noise generation in a rocket plume as a series of distributed sources. Recently there has been movement to improve the modeling and measurement techniques used in predicting acoustic loads on launch vehicles and nearby structures[2,3]. These improvements have included shifting the source region in the existing model and developing computational fluid dynamic models to predict both near and far-field acoustics of a rocket source.

Contained within this thesis is an energy-based acoustic analysis of the near-field of multiple solid rocket motors. This research gives insight into the field generated and may be used by others to provide direction in how current prediction models and measurement methods may be improved.

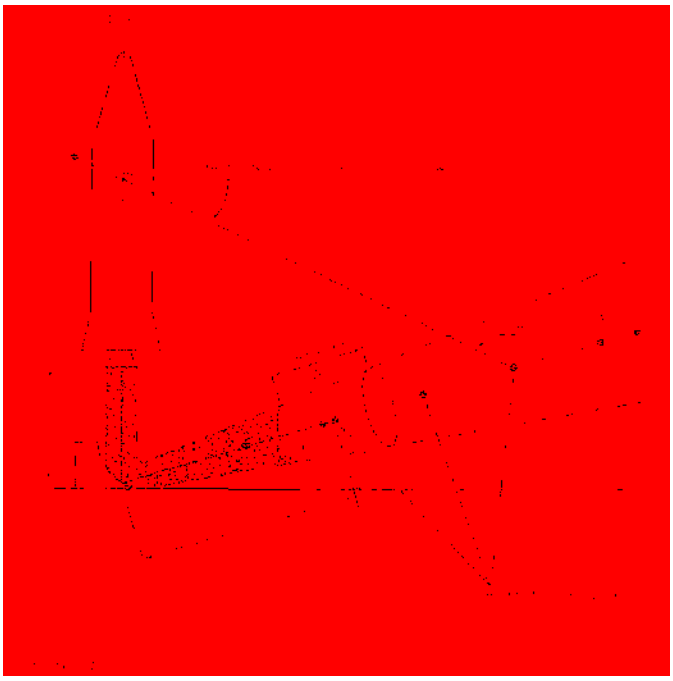

Figure 1.1. Image from NASA SP8072[1] depicting how a rocket plume is sliced into segments which are added together to predict the noise at some location on (or near) the launch vehicle.

In the acoustic near field of a source, pressure measurements at a single point are subject to interference effects and may give amplified or reduced levels that do not characterize the true amount of acoustic energy in the region. Intensity may be measured accurately in the near-field of a source and also has the advantage of showing the direction from whence the sound came. For an extended or distributed source, such as a rocket plume, the acoustic intensity vector will point in the average direction of all the incident energy. Energy-based acoustic measurements, particularly acoustic intensity, may give insight into the best way to assign frequency and amplitude content for each of the slices, as in Figure 1.1, to improve the accuracy of the prediction. Other energy-based metrics may also help researchers to better understand the environment and flow of energy near a solid rocket motor.

The use of intensity measurements to generate acoustic field maps and localize source regions of aeroacoustic sources is relatively uncommon[4,5]. Jaeger[6] explored these types of measurements for a 10.1cm unheated subsonic jet by traversing a two-dimensional intensity array parallel to the plume at multiple distances away from the plume. Their work confirmed relative source locations between high and low frequencies and also looked at directivity of the intensity vector as a function of frequency. More recently, Krueger[7] has compiled an intensity vector map of a F-22A Raptor aircraft using intensity arrays and near-field acoustical holography techniques.

This thesis contains experimental analysis for acoustic energy arrays in both controlled and field test environments. Chapter 2 is concerned with experimental variations in magnitude and phase response between microphones in the array that result in low-frequency errors. A method for calibration and experimental confirmation is contained in this same chapter. Wiederhold[8] discussed theoretical limitations of multi microphone arrays and his results are used in Chapter 3 to investigate experimental error and assess our ability to calibrate the arrays at high frequencies. The experimental data of Chapter 3 is then analyzed in Chapter 4 to take a preliminary look at how well the arrays measure energy density quantities. The results of Chapter 4 will aid in understanding the results of the remaining chapters.

Presented in Chapter 5 and Chapter 6 are the acoustic intensity, and other energy-based acoustic metrics, obtained near three solid rocket motor static test firings. These tests have given us insight into the challenges of taking array-based measurements in a rocket noise field and raised questions regarding the limitations of the microphone arrays in measuring various acoustic quantities.

1.2 Contributions

Energy-based acoustic measurements of rocket noise fields are rare, as are the instruments which are capable of accurately acquiring data in the extreme environments of such fields. Although not new in concept, the work in this thesis gives future researchers insight into the limitations of using 4-microphone tetrahedral arrays and the finite-difference processing method to obtain rocket noise data. The limitations discussed will be useful in developing new arrays and ensuring that the arrays are correctly sized to obtain the data at the desired frequencies in field. Chung and Blaser's[9] transfer function procedure for calibration of multiple microphones is explained and is shown to improve the low-frequency accuracy of the arrays.

A particularly significant contribution of this work are the vector maps of acoustic intensity measured along the shear layer of three solid rocket motor plumes. More insight into source distribution, location and directivity is gained from these maps and related ray tracing diagrams. Also of use are the energy density maps which help describe the fields in terms of near-field and far-field measurements. Appendix A contains the formulations of the finite-difference methods used in the processing of the data in this thesis.

To the reader: What is labeled as "Chapter 2" in this thesis is a paper written for the 162nd meeting of the Acoustical Society of America in San Diego, California on November 3rd 2011. This paper was part of a special session on launch vehicle noise and has been written to be a "stand-alone" document. The results and discussions of this paper will be of interest to those who continue to research the design and implementation of broadband acoustic intensity arrays. Having been completed last chronologically, the results of this analysis have not been applied to the remaining chapters of this thesis.

2 Low-Frequency Calibration of a Multidimensional Acoustic Intensity Probe for Application to Rocket Noise

Jarom H. Giraud[1], Kent L. Gee[1], Scott D. Sommerfeldt[1], R. Troy Taylor[1], and Jonathan D. Blotter[2]

[1]Dept. of Phys. and Astronomy, Brigham Young Univ., Eyring Sci. Ctr., Provo, UT 84602, kentgee@byu.edu

[2]Dept. of Mech. Eng, Brigham Young Univ., Provo, UT, 84602

Abstract. Microphone arrays used to measure acoustic intensity and other energy quantities traditionally have low-frequency bandwidth limitations (e.g., below 100 Hz) thereby excluding the lowest, and in some cases, the most energetic frequencies generated by large rocket motors. At these low frequencies, the phase and magnitude mismatch between microphones becomes greater and the acoustic phase separation between any two microphones becomes smaller, resulting in more error in estimating the pressure gradients. To investigate the low-frequency response of an acoustic intensity probe, a turntable is used to rotate a four-microphone probe in a low-frequency noise field. An experimental assessment of the bandwidth is given for both magnitude and directional response down to approximately 40 Hz. The effectiveness of a microphone interchange calibration technique to remove amplitude and phase mismatch and increase the usable bandwidth of the probe is also discussed.

2.1 Background

Large solid rocket motors, such as those used for sending equipment and personnel into space, generate intense acoustic levels during firing. For these larger motors (nozzle diameters ~1 to 3.5 m) low frequencies, on the order of tens of Hz, dominate the acoustic spectrum and peak pressures approach that of the atmosphere near the plume. These acoustic loads are capable of damaging near-by structures and are necessarily accounted for in the engineering of these launch vehicles and support structures. A typical spectral response near one of these motors is shown in Figure 2.1. Notice the amount of acoustic energy at frequencies as low as 10 Hz. This source spans the entire audible range at levels over 80 dB and has the most acoustic energy below 100 Hz, which is a difficult region to accurately measure acoustic intensity.

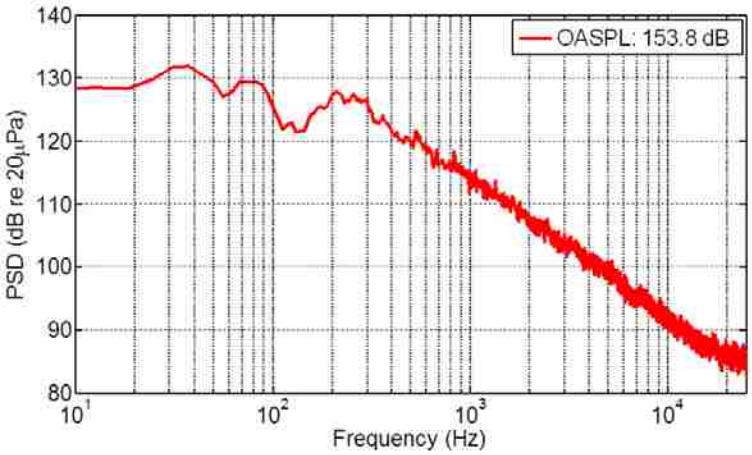

Figure 2.1.Typical spectra from a GEM-60 solid rocket motor (1.09 m nozzle diameter) at a location ~28 nozzle diameters downstream and ~18.5 nozzle diameters from the axis of firing.

The most common acoustic models for rocket noise prediction are the distributed source methods described in NASA report SP-8072[1]. These models attempt to predict rocket acoustics by modeling the exit plume as a series of discrete sources with an assigned amplitude and frequency content. The accuracy of this model is directly tied to the present day understanding

of noise generation in a rocket plume. A goal of this research is to improve our accuracy of measuring acoustic intensity at both low and high frequencies to better understand and describe noise generation in the rocket plume and thereby improve these models.

The so-called "p-p" method for measuring acoustic intensity utilizes an approximation of the particle velocity from two pressure microphones and their average pressures to calculate acoustic intensity. This method relies on the accurate measurement of both magnitude and phase characteristics of an acoustic source.[10,11] While high-frequency intensity measurements are limited by scattering and increased errors in approximating collocated pressure and velocity, low-frequency measurements are limited by frequency response characteristics of the microphones used in the measurement. This paper describes the problem of inaccurate low-frequency microphone response, an approach for improving it and experimental verification of the method. Also included are suggestions for future research in this area.

Figure 2.2 shows a typical arrangement for performing the p-p method in one dimension. In this figure, two microphones separated by a distance, $\boldsymbol{d}$, measure acoustic intensity along a single dimension $\hat{\boldsymbol{x}}$ by approximation of the acoustic pressure and particle velocity at a point exactly between the two sensors. As the spacing between sensors approaches a half wavelength, the approximation used to estimate the acoustic pressure at the geometric center of the array degrades. The closer two microphones are spaced, the higher in frequency the probe can measure accurately. However, as sensors are placed closer together, the low-frequency response becomes subject to phase mismatch between sensors as this mismatch becomes large relative to the acoustic phase separation of the sensors. Amplitude mismatch between sensors also becomes more influential as separation distance is decreased. To combat this and obtain a broadband

measurement, multiple microphone spacings[12,13] are used during repeated measurements for repeatable measurements such as machine or room noise.

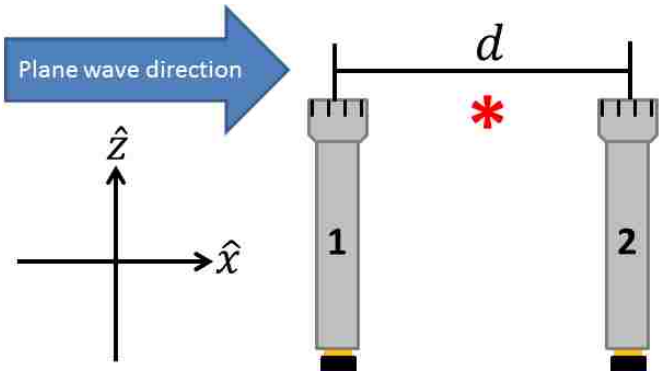

Figure 2.2. A typical setup for the p-p method.

When attempting to acquire broadband noise radiation data from a rocket motor, it is difficult (or impossible) to repeat the test after adjusting the spacing. As an alternative, an option is to place the sensors as close together as needed to obtain the high end of the desired bandwidth and try to minimize the low-frequency effects of phase and magnitude mismatch by means of a calibration. Maximizing bandwidth is a balance between microphone spacing, microphone frequency response, frequencies of interest, acceptable error and atmospheric considerations including sound speed and homogeneity of the field.

Microphones have mechanical, electrical and acoustical components that behave as inductive, capacitive or resistive elements. The combination of these components gives rise to high-pass filtering effects which causes roll-off in both magnitude and phase at low frequencies. Minor adjustments in venting, volume behind the microphone back plate, and other electronic, mechanical and acoustical discrepancies between sensors will alter this roll-off.[14] As a rule, no

two manufactured microphones will have identical magnitude and phase response; this contributes to measurement uncertainty or error.

Consider two microphones used to perform the p-p intensity measurement with a separation distance of 2.54 cm. At 13.72 kHz and a sound speed of 343 m/s, the wavelength is 2.54 cm and the acoustic phase difference between the two microphones is 360°. As frequency decreases, this acoustic phase difference between microphones also decreases, as seen in Figure 2.3. For comparison, the phase error between two typical (un-matched) 6.35mm microphones is also included in this figure. In this two-microphone example, the microphones are aligned with preamps parallel to $\hat{z}$ and the separation is only along $\hat{x}$, as in Figure 2.2. The direction of plane wave propagation is also along the $\hat{x}$ direction.

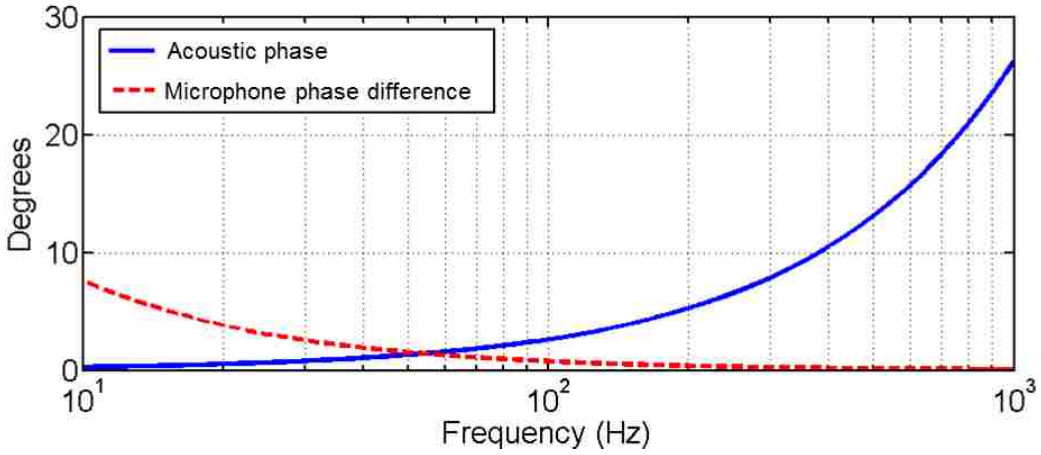

Figure 2.3. Representative trends of acoustic phase and the phase difference between two microphones separated by 2.54 cm. Acoustic phase difference between two microphones separated by some distance decreases proportional to frequency. The electro-mechanical phase difference between two similar microphones becomes large at low frequencies.

One may purchase manufactured "magnitude and phase matched" microphone pairs with variations in phase response measured as approximately < 0.2° for 20 Hz to 1 kHz and

magnitude variations of < 0.2 dB for 20 Hz to 2 kHz[15]. For a two-microphone p-p probe it is the relative phase and magnitude error between sensors that determines the low-frequency end of the probe bandwidth. The effect of a constant phase error over frequency for a microphone spacing of 2.54 cm is seen in Figure 2.4.

Assuming two microphones are perfectly matched in magnitude response but have a phase difference of ϕ, the intensity magnitude error as a function of frequency can be written[16] as

$$Error(Intensity) = 10\log_{10}\left[\frac{\sin(kd-\phi)}{kd}\right]. \quad (2.1)$$

This relationship is found by deriving acoustic intensity via the p-p method and modifying the phase of one sensor by kd, (wavenumber times microphone separation distance) the acoustic phase separation, and ϕ, the assumed phase error between microphones. Figure 2.4 shows this relationship for the case of the one-dimensional plane wave as in Figure 2.2.

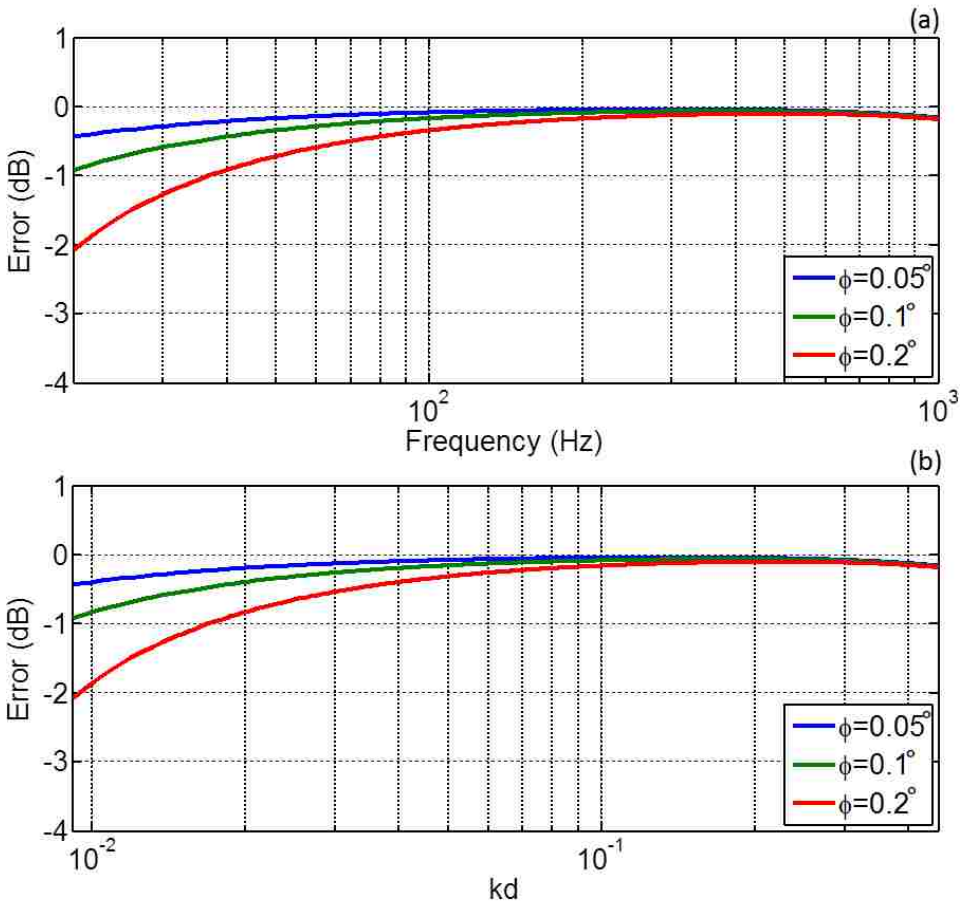

Figure 2.4. Error in measuring the intensity magnitude for various phase errors, ϕ, between sensors (a) For two microphones separated by $d = 2.54$ cm. (b) For a dimensionless quantity kd, which relates frequency and separation distance (no longer fixed at 2.54 cm).

Although Figure 2.4 (a) is presented with frequency (in Hz) as the independent variable, this plot is easily transformed to the non-dimensionalzed variable, kd (wavenumber times separation distance), as shown in Figure 2.4(b). A kd plot is useful because it allows one to determine a frequency limit for a given separation distance or determine a separation distance that allows for accurate measurement at a desired frequency.

2.2 Calibration

Any two microphones with a stable (however inaccurate) magnitude and phase response can be calibrated for use in a low-frequency intensity probe by using Chung and Blaser's switching technique.[17] This ability to calibrate (and re-calibrate) microphone sets is advantageous for use in measuring rocket noise because the response may be checked, after subjecting the sensors to the harsh environment created by a rocket, without sending the transducer back to the manufacturer. Also, the calibration can be performed before the test using a simple apparatus.

To remove the effects of magnitude and phase error between sensors, there are multiple calibration approaches using transfer functions.[18-21] The method employed in this thesis is the switching technique calibration by Chung and Blaser.[17] However, this calibration is obtained in the lab and not in-situ, such as demonstrated by Chung in other work.[19] Being able to calibrate prior to the actual measurement is essential in making rocket noise measurements due to the inability of calibrating *in situ* with the source (rocket motor) to be tested.

The switching technique utilizes the geometric mean of two transfer functions to remove the effect of the field on the calibration. Consider two similarly shaped microphones in a sound field. Each microphone has a separate output, $\hat{e}_{I,1}$ and $\hat{e}_{I,2}$, (see Figure 2.5 for definitions) related to the acoustic pressure, microphone response, and electronic response. The ratio of the outputs is a transfer function, H, between microphones. This relationship may be processed in the frequency domain as a ratio of cross-spectra, G,

$$H_{I,12} = \frac{\hat{e}_{I,2}}{\hat{e}_{I,1}} = \frac{G_{I,12}}{G_{I,11}}. \tag{2.2}$$

If the locations of these sensors are exactly reversed, as in Figure 2.5, and the remainder of the measurement field remains unchanged, a second measurement and resulting transfer function may be obtained as

$$H_{II,12} = \frac{\hat{e}_{II,2}}{\hat{e}_{II,1}} = \frac{G_{II,12}}{G_{II,11}}. \tag{2.3}$$

Then, by taking the geometric mean of the two transfer functions obtained, a new transfer function is obtained that relates the two microphone responses by

$$H_{cal,12} = \sqrt{H_{II,12}H_{I,12}}. \tag{2.4}$$

To apply the calibration, one then multiplies $H_{cal,12}$ by $\hat{e}_{I,2}$ and the p-p intensity method may be performed in the usual fashion. This method modifies the response of the second microphone to match what the first microphone would have measured in the same location with the same stimulus. This method can be used to relatively calibrate any number of microphones in an array to one common reference.

Figure 2.5 shows visually how the desirable frequency response function $H_{cal,12}$ is obtained by means of ratios of cross spectra, G, or microphone output, $\hat{e}$.

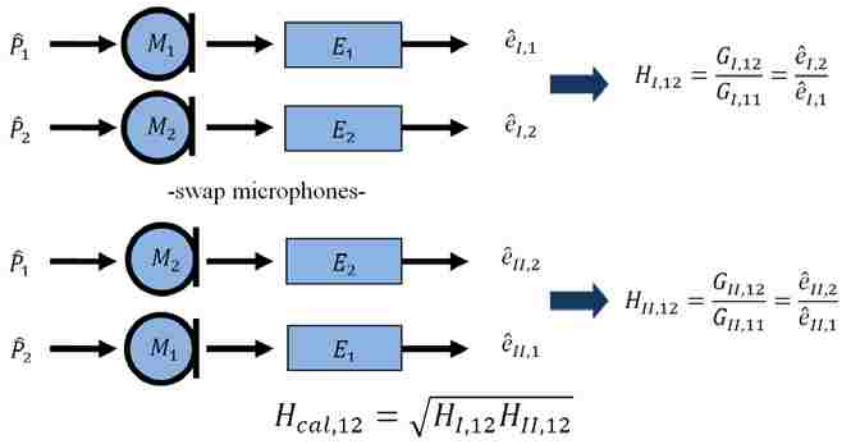

Figure 2.5. The process of finding a relative calibration between two microphones M_1 and M_2 with electronic responses E_1 and E_2 from pressure stimuli of $\hat{P}_1$ and $\hat{P}_2$.

Two laboratory G.R.A.S type 40BE free-field microphones with 26CB type preamplifiers were calibrated multiple times using the method depicted in Figure 2.5 to determine the transfer

function calibration. A G.R.A.S. 42 AE type low-frequency calibrator was used as an acoustic source because of the ease by which the exact switch of sensor locations is performed. Figure 2.6 shows five overlaid plots of the relative phase and relative magnitude of the calibration. It is interesting to notice that relative phase difference between the two microphones at 100 Hz is > 3°. However, the variation in phase is very small between trials, < 0.02°. We can then say that, with the calibration, these microphones are phase matched to < 0.02° for 10 Hz to 100 Hz for this exact setup. It is the similarities between trials that determine how effective the calibration is. Similar results are seen for magnitude calibration which results in a magnitude matched pair with <.06 dB difference for 10 Hz to 100 Hz.

It should be noted that slight variations in environment will affect the calibration in this frequency range and in general, calibrations are only valid for the exact conditions in which they were obtained. When attempting to calibrate for a measurement, the calibration should occur in conditions closely approximating that of the measurement. Individual microphones and microphone pairs will vary.

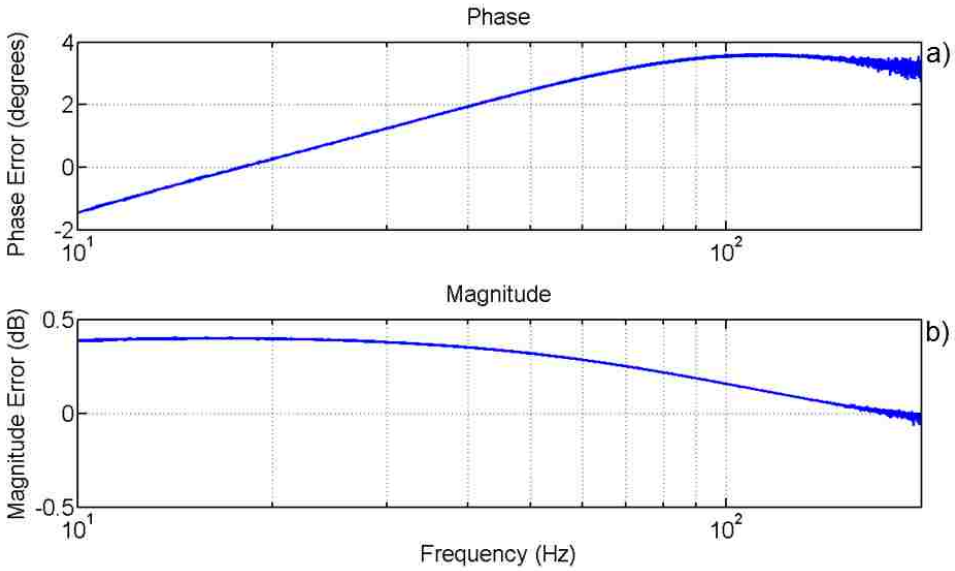

Figure 2.6. Five overlaid phase (a) and magnitude (b) calibrations relating two microphones.

As a point of interest, the relative phase and magnitudes between each of the sensors used in the experiment are given in Figure 2.7.

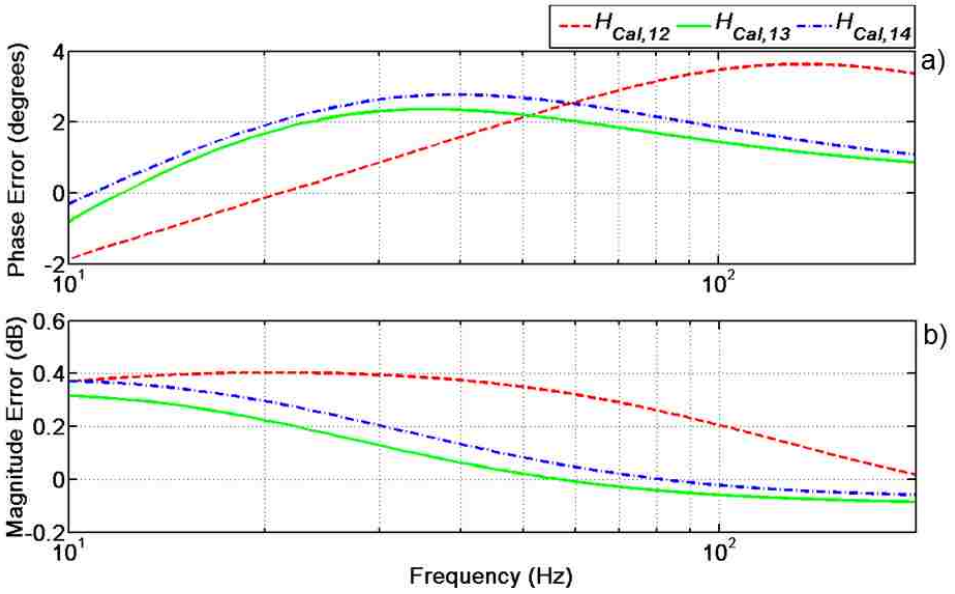

Figure 2.7. Phase (a) and magnitude (b) transfer functions for the microphones used in the experimental array.

The transfer function $H_{cal,12}$ of Figure 2.7 is for the same microphone pair, calibrated a separate day, that was shown in Figure 2.6. These two calibrations are overlaid in Figure 2.8 to more explicitly show the difference between them. The effective response of the microphone has changed slightly between calibrations and it is not simply a DC shift in magnitude; there has been a shift of the break-point, or roll off, between these calibrations. A challenge of this type of calibration is the tendency for it to drift with slight variations through the duration of the test due to atmospheric field effects. This variation over time/conditions may be equally, if not more, important than our ability to calibrate with great repeatability. In other words, the fact that we can calibrate our microphones to nearly an order of magnitude tighter than reported by the manufacturer may be useless if the test conditions vary from the calibration conditions.

In fairness to G.R.A.S., who have been very helpful in this process, it should be noted, that this particular microphone pair in Figure 2.8 shows more overall error (Δ5°, Δ0.5 dB) than is typical for these types of sensors. These sensors have been used in multiple experimental setups and it may be that frequent use and 'gentle' abuse may account for the dramatic swings in phase and magnitude response of this pair. Generally these microphones have a "flat" response down at 100 Hz.

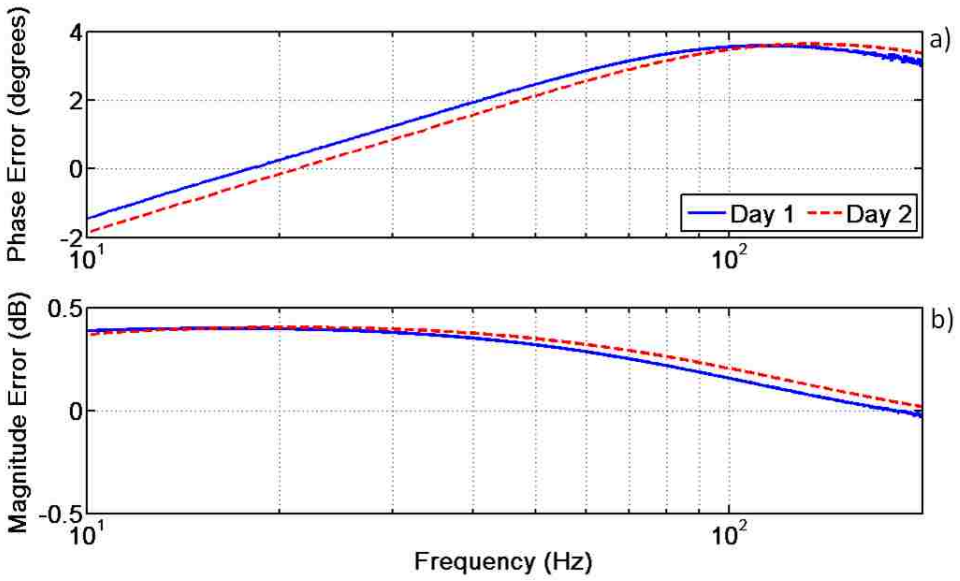

Figure 2.8. Phase (a) and magnitude (b) transfer functions for the same microphone pair on two separate days. There were approximately 2 weeks between the calibration times.

2.3 Experiment

An ideal test of the effectiveness of the calibration in improving angle and magnitude errors in measuring acoustic intensity would be to rotate an array of sensors in a plane-wave field and compare the measured intensity with the known intensity of the plane-wave field.

To approximate a plane-wave field, a loudspeaker was set far enough from a source that the diverging waves appear nearly planar over the size of our measurement area. Our frequency range of interest is on the order of tens of Hz and requires either an anechoic chamber with sufficiently deep wedges, or an outdoor measurement to eliminate a standing wave field. The experimental setup is shown in Figure 2.9. Notice that between the loudspeaker source and microphone array is a concrete sidewalk. A JBL EON 500 series subwoofer was set about 10 m from an intensity probe mounted atop an Outline ST2 turntable. White noise was generated and output by the speaker and recorded at the probe microphones via a custom LabVIEW program. After each 15-second measurement, the turntable was rotated approximately 5° and the

measurement was repeated. This process was repeated until 120° of rotation was obtained (120° matches with lines of symmetry of the intensity probe array).

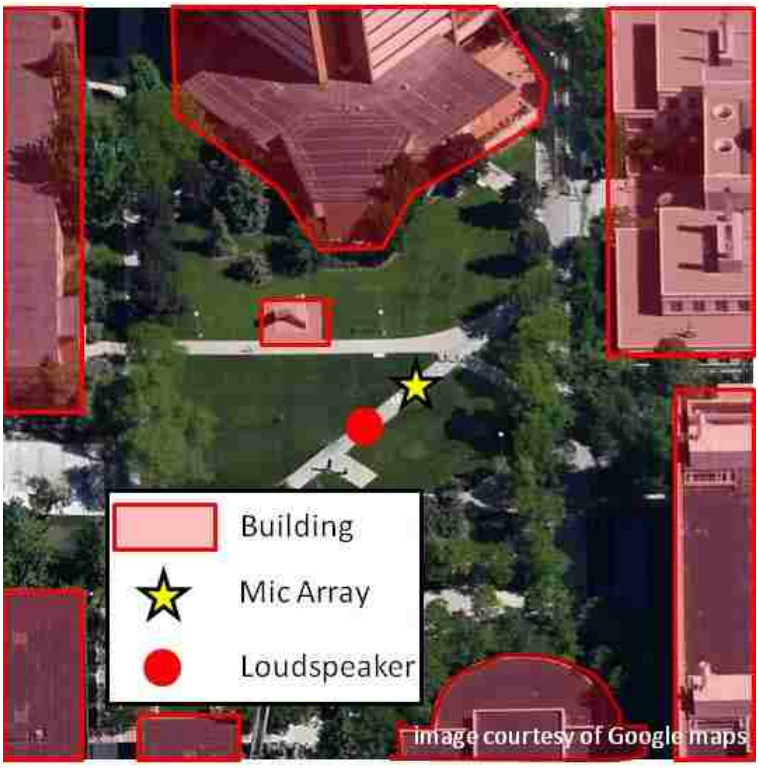

Figure 2.9. Top-down view of experimental setup.

There are known errors inherent in this experimental design. Although an outdoor location was chosen to reduce the presence of standing waves, due to the large wavelengths involved it was possible some standing waves developed between buildings. The presence of noise from building ventilation systems and passersby was occasionally present. Also, because the environment was not anechoic, there are ground/building reflections that cause interference nulls at the probe. To eliminate interference nulls in the vertical direction within the band of interest, the speaker and probe were placed low to the ground (approx. 0.5 m high). Apart from moving the ground interference null beyond the frequencies of interest, placing the subwoofer near the ground gave approximate doubling of acoustic pressure and improved the signal-to-noise ratio.

Figure 2.10 shows the average sound pressure level, SPL, for each microphone over all angles of rotation. It appears that around 30 Hz, the signal flattens out to what is presumed to be “noise”, both electronic and environmental.

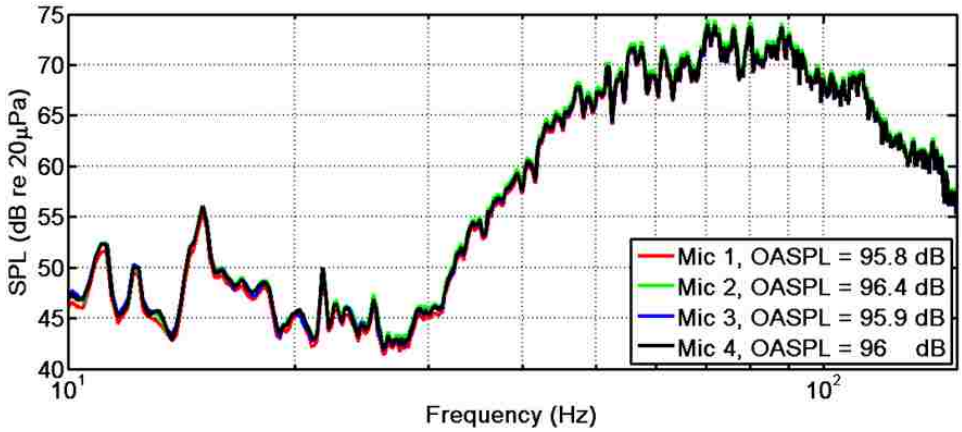

Figure 2.10. Average SPL for each of the four microphones used during the test

The intensity probe used in this experiment consisted of four 6.35 mm microphones in a tetrahedral configuration with all four of the preamps parallel to each other and the microphone diaphragms faced upwards. Figure 2.11 depicts an aluminum microphone mount which was manufactured to hold the microphones rigidly throughout the experiment such that a 2.54 cm diameter sphere would circumscribe the centers of the diaphragms.

Figure 2.11. Four 6.35 mm microphones mounted in a regular tetrahedral arrangement.

2.4 Results

The data have been analyzed both with and without the switching technique calibration applied to the results. The plots in Figure 2.12 show the directional error for un-calibrated (red) and calibrated (blue) microphones for various angles of rotation. The polar plot angles show the angle of rotation of the multidimensional probe and the rings of constant radius are the angle error. It is interesting to notice that the error at 0° and 120° rotation angle are not equal. This is because calibrations differ between the four microphones under test and the importance of each microphone in the calculation of the intensity varies with the rotation.

This analysis has multiple references to various angles. To be clear, phase error is a part of the calibration but is not otherwise reported in the results, rotational angle of the array is the angle of the polar plot, and the reported directional error (degree error of locating the source) is the concentric circles of the polar plot. For example, in Figure 2.12 for f=100 Hz at a probe rotation of 120°, there was 50° of error in locating the source. The calibration improves this result by nearly 45°.

It is easier to consider the overall effect of the calibration by looking at Figure 2.13 which depicts the average error from all measurements as a function of frequency. In this experiment

the source and receiver were spaced by approximately 10 m. At this distance, 5°, 10° and 20° error correspond to 0.87, 1.7, and 3.4 m error in estimating the location of the source. An area of future research may be to investigate the relatively smooth decrease in angle accuracy below 45 Hz for the calibrated curve. Some of the error may rise from the poor signal-to-noise ratio at these frequencies (see Figure 2.11). However, slight errors in calibration cannot yet be discounted.

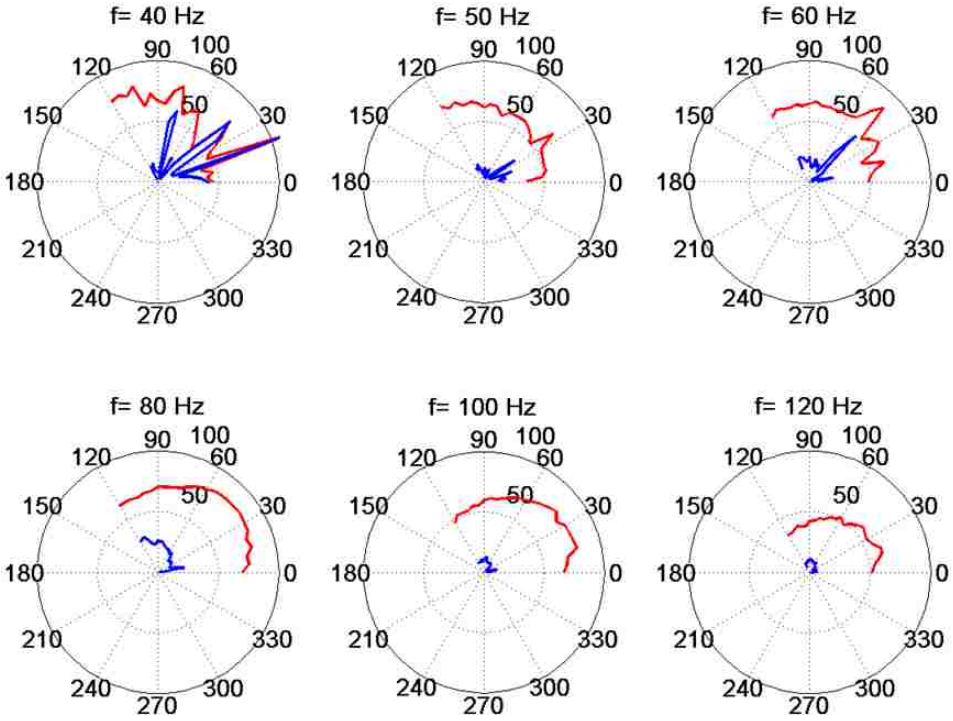

Figure 2.12. Directional errors for various angles of probe rotation for the calibrated (blue line) and un-calibrated microphones (red line).

Figure 2.13(a) shows the average angle error as a function of frequency for each of the measurements performed. As the frequency drops to about 30 Hz, the error between the calibrated and non-calibrated calculations is negligible and is centered around 90°. Below 30 Hz may be in the noise floor of the measurement as seen in Figure 2.10. The maximum error one

can achieve is 180° (pointing directly away from the source) and the minimum error is 0° (pointing directly towards the source), it stands to reason that the average error of this ”noisy” data be in the middle at 90° (pointing neither towards or away from the source).

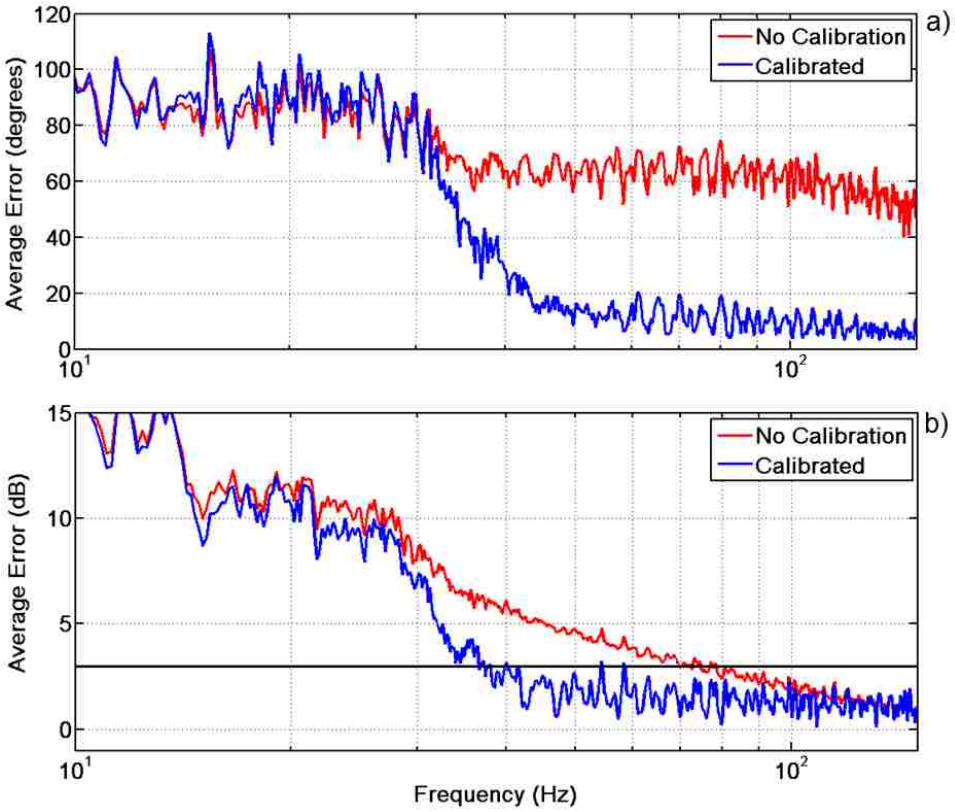

Figure 2.13. Average angle error (a) of the polar plots in Figure 2.12 and average intensity magnitude error (b) of the polar plots in Figure 2.15.

Nondimentionalized scaling of Figure 2.13 is given in Figure 2.15 which relates the angle and magnitude error to kd, wavenumber by microphone separation distance.

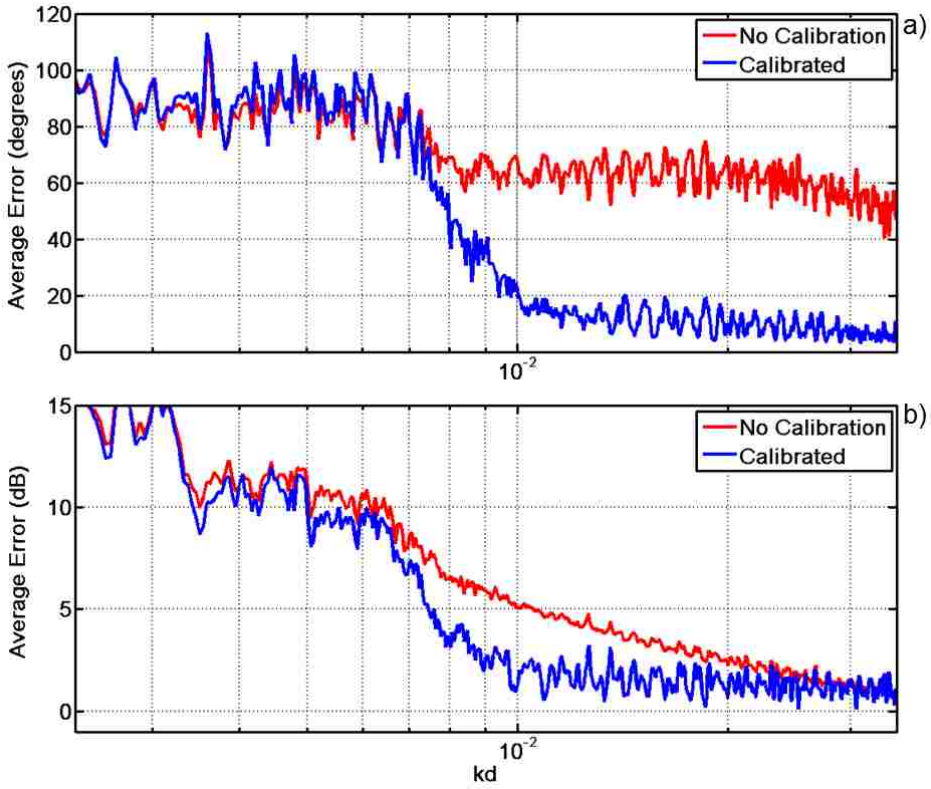

Figure 2.14. A kd scaled plot of Figure 2.13

Also a matter of interest is the accuracy of these sensors in measuring the magnitude of the acoustic intensity. Figure 2.13(b) shows average intensity error in decibels for the angles in the experiment and suggests that above 40 Hz we can expect less than 3 dB error for our calibrated transducer setup. If we consider 3 dB to be the cut-off value, we have extended the range of the probe from 80 Hz to 40 Hz. This factor of 2 increase in bandwidth on a kd scale can applied to future probe designs.

Although there appears to be a bias error for the calibrated intensity error, upon closer inspection we see that it is a gently sloping curve that continues to approach zero as frequency increases. It is likely that slight variations in calibrations are to blame, and seems plausible from the data of Figure 2.4. However, it is likely not possible to prove this concretely with the present

results. The reference source for this error analysis is the time averaged intensity of an acoustic plane wave: $< I_{plane} >= \frac{p_{rms}^2}{\rho_0 c}$ using the mean-square pressure of the four microphones. It is interesting to notice that as frequency increases, the impact of the calibration decreases. This is because increasing frequency means more acoustic phase separation between microphones and therefore the microphone phase error becomes less significant relative to the acoustic phase.

The magnitude error for measuring acoustic intensity is found in Figure 2.15. As was seen with the directional errors, there is a general improvement to the calculation by application of the calibration. At 120 Hz however, we see approximately equal error for the calibrated and un-calibrated cases but the angle of incidence is important when deciding if the calibrated or un-calibrated signal is better. This is likely due to one or more microphones having faulty phase calibrations at this frequency. Just as the calibration drifted slightly in Figure 2.8, there may be drift between laboratory calibration and outdoor experiments.

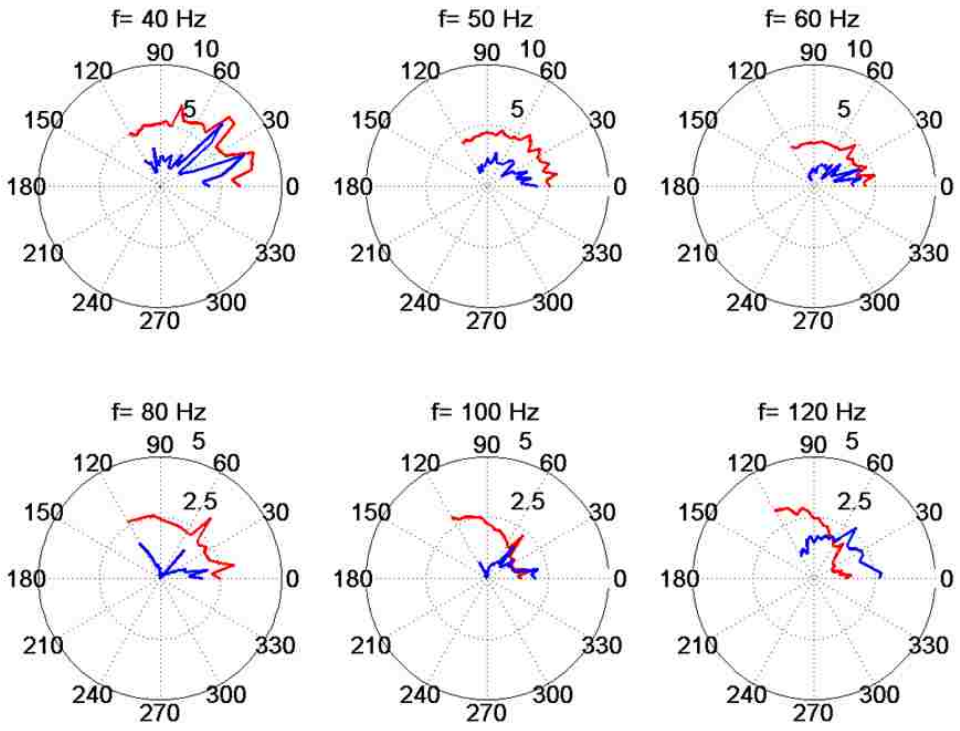

Figure 2.15. Magnitude error for measuring acoustic intensity for the calibrated result (blue line) and the un-calibrated result (red line).

2.5 Summary

Transfer function calibrations have been obtained for a microphone set and improve the low-frequency response of an intensity probe. The calibrated microphones can achieve variations in phase and magnitude matching of <0.02° and <0.06 dB on a given day. However the stability of these calibrations are questionable and therefore these tight tolerances are not recommended to use as guidelines when deciding microphone spacing to measure a specific frequency range until the day to day variation of a sensor set is known and accounted for.

For an outdoor measurement, and at various angles of incidence, the acoustic intensity was measured resulting in error plots showing the ability of the probe to determine the location and intensity of the source. The application of the transfer function calibration improved both

direction and magnitude measurements over the frequency range of 30 Hz to 100 Hz. Directional error of the intensity array was improved by ~40 degrees for 40 Hz to 100 Hz and intensity magnitude error also improved to be ~<3 dB for the same bandwidth. On a kd scale, this allows the usable range of the probe to be lowered to kd =8E-3 from 2E-2.

2.6 Suggestions for future work

Further experiments to confirm the usefulness of these calibrations may be more successfully achieved in a low-noise, half-space environment, such as a very large parking lot or a location such as the Bonneville Salt Flats of Utah. These locations will minimize error sources and give more insight into the next steps in developing these probes. For continued research it may be equally effective, yet simpler, to consider a two-microphone intensity probe at a single angle of incidence. Also, purchase or development of a low-frequency driver[22] capable of large amplitudes at infrasonic frequencies would be of interest for future work.

Further investigation into the stability of the relative calibration for a microphone set as affected by variations in temperature, pressure, time, rocket environment, etc. may enable one to account for it in the calibration process. For example, it has been seen in laboratory measurements (not reported here) that when a calibration is performed, there is a "warm-up" time for the sensor to achieve a steady state response. Research by another student at Brigham Young University, Ken Bostwick, has found that for any given day, there may be a 0.5° shift at a discrete frequency, say 100 Hz, in the calibration before a "steady state" response is achieved. This understanding applied in the lab calibration and the field measurement increases the effectiveness of the calibration.

Finally, it is presumed that if the same sensors as used to produce Figure 2.14 were used in another test with a separation distance twice as large, the kd plot would look the same, but the

frequency plot (as in Figure 2.13) would show a low-frequency bandwidth cutoff at half of that found previously. The accuracy/linearity of this kd-scaling should be checked and may uncover other factors that influence the calibrated intensity measurement at low frequencies.

2.7 Acknowledgments

This work has been supported by NASA as part of a phase II SBIR awarded to Blue Ridge Research and Consulting for development of an energy-based acoustic measurement system for rocket noise. (Proposal No. 09-2 O2.02 – 8697)

3 Experiment vs. theory – high frequency

3.1 Background

The paper presented as Chapter 2 of this thesis has discussed the low-frequency response of an acoustic intensity array. Herein we will explore some high-frequency limitations of similar arrays. It is imperative that the limitations of each array design are known that thereby we may have "constrained confidence" in the in-situ measurements that will be presented in Chapter 5 and Chapter 6. Please note that the experiments of Chapter 3 and Chapter 4 were performed independent of and before those in Chapter 2. Therefore, the findings of Chapter 2 are not applied to the analysis of these next two chapters.

Four pressure microphones arranged such that their diaphragm centers form the vertices of a tetrahedron can be used to determine acoustic vector quantities (i.e., intensity) in three dimensions. Wiederhold[8] has created a computer simulation analyzing the effectiveness of various arrangements of microphones to most accurately measure acoustic vector quantities. This chapter contains an experimental comparison to Wiederhold's work for three different, yet related, probe designs using the p-p finite-difference method. This method utilizes a pressure gradient calculated from two (or more) pressure microphones (p-p) to approximate the acoustic particle velocity. More information regarding the measurement of sound intensity using the p-p method may be found in Appendix A of this thesis.

The finite-difference method requires that a spatial pressure gradient be used to approximate the particle velocity of a sound wave. This approximation, along with scattering effects, and a pressure average estimated between sensors causes the p-p type acoustic intensity arrays to have magnitude and direction errors as well as a preferred orientation for minimizing measurement error for a given incident sound wave. There is much literature available discussing limitations

of the finite-difference and finite-sum approximations for high frequencies[16,23-25]. Wiederhold[8] gives a thorough analysis of these theoretical errors for four microphones arranged in a regular tetrahedron pattern both in free-space and mounted on the surface of a sphere. Physical approximations of these idealized sensors were built to compare in situ errors with those predicted by the model. These physical sensors are seen in Figure 3.1.

Each sensor has four microphones with their centers arranged in a tetrahedral configuration. The spherical array (SA) has a slightly irregular tetrahedral arrangement of microphones (tetrahedral angle of 120°) and has a diameter of 2.54cm. Another design uses an external frame (EF) to hold the microphone diaphragms at the vertices of a regular tetrahedron circumscribed by a sphere of diameter 3.81cm. The third design is also a regular tetrahedron and is similar in concept to the "Ono Sokki"[26] intensity array with microphone preamplifiers aligned parallel (PA) to each other and such that a 2.54cm diameter sphere would circumscribe the centers of each microphone diaphragm. The EF array has a larger diameter meant to compare with the SA array when a scaling factor of 3/2 is applied to account for scattering off the sphere.

Data for these tests were recorded by multiple National Instruments PXI-4462 cards at a sampling rate of 50 kHz. The transducers used in the arrays were GRAS 6.35mm 40BD with type 26CB constant current preamplifiers powered by the data acquisition system. Each array used microphones with sensitivities in the range of 4mV/Pa. Microphones for the SA array are permanently mounted into the sphere, the microphones used in the PA and EF arrays are removable and each array used the exact same microphones.

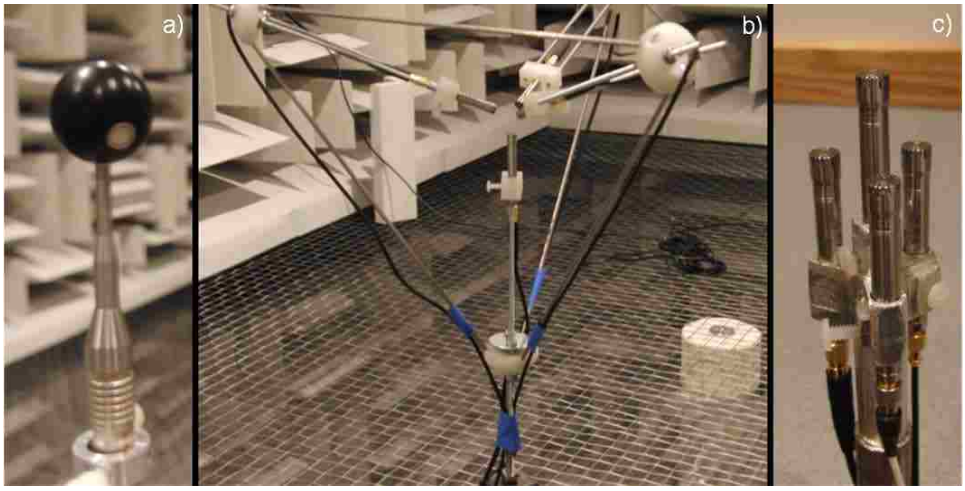

Figure 3.1. The three microphone designs used in this analysis are the spherical array (SA) (a), the external frame (EF) array (b), and the parallel axis (PA) array (c).

3.1.1 Sphere 3/2 factor

As discussed by Elko[27] and Parkins[28], scattering off a spherical array, such as that in Figure 3.1a, causes an error in estimating the acoustic intensity at low frequencies, i.e. where the product $ka << 1$ (much less than ~ 4 kHz for a 2.54 cm sphere). To compensate for this, it is common to use an effective sphere radius 3/2 times larger than the physical dimension during data processing. Intensity magnitude, as calculated using the p-p method, is inversely proportional to microphone separation distance (and sphere radius) and therefore, the magnitude of the acoustic intensity will increase with decreasing separation/radius and visa versa. It is important to notice that for a real measurement, the frequencies at which minimum and maximum error occur do not change with this scaling factor; it is simply a DC offset of $10\log_{10}\left(\frac{3}{2}\right) \approx 1.76$dB. Figure 3.2 illustrates the effect of changing the "effective radius" of the array.

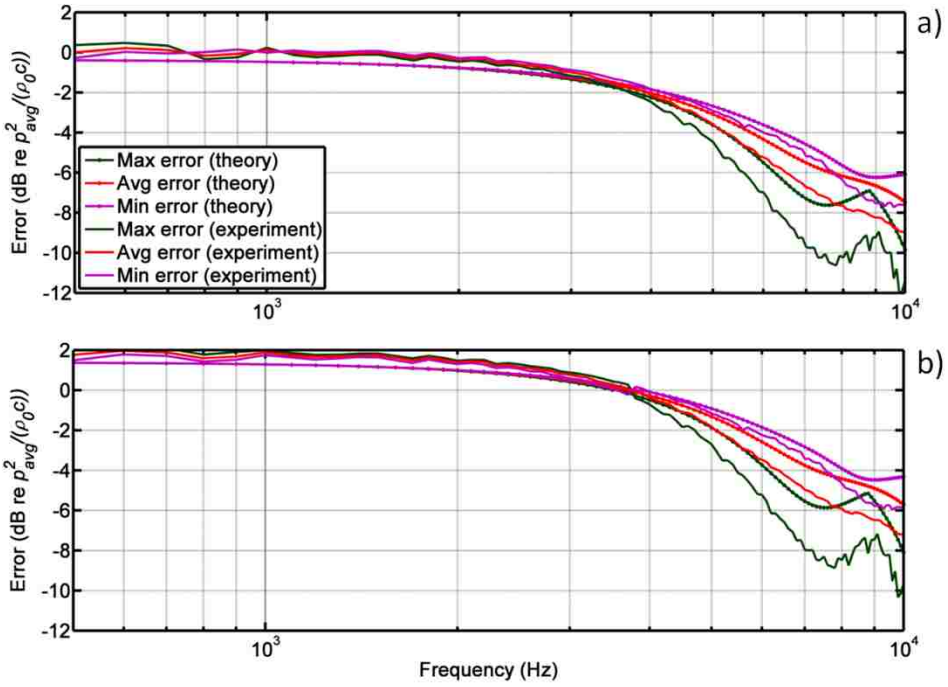

Figure 3.2. The expected and measured error in measuring active acoustic intensity over frequency for a spherical array of 2.54 cm physical radius that is processed using radii of a) 3*a*/2 or b) *a*.

One of the major advantages of using a spherical array is that with the 3/2 factor, it is able to accurately measure lower frequencies than a free-space array of the same size using the same microphones. When using this method, one must consider the frequencies of interest and determine if a sphere of radius *a* is more like a free-space array that can be circumscribed by a sphere of radius *a* or 3*a*/2. Wiederhold in his theoretical analysis has followed Elko and Parkins in using a free-space array of radius 3*a*/2 for comparison. The following analysis compares a spherical array and an approximation of a free-space array both having a radius of only *a*. To compare the experimental results that follow with the conclusions of Wiederhold, the reader may multiply the bandwidth of the PA array by a factor of 2/3 by assuming that bias errors related to linearly scalable effects are minimal (a fairly good assumption); this effectively makes the 2.54cm array a 3.81cm array.

3.2 Experiment

Wiederhold's theoretical results[8] were calculated by assuming a plane wave incident on a sphere at a particular angle. The angle was then changed a number of times to create an error map of the entire sphere surface. To mimic the theoretical test experimentally, a microphone array was mounted atop a turntable inside an anechoic chamber with a loudspeaker (22 cm diameter woofer) some distance (~4.5 m) away. By mounting the arrays on a turntable, we were able to rotate about one axis and look at errors along the array's equator, $\theta = \frac{\pi}{2}$. (Although not included in his thesis, Wiederhold's results for this particular case have been acquired as a comparison and they are included in this analysis.) As the wave propagates from the loudspeaker it is assumed to become planar relative to the size of the array. After each test the array was then rotated in increments of 2.5˚ until 360˚ was achieved.

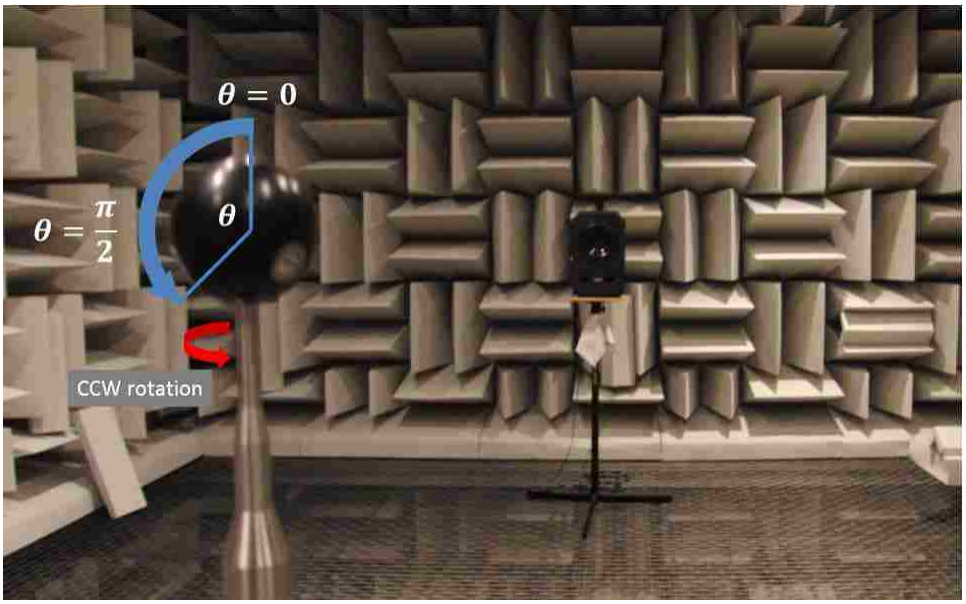

Figure 3.3. Typical experimental setup. Microphone is mounted atop a turntable and set some distance from a loudspeaker inside an anechoic chamber. The array is rotated so that $\theta = \frac{\pi}{2}$ forms a plane parallel to the floor as the array is rotated counter-clockwise (CCW) between measurements.

3.3 Analysis of the experiment

To approximate a plane wave field above 100 Hz, a loudspeaker source was set greater than 4 meters from the arrays in an anechoic chamber. This was done to produce experimentally Wiederhold's theoretical calculations mentioned in Section 3.1. Here we assess the plane wave approximation of the experiment.

The particle velocity for a spherical source, assuming time harmonicity, is given by

$$u = \frac{A}{r\boldsymbol{z}} e^{-jkr}, \tag{3.1}$$

where A is the amplitude, r is the distance from the source, k is the wavenumber and $\boldsymbol{z}$ is the specific acoustic impedance. For a plane wave, $\boldsymbol{z} = \rho_0 c$ and

$$\boldsymbol{z} = \frac{\rho_0 ckre^{j\theta}}{\sqrt{1 + (kr)^2}} \tag{3.2}$$

for a spherical wave. The angle θ may be defined as $\tan^{-1}\left(\frac{1}{kr}\right)$.

The particle velocity was calculated assuming both planar and spherical waves and the two results were compared. If kr is taken to be a non-dimensional scaling of wavenumber by distance between source and receiver, it is expected that the particle velocity magnitude of a spherical source is approximated by a plane wave assumption within 10% error at kr =2.18 and 1% error at kr =7.05. This means that these assumptions hold for kr values larger than those given. In the experiment, the source was set at least 4 m from the array, so at 100 Hz, kr =7.32. In other words, above 100 Hz, we should be able to assume <1% difference between plane and spherical wave fronts. As kr becomes large, for our experiment, we can say the wave field becomes "locally planar" and use plane wave analysis on our arrays.

Another characteristic of plane wave fields is that the pressure does not change over propagation distance. Spectra from each microphone on the SA array are shown in Figure 3.4 for a) a single orientation with 'Mic 4' facing the speaker, and b) the average level for the entire test. From this we see that at low frequencies the microphone levels are comparable. This alone is not indicative of a locally planar acoustic field; however, considering the previous analysis, it adds credibility to the assumption. Above 2 kHz, scattering begins to play a noticeable role in both the single rotation and the averaged measurements and our assumption of plane-waves becomes less valid. The following figures in this analysis have low-frequency cutoffs of 500 Hz, this was done to give uniformity to the presentation of results and to not distract from the high-frequency analysis being considered here.

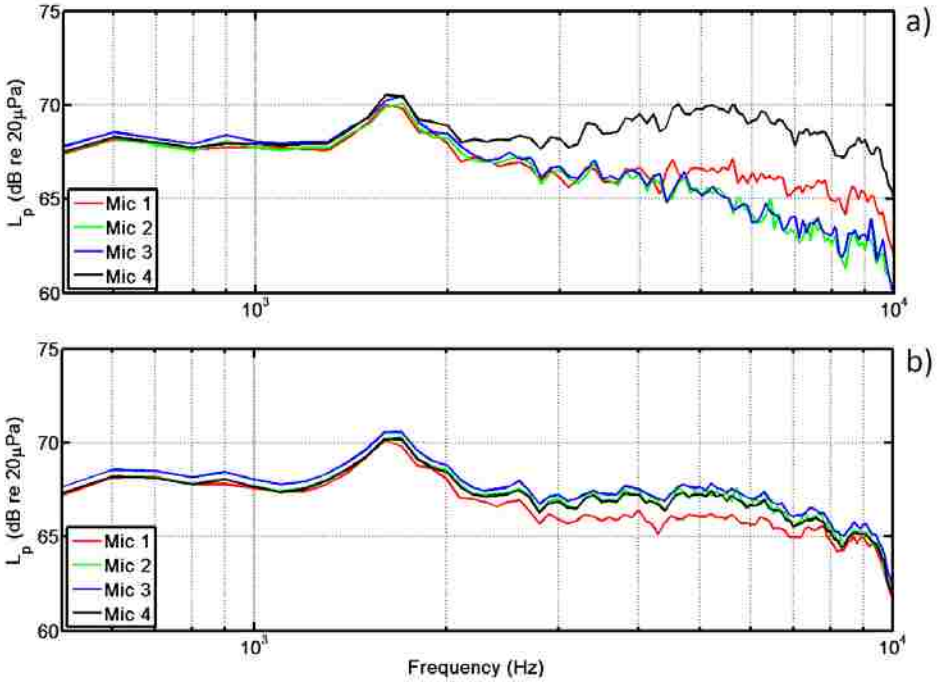

Figure 3.4. Sound pressure levels (L_p) for the SA array with a) the rotation such that microphone 4 is facing the source, and b) the average L_p for the test.

The other two arrays (SA and EF) in this analysis have a similar frequency range over which the agreement between the microphones support the argument of locally planar wave fields, i.e. <2kHz. Some spectra for the SA and EF arrays are seen in Figure 3.5 and Figure 3.6. The SA and EF arrays shown use the same microphones, however the EF array has a microphone separation distance 3/2 greater than the PA array. The variation in spectral response is a characteristic of the physical array into which the microphones are mounted.

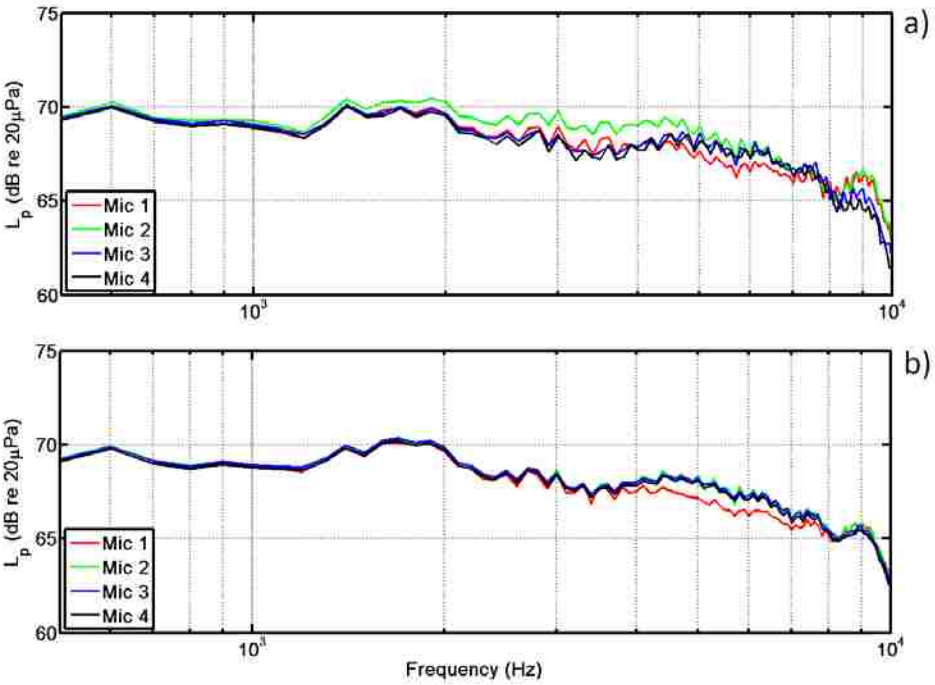

Figure 3.5. Sound pressure levels (L_p) for the PA array with a) the rotation such that microphone 2 is nearest the source, and b) the average L_p for the test.

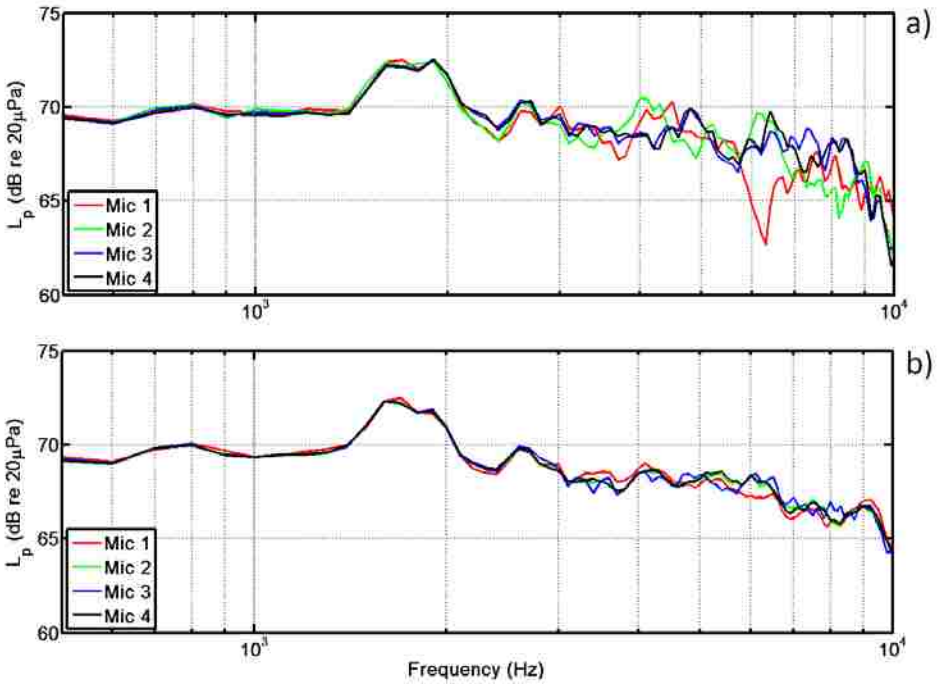

Figure 3.6. Sound pressure levels (L_p) for the EF array with a) the rotation such that microphone 2 is nearest the source, and b) the average L_p for the test.

Although technically situated in a spherical wave field, locally planar wave propagation is assumed valid in the frequency range of <2 kHz for these arrays. Using this assumption, we can compare the measurement of the array with the theoretical predictions developed by Wiederhold which assumes plane wave propagation.

As the microphone array is rotated over various angles of incidence, there are particular angles that give a better approximation. Figure 3.7 shows how the measured real part of the acoustic intensity, or 'active acoustic intensity', compared to the intensity of a plane or spherical wave. To calculate the acoustic intensity of a purely propagating wave, i.e. a plane or spherical wave, the average squared pressure of the four microphones in the array at each measurement angle, p_{avg}^2, is used in the relationship

$$I = \frac{p_{\text{avg}}^2}{\rho_0 c}, \tag{3.3}$$

where ρ_0 is the density of the medium, and c is the sound speed. As seen in Figure 3.4, the pressure of each microphone may be slightly (or largely) different from one another for a given angle of incidence or frequency; this will introduce error into estimating the correct intensity. Although other weightings of the microphone pressures, such as the use of the center microphone alone, may produce a more accurate result of the acoustic intensity, the average squared pressure is used to directly compare with the results supplied to the author by Wiederhold[8] during some of Wiederhold's preliminary work.

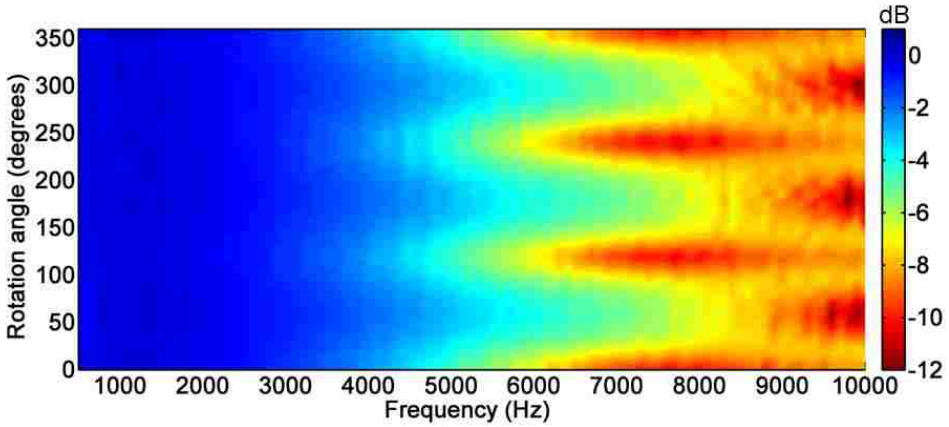

Figure 3.7. Intensity magnitude error relative to plane wave intensity calculated via Equation 3.1, utilizing the average squared pressure of the four microphones in the array for p_{avg}^2.

From the data presented in Figure 3.7 one is able to calculate the minimum, maximum and average errors over all rotation angles. We see that for this array, that at angles of 60°, 180° and 300° we have regions of minimum error between approximately 4 kHz and 8 kHz. These angles correspond to rotations such that the sound is incident on a microphone diaphragm facing the source. The regions of larger error (between these angles) correspond to the rotations where a

microphone is directly opposite the side of the sphere where the sound is impinging. At 8 kHz to 10 kHz, these regions appear to switch which has the most severe error.

An alternative method to analyze the error is by plotting the minimum, maximum and average errors averaged over each rotational angle as is done in the following figures over the frequency range 500 Hz to 10 kHz.

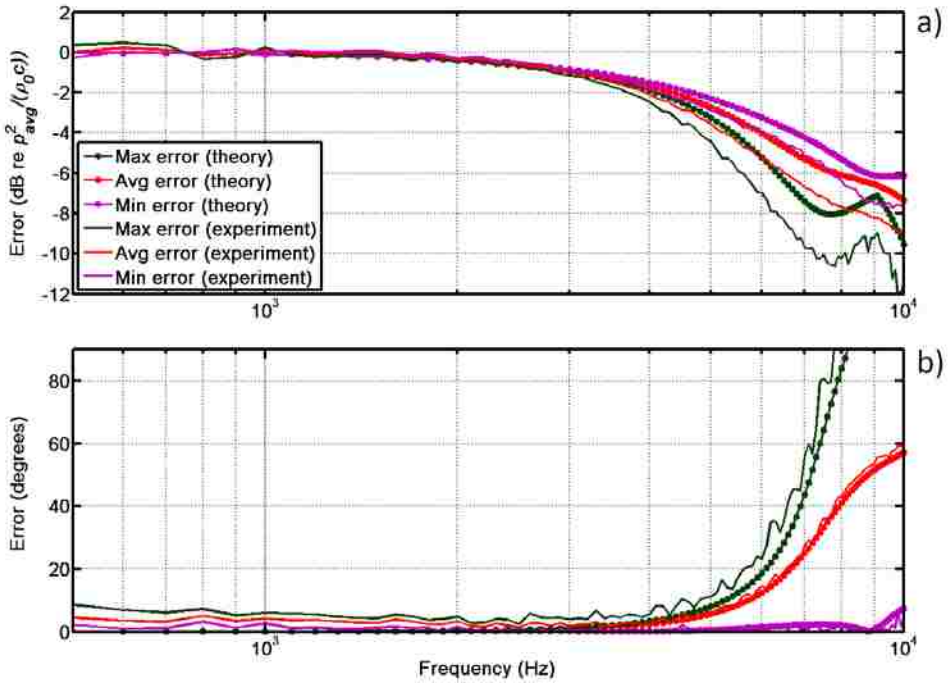

Figure 3.8. Theoretical and experimental error in estimating the magnitude (a) and direction (b) of the active acoustic intensity using the SA array.

Magnitude and angle error over a full 360° rotation of the SA array are given in Figure 3.8. There are obvious discrepancies between theory and experiment, however the general trends and the overall agreement is good, differing by <3 dB error from 500 Hz to 8 kHz in the case of the maximum error. Having utilized the 3/2 factor during processing and based on the analysis of Chapter 4, the most accurate and usable range of the sensor is for frequencies less than 4 kHz. If

we focused in this range only, there is <1dB deviation from the average error and only ~2dB error overall. Directional errors also show good agreement between experiment and theory for general trends and tend to deviate more as frequency increases. It is expected that there would be more experimental error arising from scattering and misalignment of the array during testing and this is seen in both the magnitude and direction for the active acoustic intensity in Figure 3.8. At frequencies above 7 kHz the scattering of the array becomes apparent in both the theoretical and experimental results. It is supposed that small misalignment and relative phase differences between microphones is responsible for the non-zero angle error at low frequencies in Figure 3.8.

The EF array design was tested in similar manner to the SA array and the summary plots of Figure 3.9 show the maximum, minimum and average values over the full rotation of the test. This array configuration is compared to Wiederhold's results for microphones in free space and does not account for any assumed scattering effects as did his spherical results, although in practice, there is scattering.

It is interesting that the intensity is overestimated at 500 Hz. This discrepancy suggests that either our microphone separation distance was recorded incorrectly, the atmospheric conditions, ρ_0 and/or c are slightly off or simply our microphones do not average to the pressure at the center of the microphone diaphragm. The overall trending of active acoustic intensity magnitude has <3 dB 'average error' agreement between 500 Hz and 10 kHz although theory and experiment do not trend as closely as for the SA array. The error in acquiring the direction from which the sound came is more unpredictable above 3 kHz but is less than 10° for 500 Hz to 3 kHz.

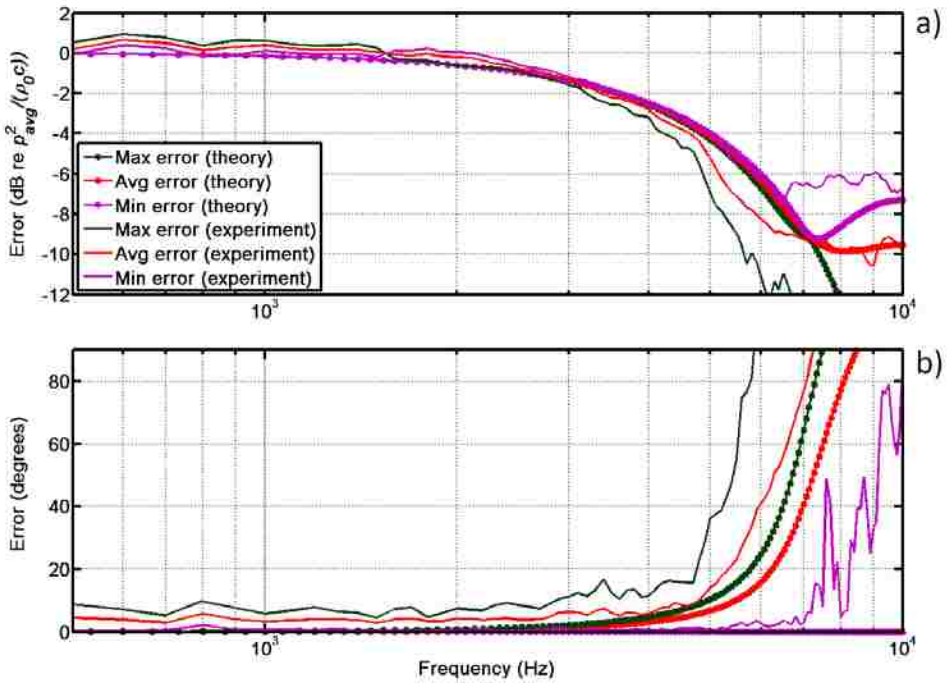

Figure 3.9. Theoretical and experimental error in estimating the magnitude (a) and direction (b) of the active acoustic intensity using the EF array.

For the remainder of this analysis, we will consider only the SA and PA arrays. The EF array is essentially the same "free space" design as the PA array but it is much more limited in bandwidth for the measurements obtained.

The angle and magnitude error plots for the PA array design follow in Figure 3.10 and are compared against the same theoretical results the EF array was compared to. For this array design, we see that the experiment and model have fairly good agreement with <2 dB difference over the entire range shown. Below 4 kHz, the two arrays perform similarly with the PA array overestimating the pressure slightly. The PA design also performed well in the direction measurement of the source, having lower maximum, minimum and average errors than the sphere above 4 kHz. Figure 3.10 also demonstrates what is assumed to be misalignment or microphone phase response error evidenced by the significant amount of low-frequency error. It

appears that for the microphones used in this experiment, we must be willing to accept up to 10° error (worst case) for estimating the direction of the acoustic intensity for an arbitrary angle of incidence.

The PA array has been compared against a theoretical model that did not include any scattering effects. Observing the tight agreement between theory and experiment in Figure 3.10 a, we may surmise that the expected bias due to finite approximation errors is more detrimental than scattering errors to the correct estimation of the active acoustic intensity.

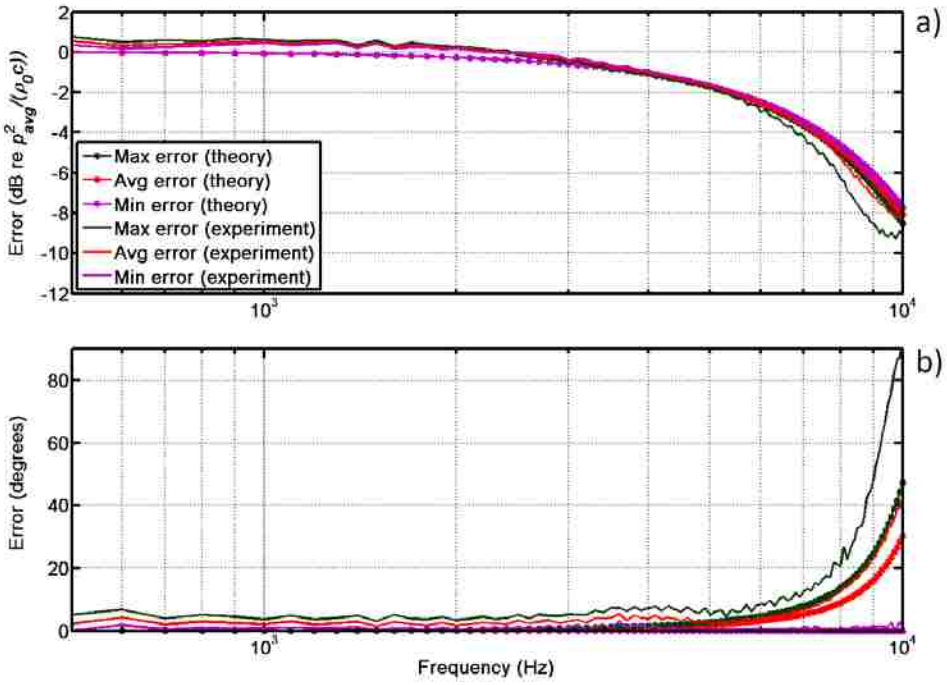

Figure 3.10. Theoretical and experimental error in estimating the magnitude (a) and direction (b) of the active acoustic intensity using the PA array.

Directivity plots of the magnitude and angle errors can better illustrate the directivity of these sensors at discrete frequencies. In Figure 3.11, the directivities are shown for arbitrary frequencies chosen between 500 Hz and 4 kHz. The orientation of the microphone array is such that when the rotation angle is 0° (numbers on the outer rim of the directivity plots) the x-axis of

the microphone array points in the direction of 0° (see Figure A.2 in Appendix A). Results are presented first for the SA array measuring active acoustic intensity. The concentric circles of Figure 3.11 represent dB error with the outermost ring being 5 dB. Around the plots is shown the angle of incidence of the sound wave relative to the x-axis. The error shown is the absolute value of that of Figure 3.8(a).

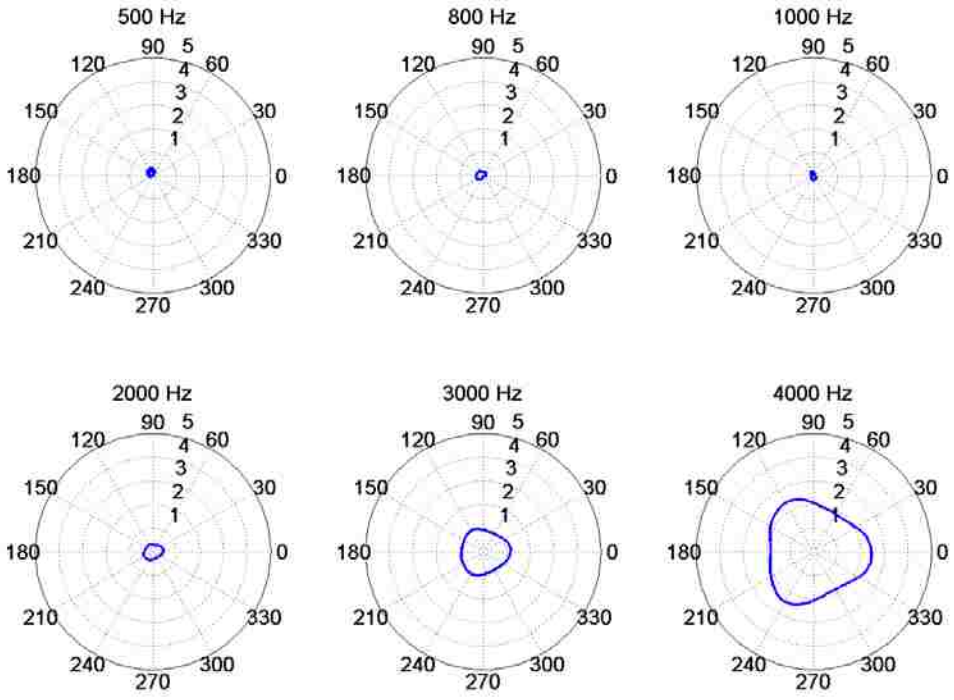

Figure 3.11. Directivity plots for the absolute value of the intensity magnitude error for the SA array.

Figure 3.12 is similar in layout to Figure 3.11 but shows the angle error of measuring where the sound came from. As frequency increases, there is general trend towards increasing error (as previously seen). We also notice that for the 3 kHz and 4 kHz cases there is directivity that corresponds to more error when a microphone is on the reverse side of the sphere compared to the incident plane wave.

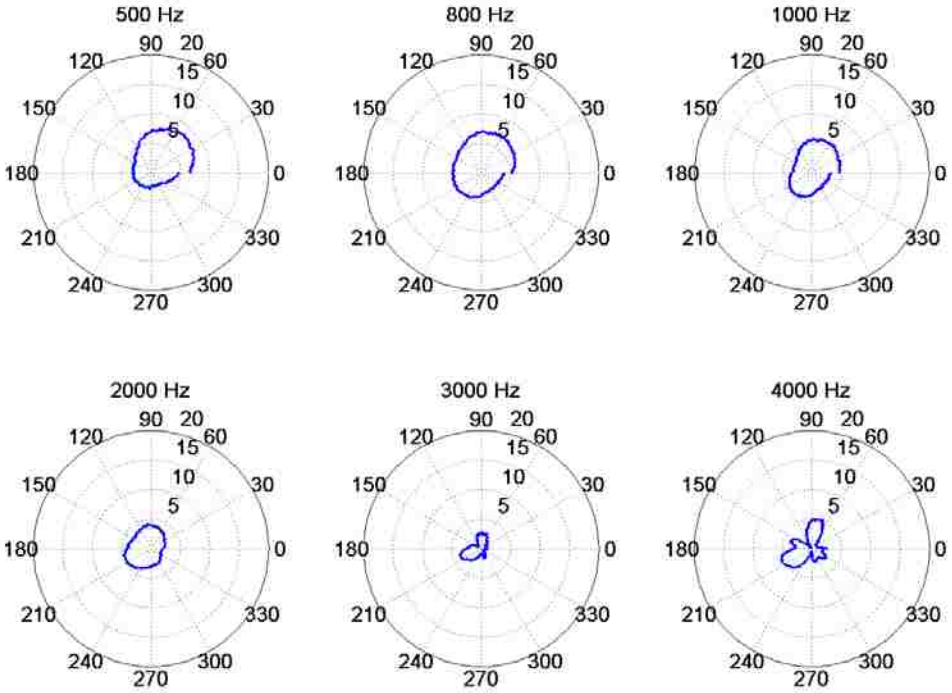

Figure 3.12. Directivity plots for the angle error for the SA array.

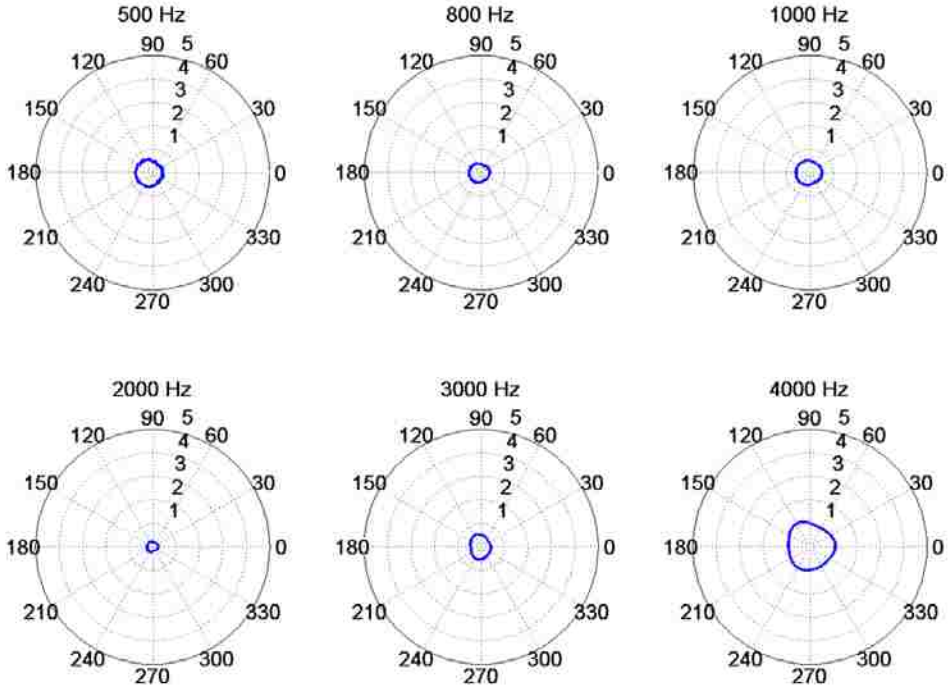

Figure 3.13. Directivity plots for the absolute value of the intensity magnitude error for the PA array.

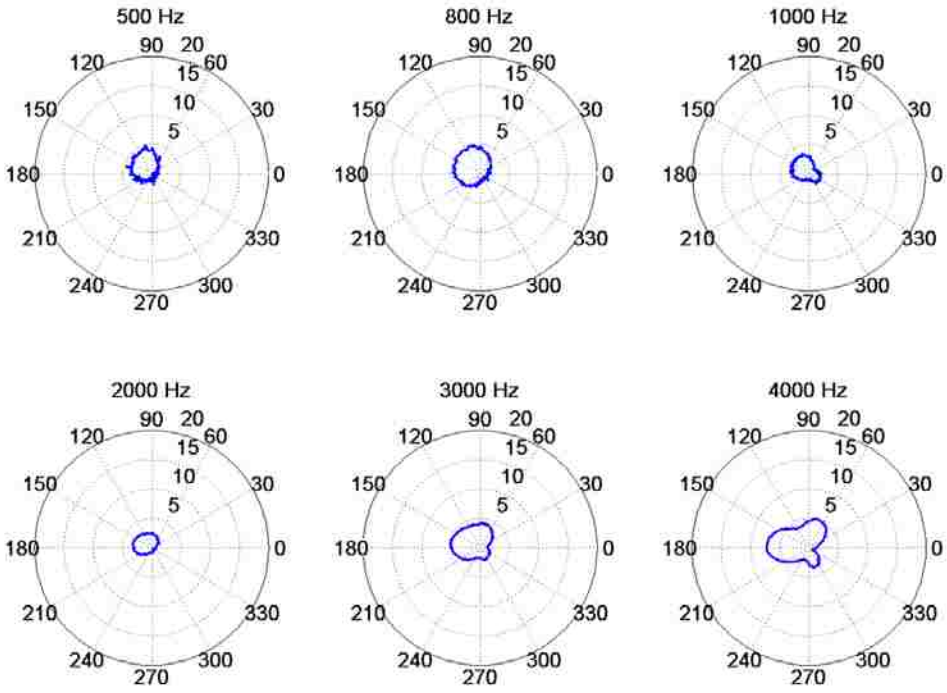

Figure 3.14. Directivity plots of the angle error for the PA array.

The SA array shows small, yet steadily increasing error in Figure 3.11 while the PA array has more error in Figure 3.13 but it appears to grow less quickly; this observation is consistent with Figure 3.8(a) and Figure 3.10(a). Angle error is interesting in that it is not as symmetric as one would suppose for either microphone array design. In Figure 3.12, the results seem to lean towards 60° and towards 150° in Figure 3.14. It is possible that some precession during rotation or other variation in the experimental setup may account for this non-symmetric error at lower (<2 kHz) frequencies. Non-symmetries at very low frequencies (<500 Hz) are most likely related to relative magnitude and phase discrepancies between sensors as was mentioned in Chapter 2, however they were not made a part of this analysis.

3.4 Calibration of magnitude errors

The principal application of these sensors has been in measuring acoustic intensity, a vector quantity having both magnitude and direction. Theory and experiment have shown that for an

approximated plane wave field there are preferred angles of incidence or orientations of the array resulting in the most accurate measurements. Further preferential orientations may be influenced by small fluctuations in magnitude or phase response between two nominally "flat" microphones. It is common in the use of transducers such as a microphone to perform a calibration at a single frequency i.e. 250 Hz or 1 kHz using a reference tone at a known level. In this way, the nominally "flat" spectral response of the microphone may be shifted in amplitude to match the calibrated reference tone. If the spectral response of the microphone, or intensity array in this case, is not spectrally "flat", a broadband calibration may be applied.

In Figure 3.8 (a) and Figure 3.10 (a) we see that the average theoretical error at 8 kHz is approximately 8 dB for the SA and PA arrays. In both cases, the measured error is within approximately 2 dB of the expected error. If the active acoustic intensity magnitude is all that is desired of a measurement, one may use the average theoretical error as a broadband calibration. This would improve the intensity magnitude estimate by up to ~8dB at some frequencies, with respective tolerances of less than -3 and -2 dB for the SA and PA arrays up to 10 kHz. This calibration would not be dependent upon microphone selection.

3.5 Calibration of angle errors

The calibration of angle errors is significantly more complicated. Finite differencing and scattering errors both predictably affect the ability of the array to accurately predict the direction from which the sound came. However, for a post calibration to work properly, each measured angle must correspond directly to a single "correct angle", or in other words, no two measured angles can be from the same "correct angle" unless the two measured angles are identical. In the theoretical model, there appears to be some ability to construct "error gradients" that describe the smoothly varying error over frequency and rotation. If the same smooth variation of error

was obtained for a given experiment, the theoretical error gradients could be useful in improving the angle calculation but, in practice the author has not seen this type of predictable response for the experimental plane wave environment.

3.6 Alternate orientation

In the aforementioned experiment, we considered measurements as the arrays were rotated about $\theta = 0$ (Figure 3.3). It is expected that different rotations may emphasize limitations of the array designs. For this reason, the same microphone arrays were rotated by 90° such that the top microphone in the previous experiment was now pointing towards the source for the initial measurement position. Again the arrays were rotated counterclockwise in 2.5° increments until a full 360° rotation was achieved. This particular orientation was chosen because it explored a presumed limitation of the PA array that scattering would be large when all microphones pointed either directly towards or away from the source. The previous orientation only explored grazing incidence acoustic waves for that design. For this orientation of the arrays, the theoretical prediction is not avalible.

Surprisingly, the alternate orientation did not have as great of an impact as was conjectured. Indeed, by comparing Figure 3.15 and Figure 3.16 with Figure 3.8 and Figure 3.10 we see that this second orientation has more error, but not substantially so; particularly below 4 kHz where the arrays perform best. If we constrain our analysis to the region 500 Hz to 4 kHz, the average error of the measurements are accurate within ~3 dB and 10° for magnitude and direction errors. For this orientation of the array, there are significantly more scattering surfaces (cables, microphone holders, etc) in the plane of the measurement. This may be a primary reason for increased error above 4 kHz.

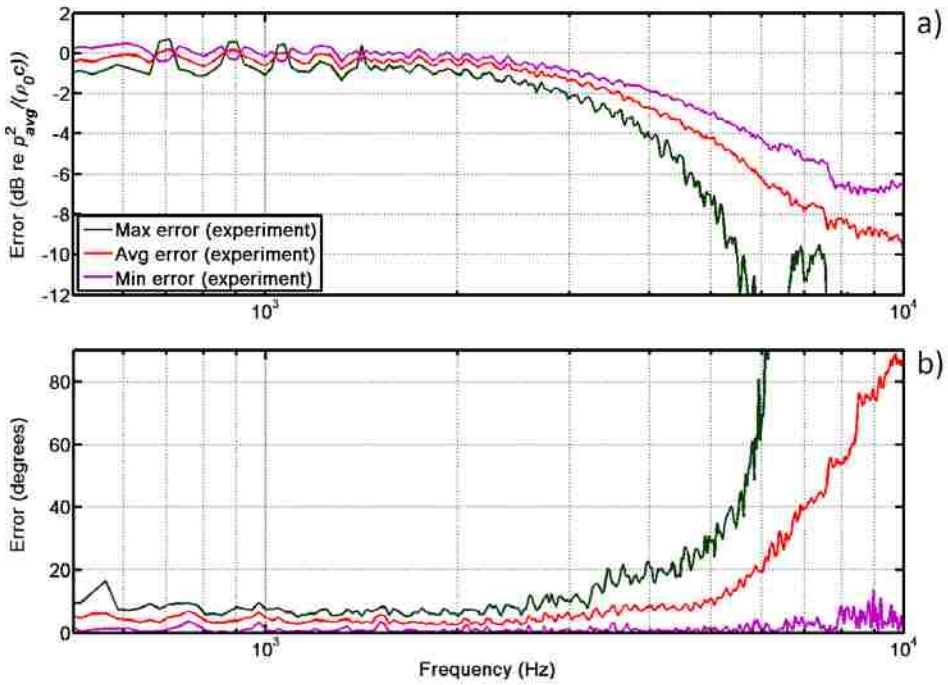

Figure 3.15. Experimental error in estimating the magnitude (a) and direction (b) of the active acoustic intensity using the SA array rotated about $\theta = \frac{\pi}{2}$.

Figure 3.16(a) shows that the experimental magnitude error, for the PA design. Between 500 Hz and 3 kHz, this configuration of the PA array seems to excel in both magnitude and directional response having ~1 dB and 10° error over this range.

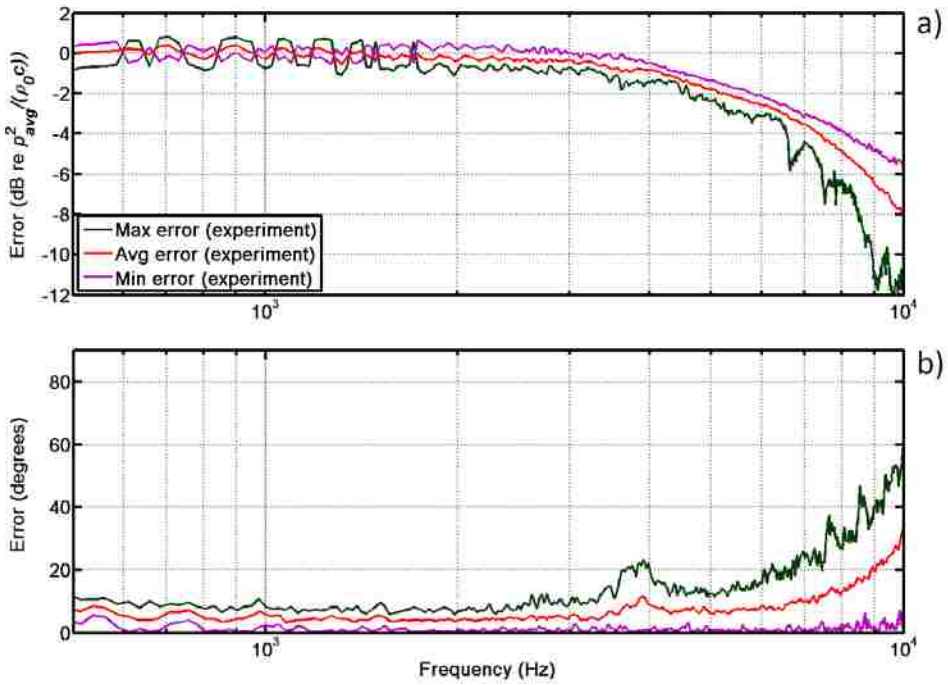

Figure 3.16. Experimental error in estimating the magnitude (a) and direction (b) of the active acoustic intensity using the PA array rotated about $\theta = \frac{\pi}{2}$.

Directivity plots, as in Figure 3.17, show the dB error between measured intensity and the plane wave intensity calculated from the mean square pressure of the microphones for the array. The concentric circles represent decibel error with the outermost ring being 5 dB. Around the plots is shown the angle of incidence of the sound wave. At 0°, the top-most microphone diaphragm points towards the source. When the z-axis of the arrays points towards the loudspeaker source, the angle of rotation is defined as 0°. Figure 3.17 at 4 kHz shows the most error as the top microphone points towards the source. The PA design, shown in Figure 3.18, was surprising at this same frequency of 4 kHz because the greatest error occurred for the rotation of 90° which is the same "grazing incidence" orientation that was previously discussed. Although the PA design appears to obtain better magnitude measurements, it should be noted again that there may be some discrepancy with comparing the SA array with a free space array by the use

of the 3/2 factor in processing the SA array data. The weighting results in a 1.76 dB bias error; a significant difference that is on the same order as the errors we are investigating.

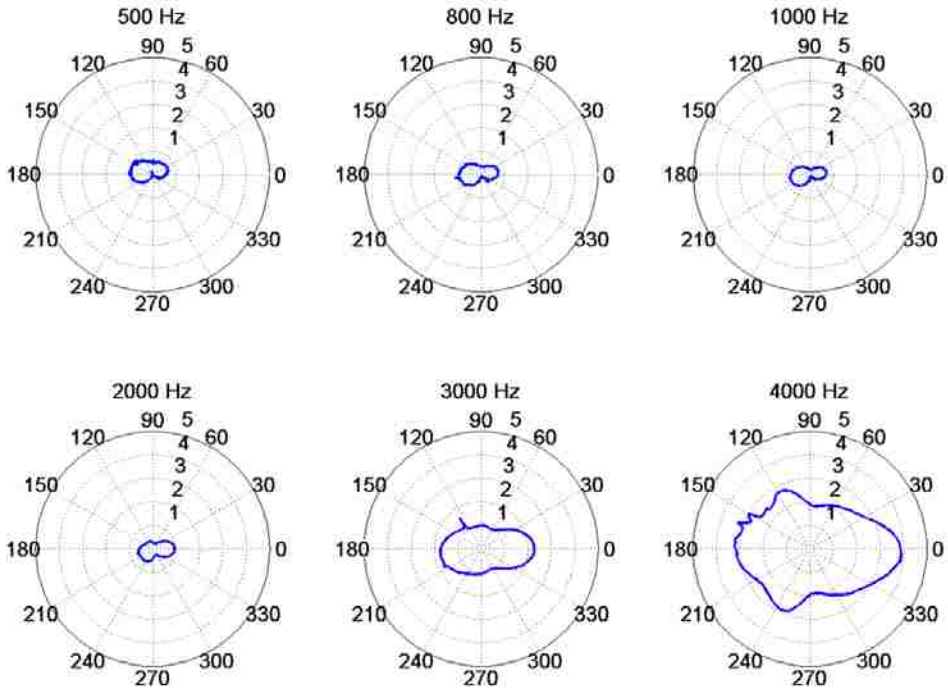

Figure 3.17. Active acoustic intensity error plots for the SA array.

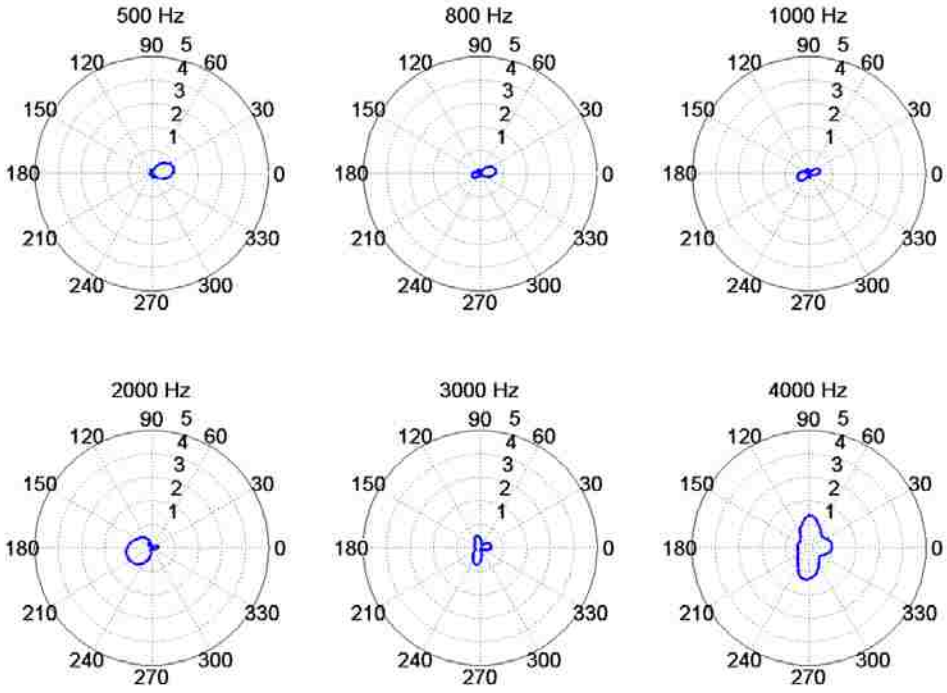

Figure 3.18. Active acoustic intensity error plots for the PA array.

Intensity magnitude error is surprisingly small for this rotation as well. It was expected that the cables and support structure would introduce excess errors, particularly in the case of 180° rotation. Also unexpected is that the more-symmetric SA array has overall more error for these frequencies than the PA design. Figure 3.19 and Figure 3.20 show that directional errors at lower frequencies appear to be less directional than those at 4 kHz for each array design. In each case, the direction is estimated the worst when the array points away from the source.

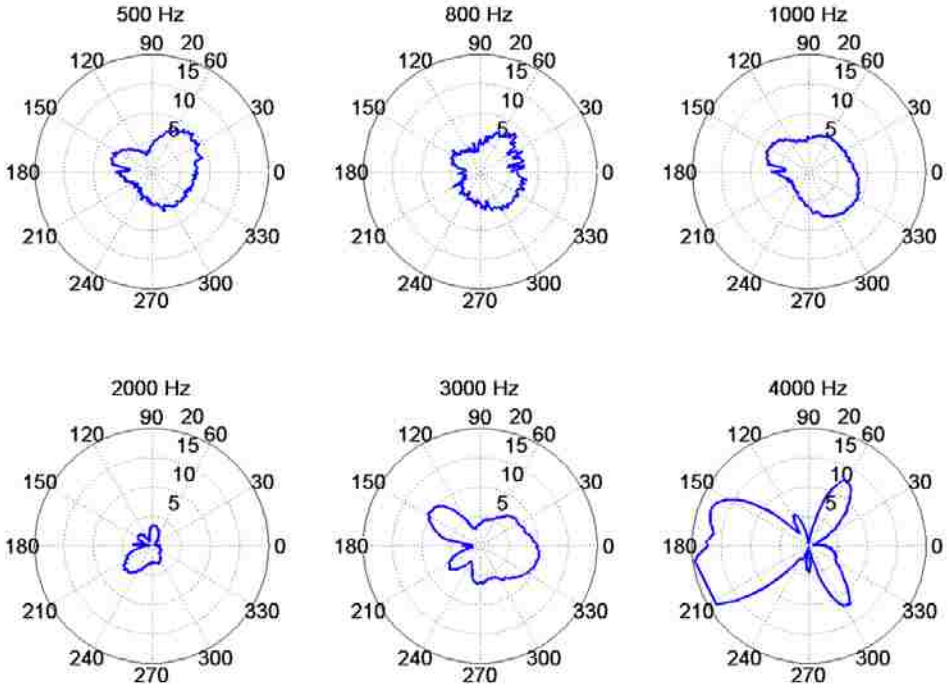

Figure 3.19. Error in estimating the direction of the active acoustic intensity vector for the SA array.

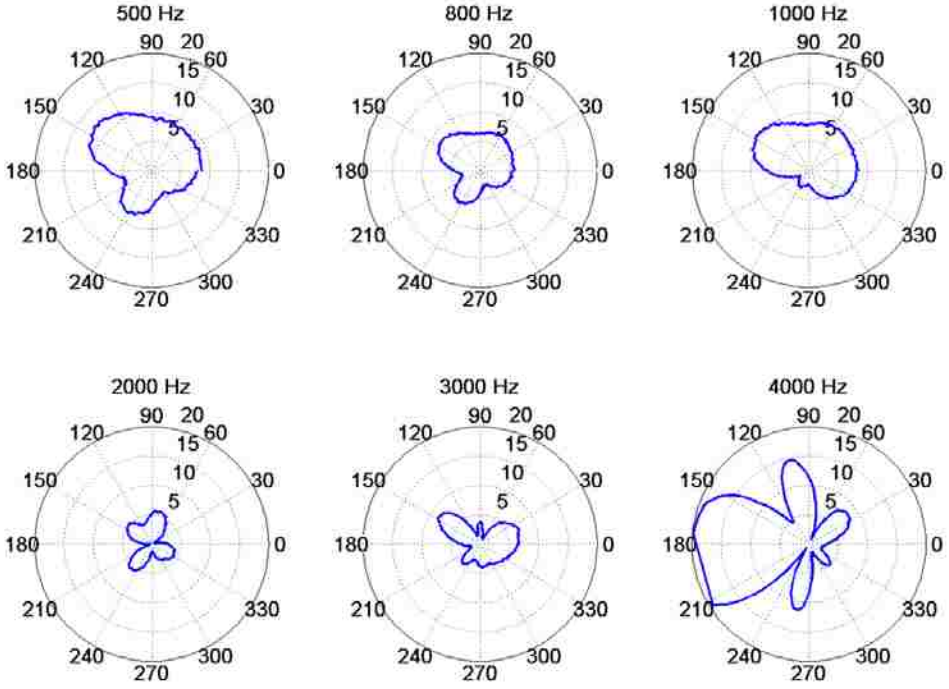

Figure 3.20. Error in estimating the direction of the active acoustic intensity vector for the PA array.

It is expected that, neglecting calibration errors, the lowest frequencies should give the best estimation of direction. Of the frequencies shown, both of these sensors measure direction the best at 2 kHz. This result is surprising and may be related to errors inherent in experimental testing including, but not limited to, phase relationships of the microphones. At high frequencies, i.e. 4 kHz, both the SA and PA array are highly directional in the angle estimate. This same directionality was not seen for the measurement of intensity magnitude which may suggest that measurement of the intensity magnitude is more robust to scattering and diffraction of the sound wave for these two designs.

3.7 Conclusions

For these controlled measurements performed in an anechoic chamber, it has been shown that the magnitude of the active acoustic intensity may be theoretically determined within 2-3 dB accuracy between 500 Hz and 10 kHz for the rotation about $\theta = 0°$. The error in estimating the direction of the active intensity vector has been shown to be theoretically calculable to varying precision (based on frequency). A second orientation of the arrays was chosen in an attempt to highlight/explore the omnidirectionality of the sensors and illustrated how orientation and frequency of interest impact the performance of the array.

It has been seen that for the two designs primarily presented here, the 2.54 cm PA array consistently out-performs the 2.54 cm SA array in these particular measurements of the active acoustic intensity vector magnitude and direction with the exception of the low-frequency (approaching 500 Hz) end of the acoustic intensity vector where the PA design actually over-estimates the intensity by approximately 0.5 dB.

From the results of this analysis, it is recommended that for two equal size SA and PA type arrays of 2.54 cm diameter, the PA array should be pursued for future development if

frequencies greater than 4 kHz are of interest. Although a magnitude calibration for the SA array may be possible based upon the theoretical analysis, an angle calibration appears to be considerably more difficult, particularly due to the larger spread of minimum, maximum and average errors above 4 kHz. The limited scattering at high frequencies of the PA array is what gives it naturally lower measurement error for a similarly sized SA array. At low frequencies, the SA array performs either better, or worse than the PA array depending upon if we choose to apply a 3/2 scaling factor to account for diffraction effects. By applying the 3/2 factor to the SA array, the low-frequency response of the array is improved by up to ~1.76 dB, however, the high-frequency response drops in accuracy by the same margin.

4 Energy analysis

Heretofore we have considered the measurement of active acoustic intensity using tetrahedral microphone arrays. These same arrays may also be used to calculate other acoustic quantities including reactive intensity, kinetic energy density, potential energy density, and total energy density. Appendix A contains information regarding how to process the microphone data to obtain these quantities. In this chapter we will use the experimental data of Chapter 3 to compare some of these quantities and discuss their limitations. This is useful in helping us to determine the frequency range over which we may trust measurements in situ.

This Chapter includes more data from the SA, PA and EF, microphone arrays described in Chapter 3. The results presented here correspond to the rotation about $\theta = 0°$ for each design (see Figure 3.3). As is the case with each of the figures in this section, frequency has been given a non-dimensional scaling of ka which refers to wavenumber, k, by the radius, a, of the sphere that just circumscribes the center of each microphone in the array. This scaling allows us to consider what the response of the array should be for any size array for which all the assumptions scale linearly.

There is a 2/3 factor difference in the frequency range covered by EF array compared with the SA or PA array for each of the ka plots in this chapter. This difference is due to the fact that the physical spacing of the sensors in the EF array is 2/3 times larger the PA array. The curves for the SA or PA array may be compared directly to those in Chapter 3 spanning the frequency range 500 Hz to 8 kHz; the EF array covers two-thirds of that range, or 333 Hz to 5.3 kHz.

4.1 Active intensity

The ability of the arrays to measure the active acoustic intensity has been discussed in Chapter 3 of this thesis. To draw a connection between the work of Chapter 3 and the analysis of this chapter, the active intensity results are included briefly. The arrays were rotated in the sound field, and the average error in calculating the active acoustic intensity magnitude is determined as a function of frequency as in Figure 3.8, and Figure 3.9, and Figure 3.10 for a full rotation of the array.

It is difficult to set parameters for where a method is considered valid, and as such, these are arbitrary and they should be tailored to fit the needs of each reader. For example, if we assume a cutoff of -3 dB in Figure 4.1 a), we see that the SA array has a cutoff around ka=1.1 and the two free space arrays have a cutoff at about ka=1.5. When choosing the diameter, a, of a measurement array, these values may be used to predict at what frequency we may expect 3 dB of error. In Chapter 3, it was found that the arrays measure acoustic intensity best below 4 kHz. This frequency corresponds to a ka value of ~0.93 for the PA array. Figure 4.1 b) shows the average error in estimating the active acoustic intensity between 500 Hz and 4 kHz.

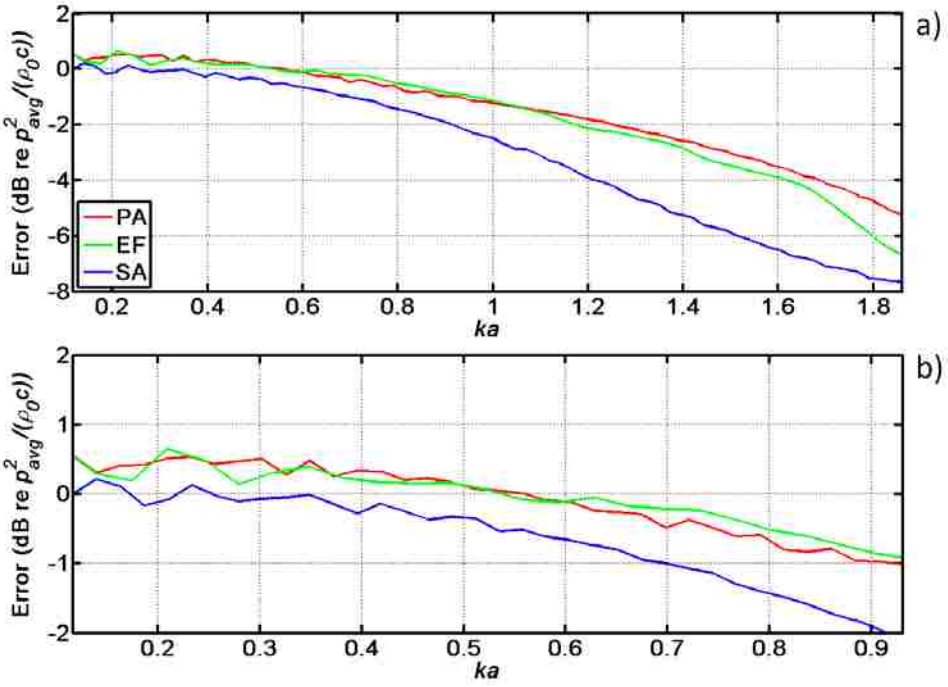

Figure 4.1. Average error in estimating the active intensity magnitude for the PA, EF and SA arrays over a full rotation of the array as calculated in Chapter 3 for a) 500 Hz to 8 kHz and b) 500 Hz to 4 kHz for a=1.27 cm.

The average directional error for all measurement angles of the active acoustic intensity is similarly presented in Figure 4.2. In Chapter 3, the active acoustic intensity was compared theoretical vs. experimental and the SA array matched very closely these two data sets. It is now seen more clearly that on average, it has more error at high frequencies. In Figure 4.2b) we notice that each of the arrays have roughly the same amount of error for ka <0.93. This is an expected result that has already been shown in Chapter 3. In both the active intensity magnitude and direction, the EF and PA arrays nearly match results on the ka scale. This result gives credibility to the idea of using ka plots to design arrays for a specific bandwidth.

It is interesting that each of the array designs have an approximate error of approximately 3° at low frequencies as shown in Figure 4.2. It may be that this error is related to experimental

uncertainty. For this experimental setup where there are 4 meters between loudspeaker source and receiving array, a 3° error corresponds to 21 cm error in locating the source.

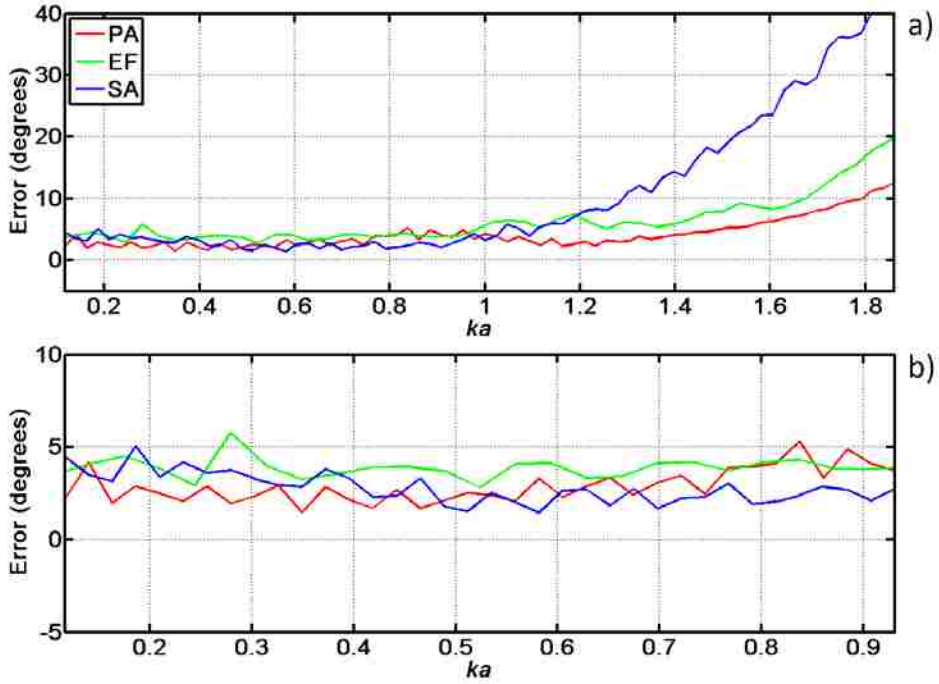

Figure 4.2. Error in estimating the location of the source for the PA, EF and SA arrays as calculated in Chapter 3 for a) 500 Hz to 8 kHz and b) 500 Hz to 4 kHz for a=1.27 cm.

4.2 Reactive intensity

The complex acoustic intensity is made up of both the real 'active" part and the imaginary 'reactive' part. The active acoustic intensity measures the flow of energy through a region of space whereas the reactive intensity is concerned with the energy that does not propagate but oscillates near the source[29]. Hence, although the reactive intensity magnitude may be non-zero, the time average of the reactive intensity is zero by definition. It also follows, that as a non-propagating quantity, the magnitude of the reactive intensity goes to zero in the far field. The experiments of Chapter 3 were such that the arrays were placed a number of wavelengths from

the source (assuming f > 500 Hz) therefore, we would expect the reactive intensity to be negligible relative to the active intensity.

For an acoustic monopole, the acoustic pressure at a non-dimensional scaled distance kr may be written as

$$p(kr) = \frac{j\rho_o c k^2 Q}{4\pi kr} e^{j(\omega t - kr)}, \tag{4.1}$$

with Q as an arbitrary source strength. From this, the particle velocity may found via Euler's equation to be

$$u(kr) = \frac{k^2 Q(jkr + 1)}{4\pi(kr)^2} e^{j(\omega t - kr)}. \tag{4.2}$$

The reactive intensity is then calculated as $Q(kr) = Im(pu^*)$, and the active intensity then may be found as the real part of the same argument. The difference between these quantities is plotted in Figure 4.3 as a function of kr. For small kr values, i.e. low frequencies, or near the source, the reactive intensity is expected to be larger than reactive intensity. However, the reactive intensity rolls off in amplitude more quickly and becomes comparably negligible in amplitude as kr increases.

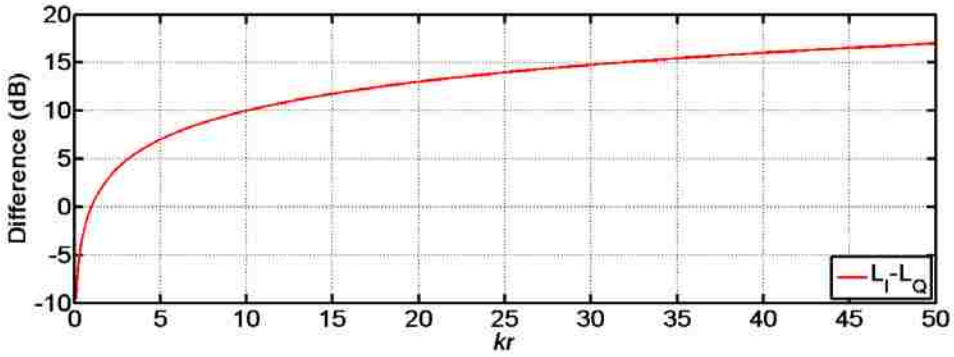

Figure 4.3. Expected difference between active and reactive intensity levels for a spherically diverging wave from a monopole source as a function of kr.

Using the information of Figure 4.3, and assuming standard atmospheric conditions at a frequency of 500 Hz and 4 meters from the source, we expect the active intensity to be ~15 dB higher in level than the reactive intensity. This chosen example corresponds to what we expect the difference between active and reactive intensity levels to be for our experimental setup. The plots in Figure 4.4 show the relationship of active and reactive acoustic intensity levels for the experiment described in Chapter 3. Notice that the independent variable of Figure 4.5 is ka, not kr, and r is a fixed distance of $r \approx 4$ meters determined by the experimental setup.

For lower ka values, i.e. < 0.5, we see that there is between 8 and 14 dB difference in level between the active and reactive intensities. Although it does not match the expectation of 15 dB, it does tell us that the reactive intensity is relatively small. As ka increases, there is relative increase in reactive intensity, however this increase is likely related to array processing and not the physical characteristics of the sound field; we know from Chapter 3, that the active intensity is underestimated as frequency increases. For values of $ka < 0.5$, we seem to have the best hope of accurately measuring reactive intensity in the field. This translates approximately to values less than 2 kHz.

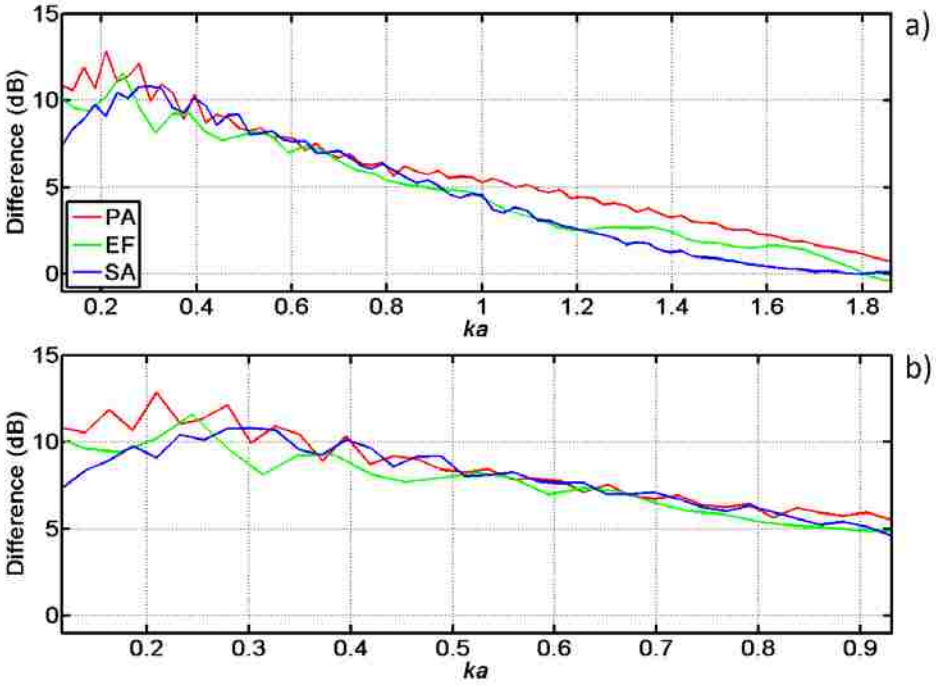

Figure 4.4. Difference between the active intensity level and reactive intensity level for the PA, EF and SA arrays for a) 500 Hz to 8 kHz and b) 500 Hz to 4 kHz assuming a=1.27 cm.

4.3 Kinetic and potential energy density

For a spherically spreading source, a distance r away from an ideal energy density array, we expect the difference in the level of kinetic and potential energy densities to be as presented in Figure 4.5. For our experimental setup and frequencies above 50 Hz, we are well outside this range ($kr \gg 3$) and expect even less difference between the quantities shown for our "plane wave" approximated field.

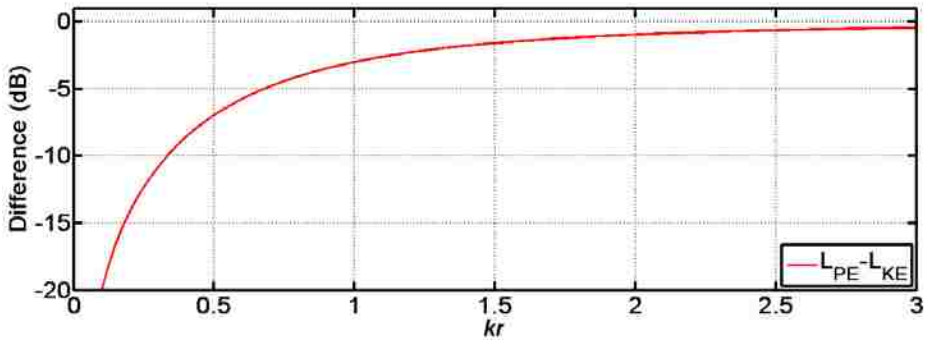

Figure 4.5. Expected difference between potential and kinetic energy density levels for a spherically diverging wave as a function of kr. The variable r corresponds to the distance from the source, not the array size.

A true plane wave has the characteristic of having equal values for kinetic and potential energy density. The experiment of Chapter 3 was constructed to produce a "locally planar" acoustic field at the measurement point. We can assume that the kinetic and potential energy density levels ought to be equal for frequencies above 500 Hz. A simple comparison of the kinetic energy density level and the potential energy density level will show us over what range we can most trust these quantities. The decibel difference between these two levels is given in Figure 4.6.

For each of the arrays in Figure 4.6, the kinetic energy appears to dominate the field and suggests that either we are too near the source, or there is a bias in the estimation of one of these quantities. The SA array shows the best agreement for $ka < 0.6$ and it may be due to limited scattering in that region; recall from Chapter 3 that scattering effects began to be significant around 2 kHz, or $ka = 0.46$.

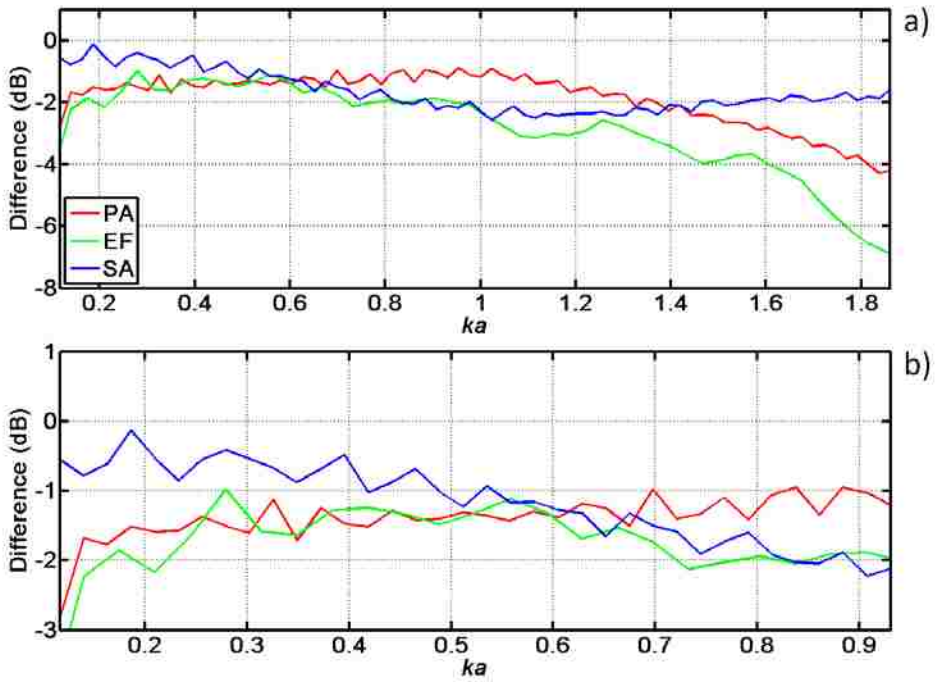

Figure 4.6. Difference between the potential and kinetic energy density levels for the PA, EF and SA arrays for a) 500 Hz to 8 kHz and b) 500 Hz to 4 kHz assuming a=1.27 cm.

4.4 Energy density

Energy density and active intensity of a plane wave are directly related by the relationship

$$I = cE. \tag{4.3}$$

If we consider the energy density level to have a reference "E_{ref}" of $\frac{I_{ref}}{c}$ we can compare levels of these quantities. The difference between sound intensity level and sound energy density level is given in Figure 4.7; for 0.2 < ka <1.2, the relationship in Equation 4.3 appears to be valid with <1 dB difference.

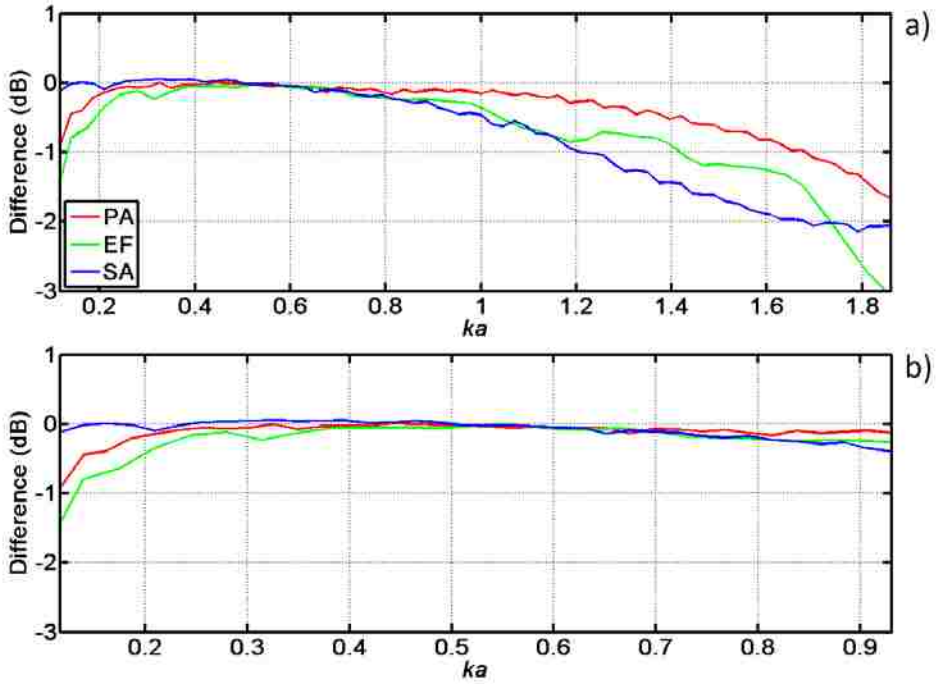

Figure 4.7. Difference between sound intensity level and sound energy density level for the PA, EF and SA arrays for a) 500 Hz to 8 kHz and b) 500 Hz to 4 kHz assuming a=1.27 cm.

It is very interesting that the difference of these levels in Figure 4.7 is near-zero given that the difference in energy quantities of Figure 4.6 suggested a bias error in either the kinetic or potential energy density quantities. An overestimation of one quantity and an underestimation of the other may be the explanation or perhaps total energy density is a more robust quantity than either potential or kinetic energy densities alone for non-ideal/scattered fields that occur due to the presence of the microphone array. Another explanation is that intensity and energy density both rely on pressure and particle velocity estimates and may be equally in error and so their difference is small and implies each quantity is equally in error.

4.5 Recommendations

It is recommended that care be exercised when discussing the interpretation of the energy-based metrics of Chapter 3 or with future measurements using these sensors. In general, we find

that the arrays perform best for approximately $0.2 < ka < 0.5$; this corresponds to roughly 850 Hz to 2.1 kHz for the SA and PA arrays. For the EF array, this bandwidth is 566 Hz to 1.4 kHz. The cause of error in the components of energy density is not well understood for these particular designs and perhaps serve best as qualitative assessments of a noise field. From Figure 3.4 we see that a high-frequency cutoff of around 2 kHz would limit errors due to scattering which may be better or worse depending upon angle of incidence of the wave. Assuming this analysis translates to the high-amplitude, shock laden, rocket noise environment described in the next two Chapters, the results are most reliable in the region below 2 kHz but may be shown with reasonable reliability up to 4 kHz based on these laboratory measurements.

5 Experimental analysis of a small test motor

5.1 Introduction

A preliminary investigation has been made by Gee et al.[30] demonstrating the ability of microphone arrays to measure various energy-based acoustic metrics near a solid rocket motor. In this Chapter, we consider the validity of the measurements taken by analysis of sound pressure levels and transfer functions. The work of Gee et al. is then revisited to correct the direction of the acoustic intensity vector presented in their paper. For various frequencies of interest, active and reactive acoustic intensity are presented and shows the flow of energy near the rocket motor. Energy density, Lagrangian energy density, kinetic energy density and potential energy density are also presented and give insight into the characteristics of the noise field and our measurement arrays during test conditions. Lastly, ray tracing of the active intensity vector is discussed as a method for determining source location of this rocket noise field.

Expressions used for calculating active and reactive acoustic intensity, energy density, Lagrangian energy density, kinetic energy density and potential energy density in this analysis are developed in Appendix A of this thesis. As is common in the analysis of rocket/jet noise measurements, the distance of the microphones to the rocket nozzle are given in nozzle diameters, *D,* and will be used throughout this chapter.

5.2 Test setup

While working on related projects, BYU has had measurement opportunities at Alliant Techsystems (ATK) in Promontory, Utah to test preliminary array designs in multiple solid rocket motor environments. Typically, once a motor has been fired in a particular test bay, it is months before another motor is readied for firing and another measurement can be made at the

same location. However, as part of propellant development, multiple small, 12.7 cm diameter center perforated, or “CP”, motors are often fired in relatively quick succession from a common nozzle. The process is much like loading a large stationary gun with a new round after each firing.

A rectangular rig consisting of four 4-microphone arrays was constructed and aligned along the shear layer of the exhaust plume as depicted in Figure 5.1. These arrays were on a sled which was able to be methodically moved farther downstream with each firing while stationary microphones verified the repeatability of each test. The sled was moved along a line 12° off the direction of fire which is assumed to be parallel (based on spalling of the concrete test pad) to the shear layer. An offset of 15 cm was allowed to prevent the microphone arrays from being too near the shear layer. The resulting data set represents a long array of sensors which covers a significant distance along the plume and gives great opportunity to learn more about the acoustic field of this particular solid rocket motor and test bay facility.

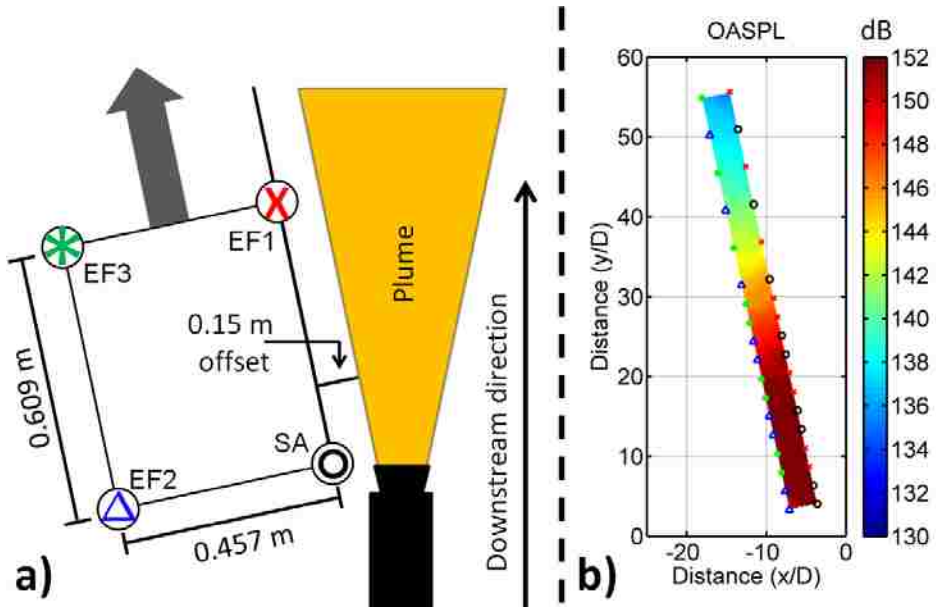

Figure 5.1. a) Top-down view of the measurement setup. Each symbol corresponds to a different microphone array, either the spherical array (SA) or one of the three external frame (EF) arrays. The arrow shows the direction the rig was moved between firings. b) Plot of the overall sound pressure level (OASPL) in dB re 20 μPa. Notice the symbols in (b) correspond to the symbols in (a). The scaling parameter D corresponds to the nozzle diameter of the motor, 12.7 cm.

There are two types of microphone arrays used throughout this chapter's analysis of solid rocket motor noise fields; the spherical (SA) and external frame (EF) designs of Figure 3.1. The SA array is an irregular tetrahedron with a tetrahedral angle of 120° between any two microphones and has a diameter of 2.54 cm. The EF designs are regular tetrahedrons and are variable in their size; for this experiment they were set at a diameter of 2.54 cm to match the physical dimensions of the SA array. The three EF arrays are EF1, EF2 and EF3. Data for these tests were recorded by multiple National Instruments PXI-4462 cards at a sampling rate of 204.8 kHz. The transducers used were GRAS 6.35mm 40BH microphones for the SA and EF1 array and 6.35mm GRAS 40BD microphones that had been specifically chosen for their lower

sensitivities (approximately 0.5mV/Pa) for the EF2 and EF3 arrays. The 40BD constant current microphones were powered by the data acquisition system whereas the 40BH microphones require a separate 200V polarization voltage supplied by two GRAS 12AA power supplies for each array.

Each array was mounted such that microphones 2 and 4 form a line parallel to the presumed shear layer of the flow. On the SA array, microphone 2 faces the plume. For the EF(1,2,3) arrays, microphone 3 faces the plume most directly. Microphones 2 and 4 are always nearest the shear layer, as seen in Figure 5.2. Microphone array geometry is given in Appendix A of this thesis.

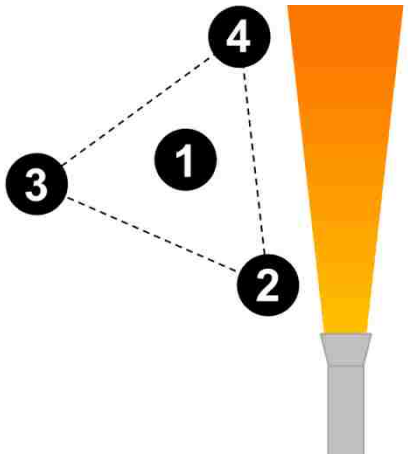

Figure 5.2. Depiction of how the arrays are oriented relative to the rocket motor. Microphone 2 and 4 form a line parallel with the presumed shear layer of the rocket plume. (Not to scale) A right-handed coordinate system is used to define microphone locations. The y-axis follows the centerline of the plume, positive downstream; the z-axis is positive out of the paper

At a location of 43.2 *D* downstream and 31.2 *D* off the center line of fire, a stationary microphone recorded each firing and showed similar spectra between 18 firings, as shown in Figure 5.3. There is a high reproducibility of the acoustic field generated during these firings and

this consistency allows for magnitude and vector maps of the aforementioned energy quantities to be generated by repeated movement of the acoustic arrays between firings. The nulls that are seen in Figure 5.3 around 200 Hz and 600 Hz are likely a result of constructive/destructive interference caused by the interaction of sound arriving direct from the rocket plume and sound reflected off of the ground or nearby structure. The location of the nulls will vary with microphone height and distance from the source, therefore the interference patterns will occur at different frequencies for the measurement arrays.

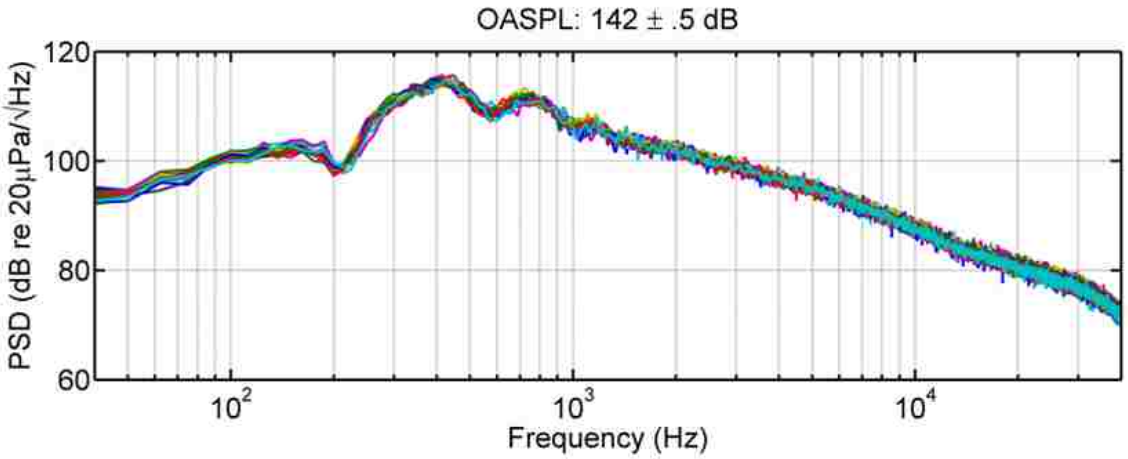

Figure 5.3. The power spectral density (PSD) of a reference microphone situated 43.2 *D* downstream and 31.2 *D* off the center line-of-fire for 18 firings. These data vary by less than 0.5 dB in the overall sound pressure level (OASPL) between firings. As shown, the spectra between firings are also similar.

The power spectral density (PSD) obtained for the top microphone of the SA array (the array nearest the plume) is shown in Figure 5.4 for the 18 trials under analysis in this chapter. Depending upon location of the microphone, the peak frequency appears to shift between approximately 150 Hz and 3 kHz. This shift in peak frequency is expected. In general, high frequencies are generated nearer the nozzle and low frequencies farther downstream. This phenomenon will be made clear in the discussion and figures that follow. The high-frequency

roll off (at ~20 dB/decade) is typical for high-amplitude rocket and jet noise fields and may be related to nonlinear acoustic phenomena.[31]

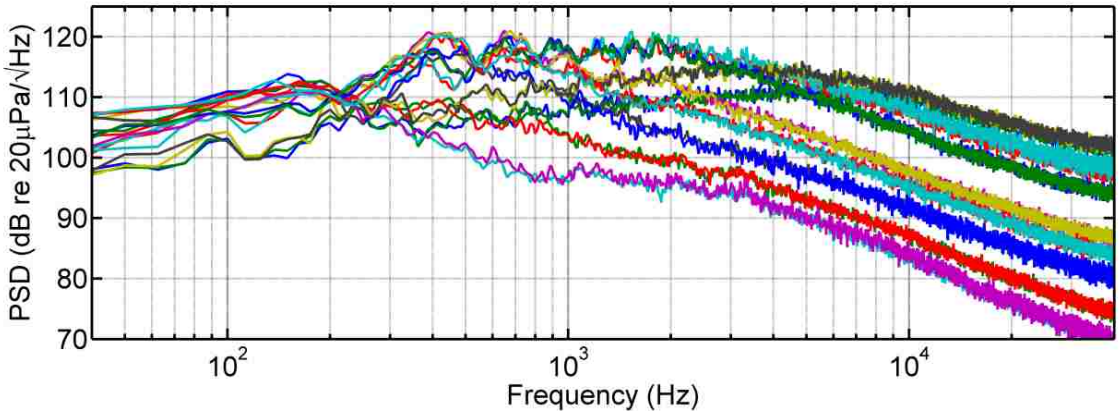

Figure 5.4. Eighteen measurements from the microphone atop the SA array for two trials at each of 9 locations.

5.3 Assessment of the small test motor measurements,

The data from the solid rocket static test firings resulted in a map of acoustic quantities near the plume of the motor. As is typical with experimental testing, there are often small errors which need to be accounted for during the processing of the data. Through this section, we will address why certain measurements are omitted from the final analysis.

5.3.1 Sound pressure levels

For the locations that correspond to the sphere being at its shortest distance from the nozzle, the sound pressure level is calculated for each of the four microphones on each of the four arrays used during the measurements. The three EF arrays (b,c,and d of Figure 5.5) have good agreement between each channel at low frequency and begin to deviate around a few kHz, likely due to scattering. The notable exception is microphone 4 on the EF1 array which does not match until approximately 100 Hz. Also, the SA array (a) has more low-frequency (~100 Hz) variation

in the SPL of each channel but then matches until higher-frequency scattering effects begin to be large.

It is likely that the scattering errors will impact the measurement of any acoustic quantity and should be taken into consideration when determining what part of the data may be trusted. The EF1 array will also exhibit low-frequency errors based upon the poor response of the fourth microphone channel. It was found later that a faulty preamplifier was responsible for this error. The error effects appear to be restricted to frequencies less than ~1 kHz, so the analysis of the EF1 array remains included in this work.

Another feature of Figure 5.5 is that each of the arrays has a different region of peak level. For example, the SA array peaks around 6 kHz and the EF1 array peaks around 3 kHz. The shift in the peak is related to the location of the array relative to the rocket motor/plume. In general, high frequencies are primarily generated farther upstream. This generality is confirmed for this specific measurement because although both SA and EF1 are the same offset distance from the plume, the SA array is farther upstream and has the higher peak frequency.

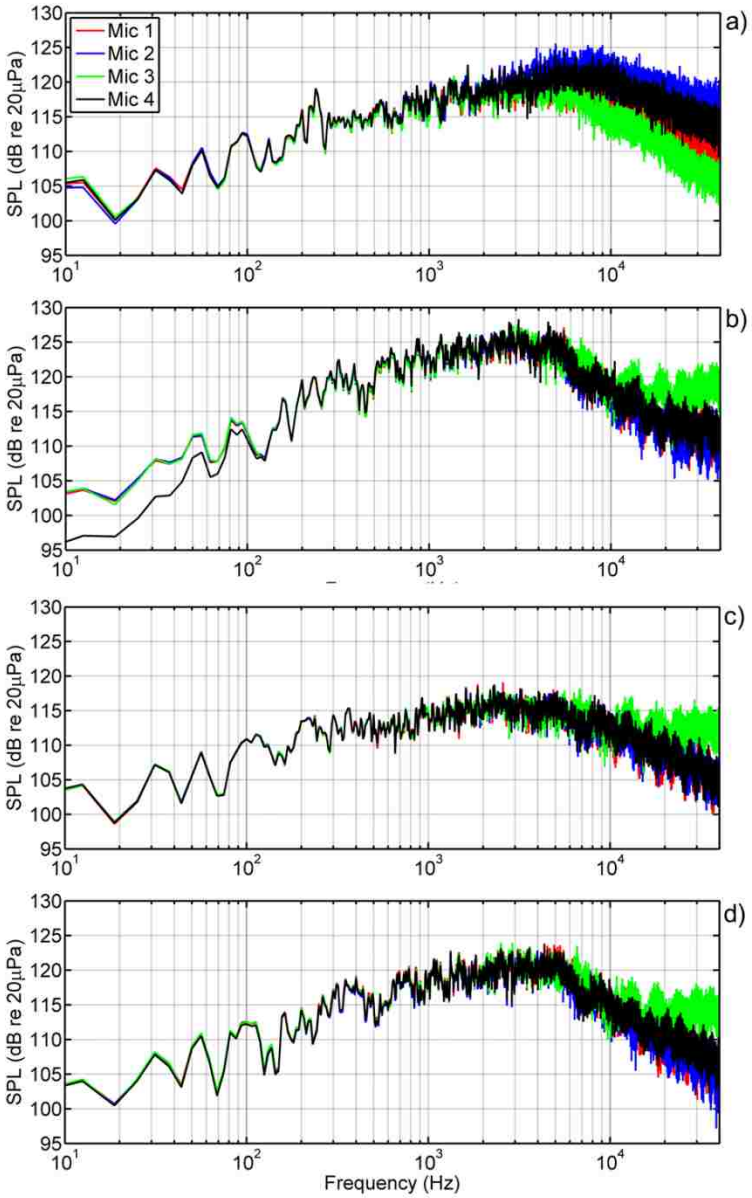

Figure 5.5. Sound pressure level for the 16 microphones in the measurements of the solid rocket motor static firings. The location of the measurement sled is such that the SA array is at its most upstream position. The individual plots are for the a) SA, b) EF1, c) EF2, and d) EF3 arrays. These measurements are for the position closest to the nozzle for each array type as shown in Figure 5.1.

5.3.2 Transfer functions

The greater the differences between frequency responses of microphones in an array, the less accurate the measurements will be in the field. An approximation of the transfer function between each outer microphone and the microphone that lies on the z-axis, microphone 1 in Figure 5.2, were calculated to gain more insight into these relationships. This calculation was done using data from the actual test and contains all field effects. It is expected that at low frequencies, i.e. 10 Hz, the acoustic field should be similar between all microphones and the transfer function should be approximately 1 for magnitude and 0° degrees phase difference. At higher frequencies, it would be expected that the relationship between microphones would diverge with the difference in acoustic fields. Presented below are the magnitude and phase representation of the transfer functions.

As expected, the transfer function involving "Mic 4" in Figure 5.6(b) and Figure 5.7(b) show the most error, having obvious magnitude discrepancy below 200 Hz and phase discrepancy below 600 Hz where at these frequencies they should be very near 1 and 0°, respectively. When analyzing the validity of field measurements, these types of figures should be generated to help ensure that there are no obvious errors. From these figures we also learn that the SA array has more low-frequency magnitude discrepancy below 100 Hz compared with arrays EF2 and EF3. The phase relationship appears more similar between arrays SA, EF2 and EF3.

The setup of these sensors in the field had microphones 2 and 4 in a line parallel to the shear layer. From the phase of the transfer function plots in Figure 5.7, we can see that at higher frequencies for the SA array, there is a positive phase difference for transfer functions H_{12} and H_{14} which indicates that the sound arrives first at these microphones (in that order) relative to the central microphone, 'Mic 1' of Figure 5.2.Transfer function, H_{13} appears to have sound arriving

later which is also consistent with the setup of the sensors. For each of the EF arrays H_{12} and H_{13} look acceptable but H_{14}seems very near zero and perhaps more negative for frequencies above 6 kHz. Overall, the orientation of the arrays in the field appears to be valid.

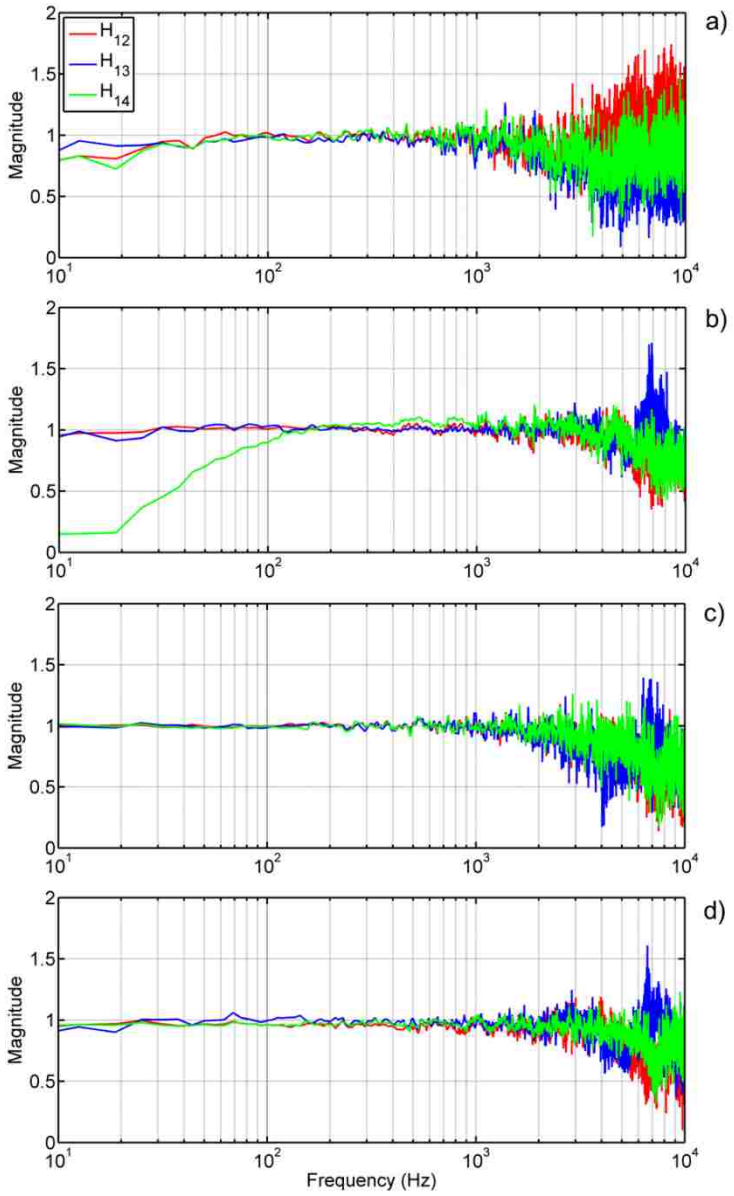

Figure 5.6. Transfer function magnitude for the 16 microphones used in the near-field measurements of the solid rocket motor static firings. The individual plots are for the a) SA, b) EF1, c) EF2, and d) EF3

arrays. These measurements are for the position closest to the nozzle for each array type as shown in Figure 5.1.

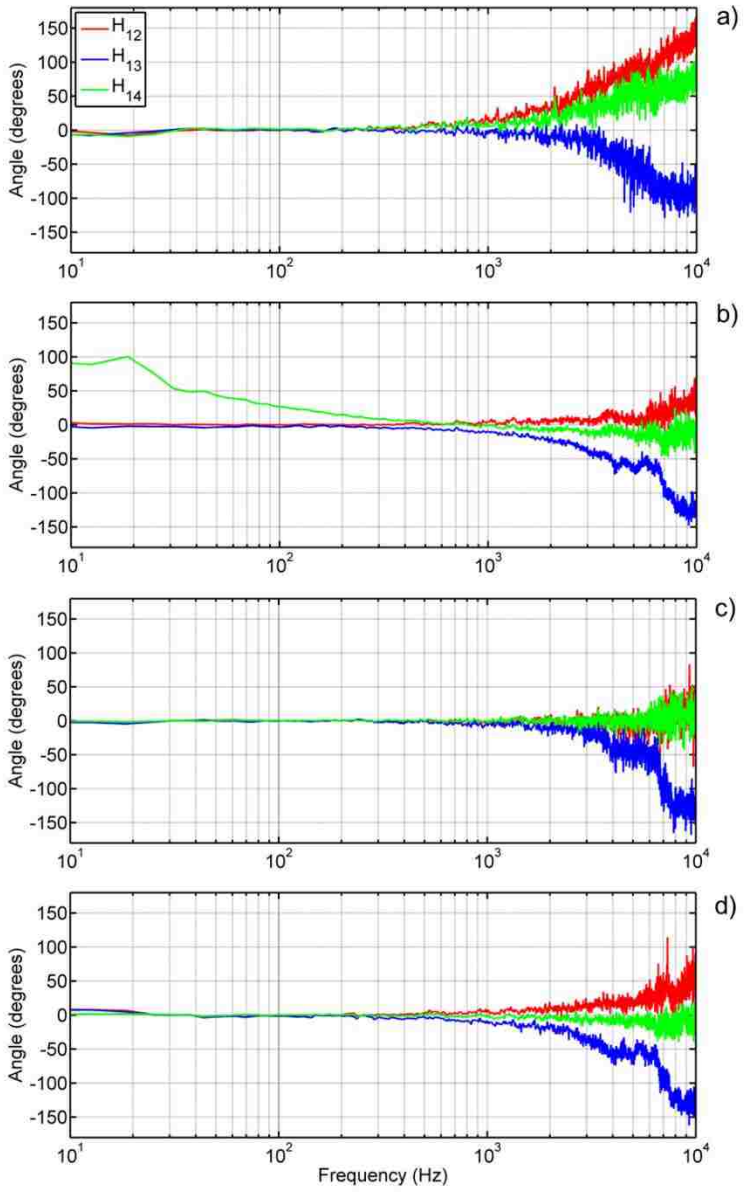

Figure 5.7. Transfer function phase for the 16 microphones used in the near-field measurements of the solid rocket motor static firings. The individual plots are for the a) SA, b) EF1, c) EF2, and d) EF3 arrays. These measurements are for the position closest to the nozzle for each array type as shown in Figure 5.1.

Based upon the analysis of the spectra and transfer functions of the microphones used in this array, we feel confident that the results for the EF1 array should not be trusted below 1 kHz and the other arrays will likely be most correct in the 100 Hz to 2 kHz range. The full impact of the scattering errors is unknown, but from the analysis in Chapter 3 of this thesis, it does not appear to be the only high-frequency limiting error source.

5.4 Revised data analysis

This data set was initially analyzed for overall sound pressure and intensity levels by Gee *et al*. in a recent JASA Express letter. This letter also included a brief analysis of the acoustic intensity vector near the motor and observed that 1) the source region contracts and moves upstream as frequency increases, 2) there is possible evidence for refraction of the sound waves outside the plume and 3) the region of highest overall sound pressure level is more upstream than the region of peak intensity. Errors in the initial analysis have been discovered relating to the direction of the intensity vector; corrected intensity vector plots are given here. The discussion and implications of the work remain unchanged from Gee's preliminary analysis.

The length of the direction vectors are proportional to the fourth root of the sound intensity level (re I_{ref} =1 pW/m^2) which is calculated from root sum of squares of the $\hat{\boldsymbol{x}}$ and $\hat{\boldsymbol{y}}$ intensities such that

$$|\hat{I}| = \left(10 \log_{10} \left(\frac{\sqrt{I_x^2 + I_y^2}}{I_{ref}} \right) \right)^{\frac{1}{4}}, \tag{5.1}$$

and the angle associated with the quantity (as projected onto the x-y plane) is given by

$$\angle \hat{I} = \tan^{-1}\left(\frac{I_y}{I_x}\right). \tag{5.2}$$

This method of separately obtaining the magnitude and angle of the intensity vector results in correct scaled magnitude whilst maintaining accurate direction. The color plots are interpolated and plotted by MATLAB's 'pcolor' function using

$$I = 10\log_{10}\left(\frac{\sqrt{I_x^2 + I_y^2 + I_z^2}}{I_{ref}}\right) \tag{5.3}$$

as the input.

A significant difference between these plots and that of Gee et al. is the exclusion of EF1 (see Figure 5.1) until ~1 kHz. From our previous analysis of this sensor, we see that the magnitude and phase of the transfer functions involving this microphone are suspect of error below 1kHz. Gee used an alternate processing method to correct for this single low-frequency error; however, this method is beyond the scope of this analysis and can be found as the "wave vector method" in a thesis by Thomas.[32]

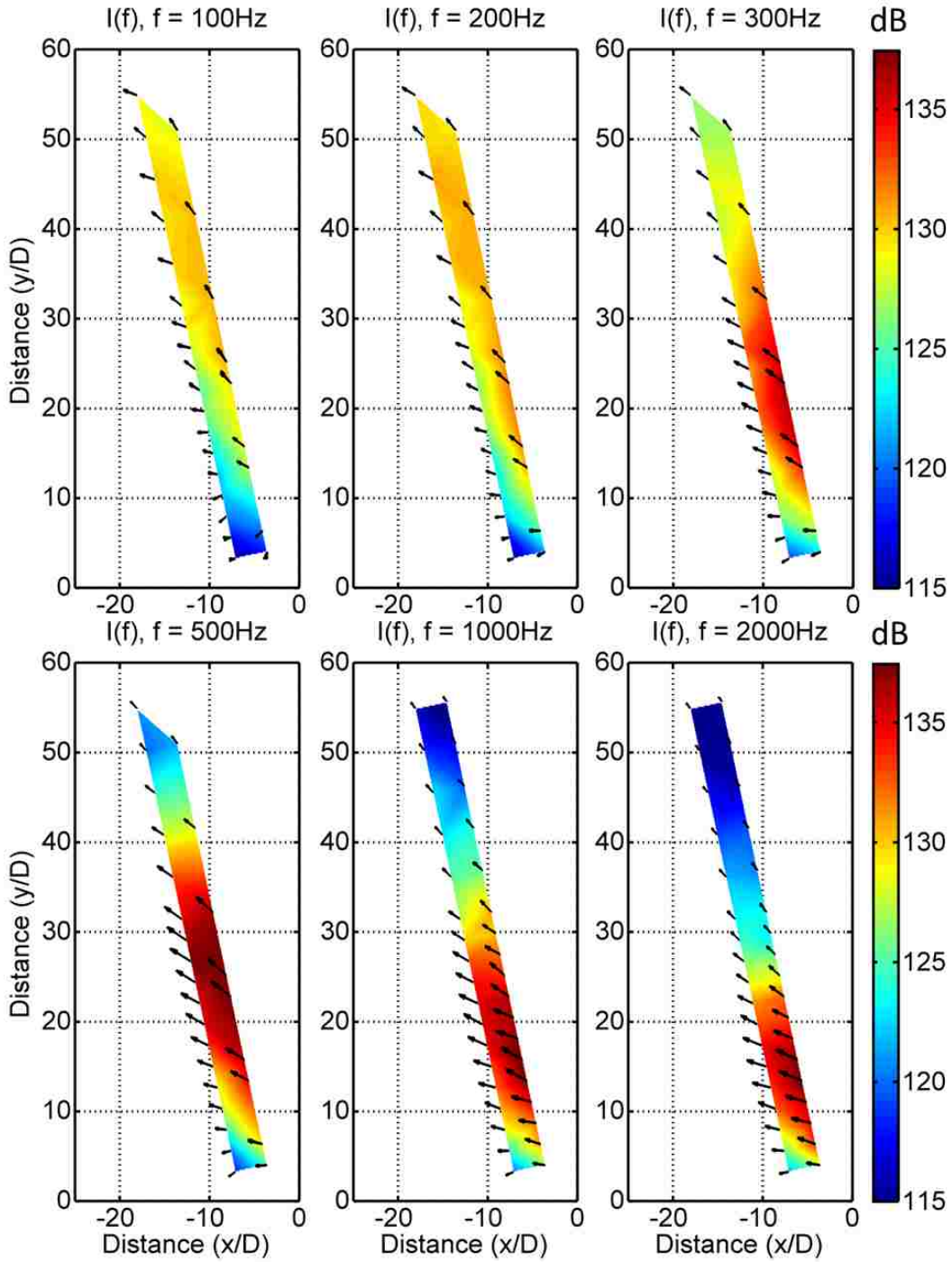

Figure 5.8. The scaled active acoustic intensity vector is given to correct those presented by Gee et al. The direction vectors are scaled by the fourth root of the magnitude of the sound intensity level and the color maps are sound intensity levels in dB re 10^{-12} W/m^2. At frequencies below 1 kHz, the EF1 array data is

unreliable and not included in these figures. Also, recall that the scaling factor, *D*, is the nozzle diameter of the rocket motor.

5.5 Energy-based results

Acoustic intensity is but one of several energy-based metrics that may be used to describe an acoustic field. It is possible that the use of other energy-based measures will give additional insight into the physical properties of the rocket noise field. In this analysis we will look at the following acoustic quantities: intensity, in its active and reactive components, kinetic energy density, potential energy density, total energy density and the Lagrangian density. The derivation of these acoustic quantities assuming a time averaged case may be found in Appendix A of this thesis.

It is impossible to give a narrowband analysis of each frequency. However, in Figure 5.3, which depicts a far-field measurement of each of the 18 firings, we see that 400 Hz is near a frequency of peak amplitude and other frequencies of greatest interest span around the 400 Hz to 3 kHz range. By considering 100 Hz, 200 Hz, 400 Hz, 1 kHz, 2 kHz and 4 kHz, we will see limitations of the arrays to estimate these quantities while simultaneously gaining physical insight into the noise field.

In their work, Mann and Tichy[29,33] discuss the interpretation of the complex intensity vector in both its active and reactive parts. The interpretation of these time-varying quantities is that the active intensity vector points perpendicular to surfaces of constant phase and shows the direction of energy flow and the reactive intensity vector points perpendicular to surfaces of constant pressure and in the direction of decreasing pressure. These interpretations of the vectors are for time varying quantities and are not necessarily the same for time-averaged quantities. Indeed, for a time averaged measurement, the reactive intensity, a zero-mean oscillating quantity, is zero.

The accuracy of the reactive intensity direction vectors is not fully understood, nor their interpretation for this noise field. They are presented here for the purpose of documenting results which appear to be from a valid measurement set with a valid processing technique. It may be that the influence of the half-space/semi enclosed environment modified the field beyond what would be expected near a rocket plume. However, these remain measurements of a real (albeit complex) noise field and are not discounted completely. In general, the reactive intensity vectors presented appear to make more physical sense as frequency increases and at locations nearer the rocket nozzle. The upstream vectors at high frequencies point in the direction of decreasing pressure, as is consistent with Mann and Tichy's analysis[29]. At, low frequencies or far from the source, calibration, field or measurement effects may overwhelm this quantity. Possible insights into the unexpected response of the reactive intensity vectors follow the presentation of the vector at a discrete frequency.

Also important to note is that the levels are calculated using the magnitude of the combined x, y and z directions and are projected onto the x-y plane. Further insight into the rocket field may be found by comparing the z-intensity with what is expected from ground reflections but this is beyond the scope of this thesis. Here we use total levels for a more accurate comparison of each of the energy quantities at the discrete frequencies shown. The references used to calculate each level are $I_{ref} = Q_{ref} = 10^{-12}\,\frac{w}{m^2}$ and $E_{Tref} = E_{Kref} = E_{Pref} = E_{Lref} = \frac{I_{ref}}{c}$, where c is the speed of sound.

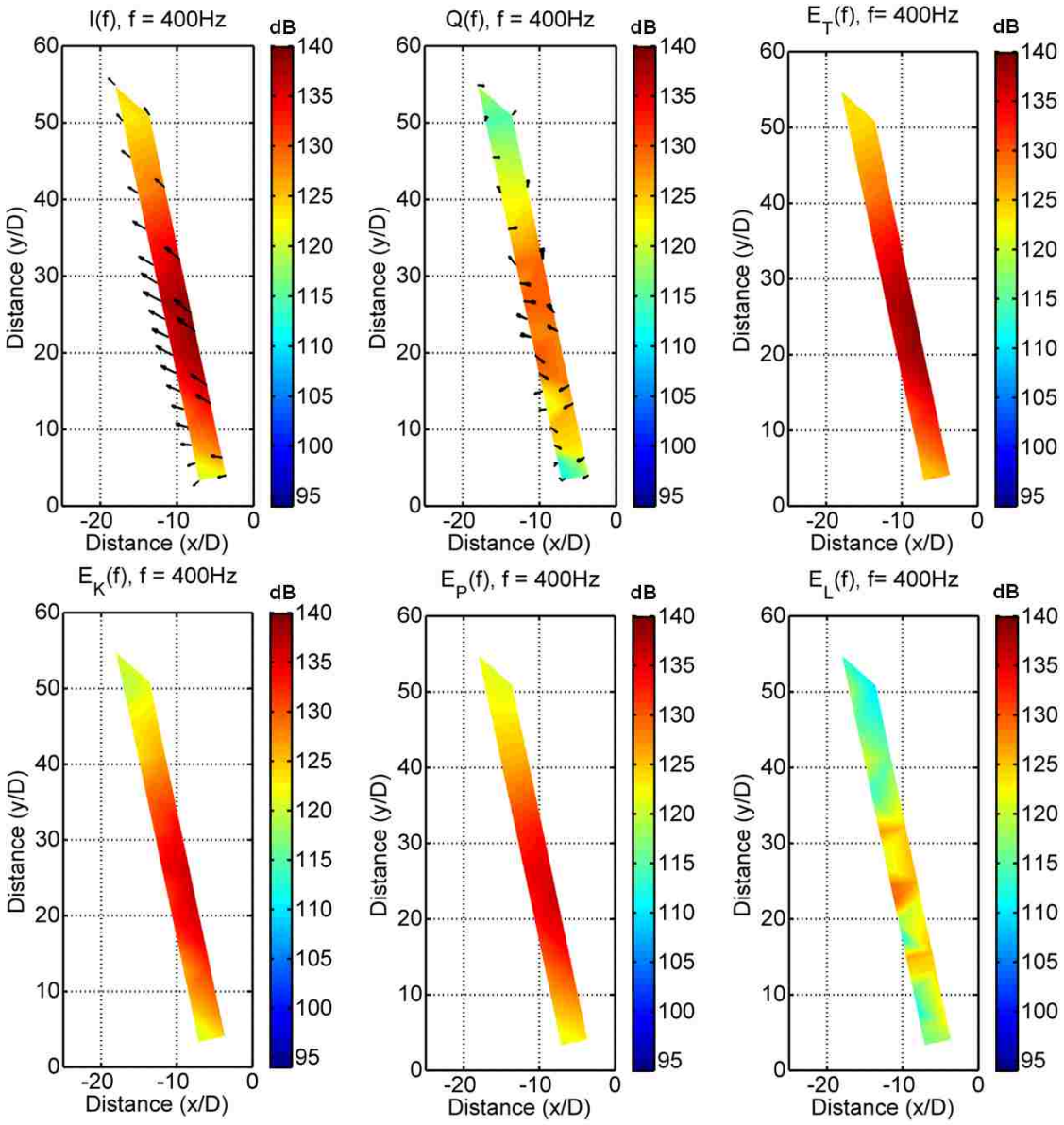

Figure 5.9. Active intensity, reactive intensity, energy density, kinetic energy density, potential energy density and Lagrangian energy density levels are given for the rocket noise field of Figure 5.1 at 400 Hz. The peak levels for this rocket motor occur near this frequency.

From Figure 5.3 we see that the maximum sound pressure level, for the referenced location, occurs around 400 Hz. In Figure 5.9, we see that in this 400 Hz region the active intensity shows a well-defined source region about 25 *D* downstream. This suggests that the primary noise

generation mechanism is located some distance downstream from the exit nozzle of the rocket motor. Another interesting feature of the active intensity is that the four array locations farthest upstream appear to give evidence of refraction of the noise in the upstream direction. From an engineering perspective, it would be advantageous to know how much noise generated by the exhaust plume is directed back towards the payload of the launch vehicle.

The reactive intensity vectors of Figure 5.9 are difficult to interpret and it appears they may be dependent upon array type; there are alternating directions of this vector that appear to correspond with different arrays. It is possible that the variation of these measurements is explained by assuming we are in the acoustic far field of the source, where the reactive intensity approaches zero. However, because the reactive intensity is proportional to the gradient of the pressure[34], the array which measures the reactive intensity vector as moving towards the source likely has a calibration error. A careful look at Figure 5.6c shows that $H_{1,3}$ has a slightly higher magnitude response for microphone 3 at frequencies around 100 Hz. The effect of this is the gradient is towards the plume rather than away.

It is interesting to note that the general trend for areas of high and low intensity are in the same downstream region as that of active intensity (as well as the energy density quantities). Reactive intensity magnitude has been shown to pinpoint more accurately acoustic sources in machine noise[34] and here we would assume the noise source to be found between 20 to 30 D downstream. This seems consistent with each of these energy quantities being presented and suggests that the magnitudes are qualitatively correct.

Kinetic and potential energy density levels of Figure 5.9 are similar in level at this frequency, particularly in the downstream region. The Lagrangian energy density is defined as the difference between the kinetic and potential energy densities. Shown in Figure 5.9 is the level of

the absolute value of the Lagrangian energy density; it is always positive and lower levels indicate greater similarity between the kinetic and potential energy densities. (Note that Figure 5.16 shows the decibel difference between potential and kinetic energy densities for a particulate measurement point. It will be discussed later.)

In Figure 5.9, the point farthest downstream on the plume side of the measurement grid of the Lagrangian is 110 dB which is ~10 dB less than the kinetic and potential energy densities at the same location. This similarity in level between the two energy quantities may be indicative of locally planar wave behavior developing as we move farther into the far field of the source. Lagrangian energy density in the region of peak level, roughly 25D downstream, is also down by a similar level of approximately 10 dB. Another argument may be that all of our measurement positions are "acoustically far" from the source at 400 Hz. Indeed, at 25D downstream (the peak source region), the nearest measurements locations are roughly 10 nozzle diameters away and at 400 Hz, this corresponds to ~1.5 wavelengths between source and receiver. For these locations and conditions, the quantity kr has a value of 9.3 which in Section 4.3 we learned that for $kr >> 3$ we expect kinetic and potential energy densities to be very nearly equal assuming a monopole source. These results seem consistent with that discussed in Chapter 4.

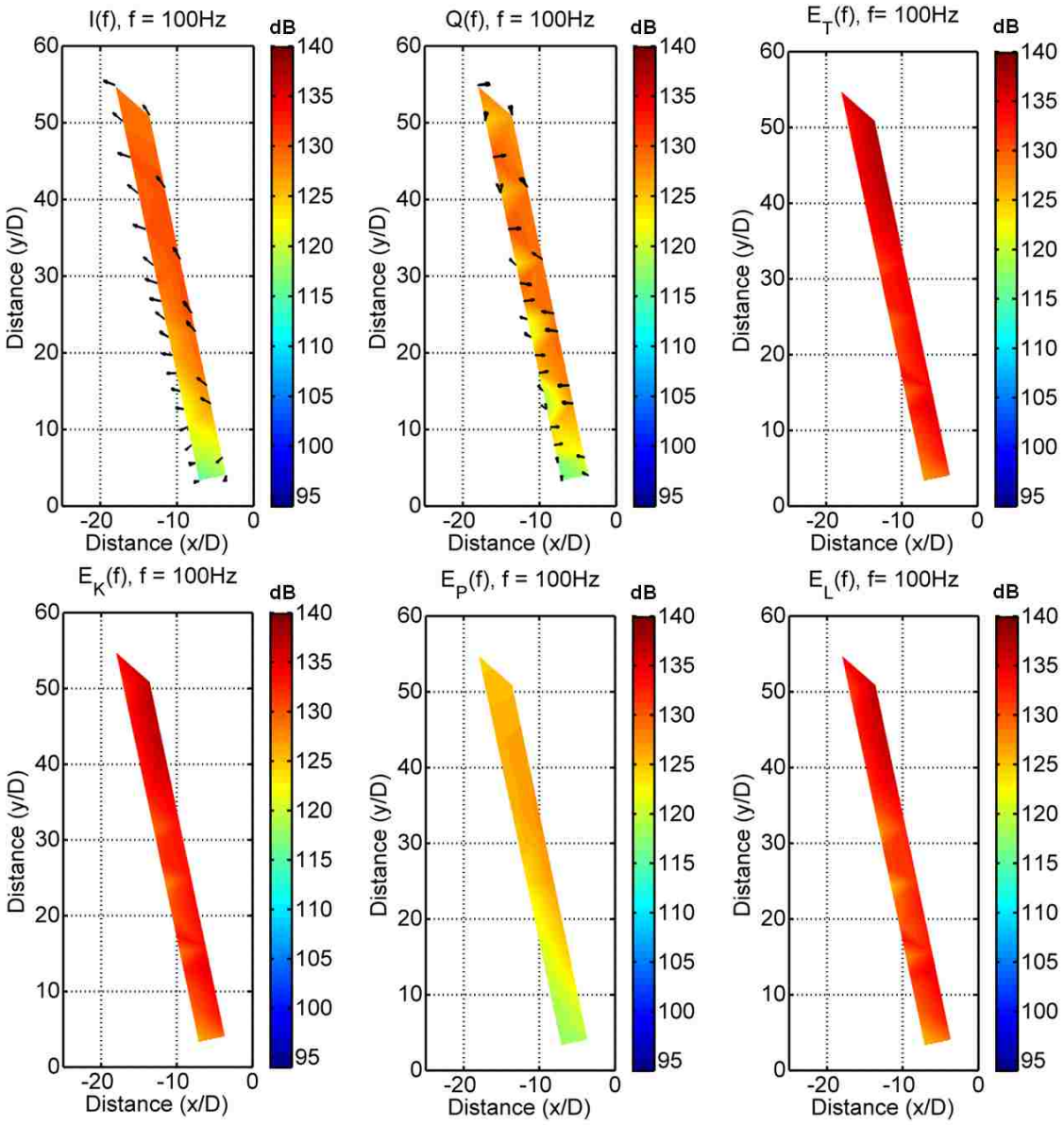

Figure 5.10. Active intensity, reactive intensity, energy density, kinetic energy density, potential energy density and Lagrangian energy density levels are given for the rocket noise field of Figure 5.1 at 100 Hz.

As we turn to Figure 5.10 and focus on these energy metrics at 100 Hz, we see some interesting features of the noise field. The active intensity level is larger downstream, indicating low-frequency noise generation occurs more strongly downstream. We also notice that from the

vectors nearest the plume to those on the outside, there is a rotation of the vectors away from the region of highest level. This effect may be diffraction and is consistent with what we saw at 400 Hz but shifted upstream for the higher frequency.

Similar to the analysis at 400 Hz, the reactive intensity vectors of Figure 5.10 are difficult to explain physically and will continue to be so for most frequencies analyzed. As mentioned earlier, it may be that for some frequencies, that there is something akin to either a calibration or a signal-to-noise problem with the measurement of the reactive intensity. The energy density terms show that at these low frequencies, the kinetic energy density is roughly 10 dB greater than the potential energy density which is qualitatively consistent with what is expected from a simple monopole source; i.e. near the source, most of the energy is kinetic. At this frequency, 100 Hz, we can likely consider ourselves in the acoustic near field. If we assume the source region is somewhat central to our measurement grid and lies on the axis of the plume, we are within 1 wavelength of the source at each measurement location. A single wavelength from the source corresponds to a kr value of less than 2π. For the monopole case in Section 4.3, we did not expect to see a difference of 10 dB between kinetic and potential energy densities until kr was approximately 0.7 or less. This may suggest that the source region of the noise at 100 Hz is not generated at the center of the plume, but nearer the shear layer.

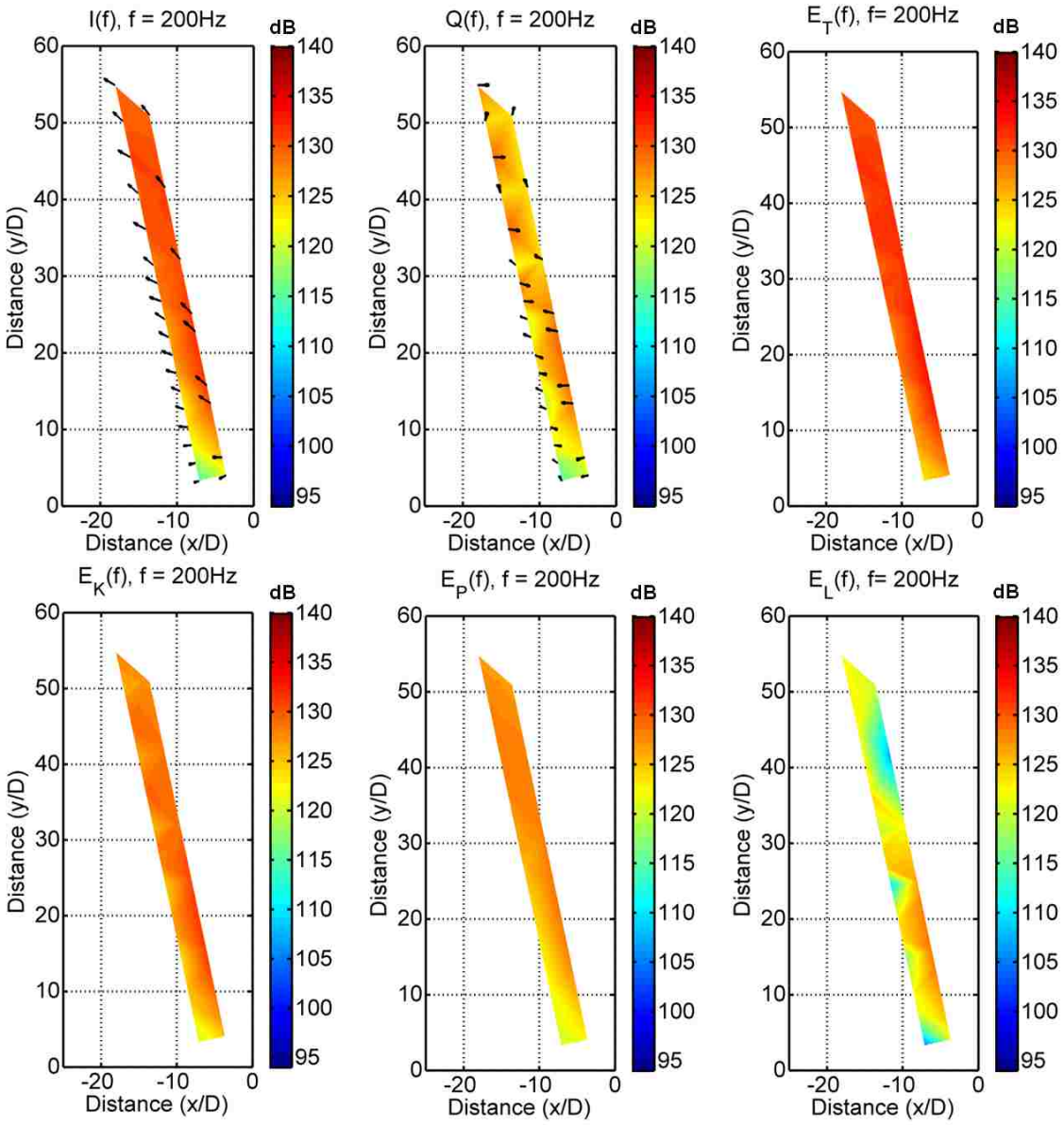

Figure 5.11. Active intensity, reactive intensity, energy density, kinetic energy density, potential energy density and Lagrangian energy density levels are given for the rocket noise field of Figure 5.1 at 200 Hz.

Figure 5.11 shows results at 200 Hz. At this frequency, the active intensity vectors continue to suggest refraction of the sound. This is evidenced by the direction of the active intensity vector which points more upstream at the upstream measurement locations. Reactive intensity

direction vectors remain inexplicable yet follow general trends in level as compared with the active intensity. Kinetic and potential energy densities are beginning to become more equal in level. Another interesting feature that is more defined in this figure than those prior is the "scalloping" that occurs. The scalloping of the active intensity and kinetic energy is partially an artifact of using interpolated plotting routines but is also impacted by ground interference nulls as were explained in conjunction with Figure 5.3. Strictly speaking, the only valid points are those for which a vector exists; the rest are interpolated for aid in qualitative interpretation and comparison of the quantities.

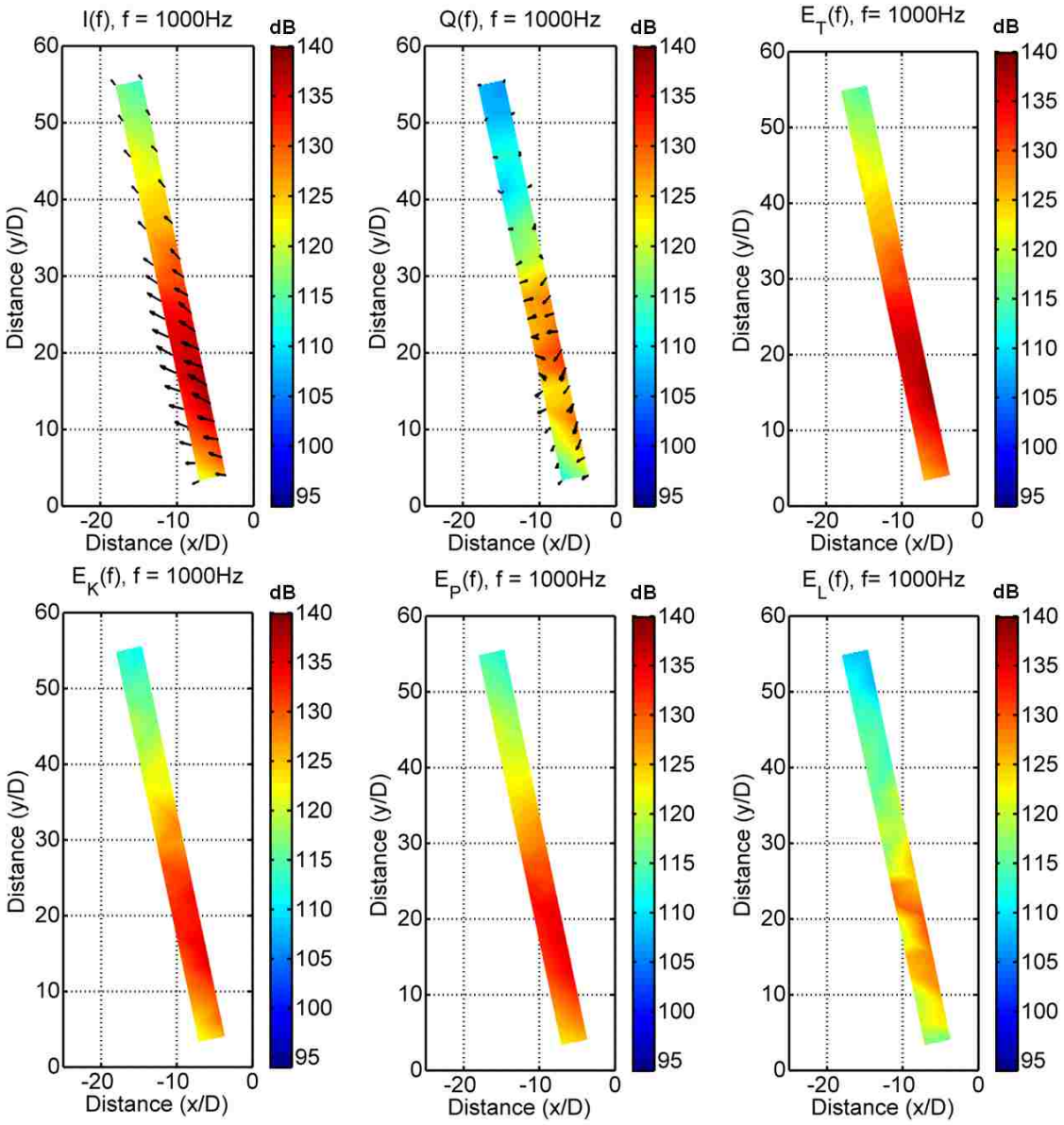

Figure 5.12. Active intensity, reactive intensity, energy density, kinetic energy density, potential energy density and Lagrangian energy density levels are given for the rocket noise field of Figure 5.1 at 1 kHz.

Figure 5.12 shows the measurements at 1 kHz. These figures are similar to those seen in Figure 5.9 at 400 Hz, but the peak region of acoustic intensity is now closer to 20*D* downstream than the 25*D* we saw at 400 Hz. We have also included the results of the EF1 array in the test

analysis. The reactive intensity demonstrates an interesting response with all the upstream vectors pointing away from the plume in approximately the direction of decreasing pressure (as expected), and then midway downstream, the vectors point inwards. For this frequency it is as if our measurement array borders on the region for which we may accurately measure the direction of the reactive intensity vector. However, it is uncertain why the vectors point in opposite directions in the region of higher level, depending upon which side of the rig they are on. Notice that for each of these metrics, as the frequency increases, the peak region contracts and moves upstream as was discussed by Gee et al.[7].

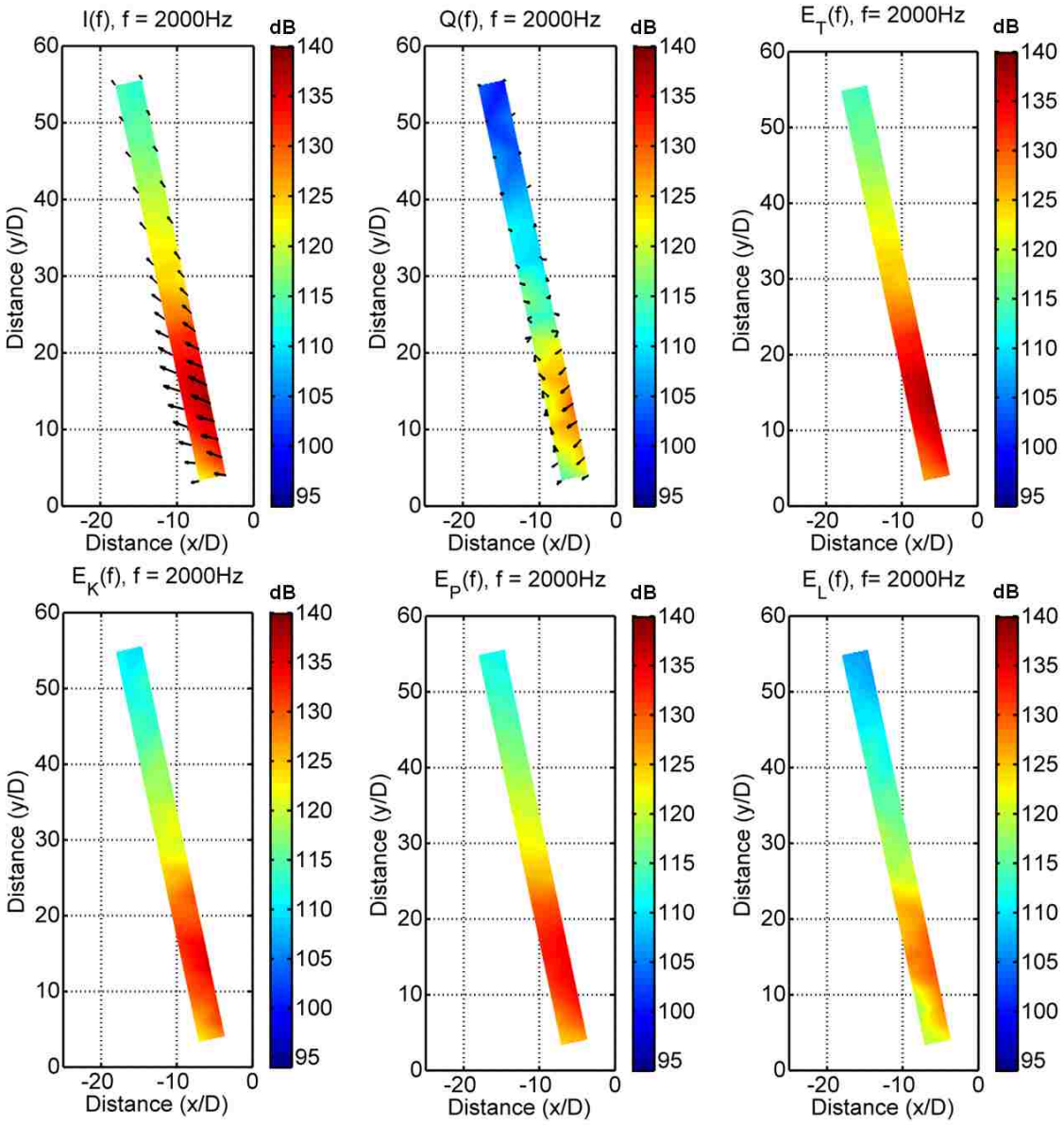

Figure 5.13. Active intensity, reactive intensity, energy density, kinetic energy density, potential energy density and Lagrangian energy density levels are given for the rocket noise field of Figure 5.1 at 2 kHz.

The general trends continue from 1 kHz, up to 2 kHz for each of these quantities of Figure 5.13. Above this frequency, we begin to assume that there are increasingly more errors in the measurement based upon the transfer function, sound pressure level and laboratory analysis

discussed in Chapter 3 and Chapter 4 of this thesis. However the best measurement range is in the 500 Hz to 2 kHz region according to our measurements from Chapter 3. We may extend this region to 5 kHz by allowing for ±3dB magnitude error and ±5° directional error for the intensity metrics.

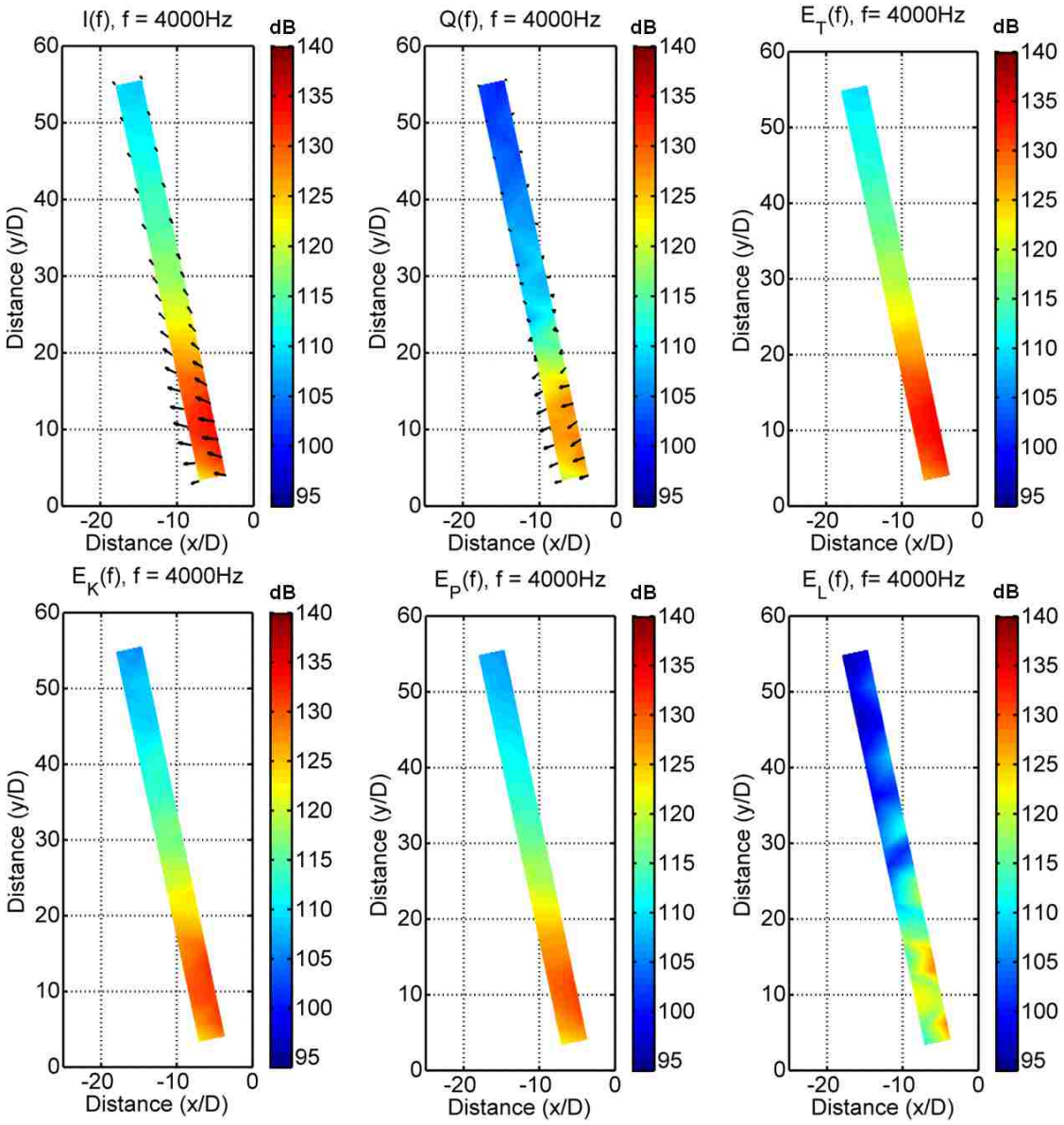

Figure 5.14. Active intensity, reactive intensity, energy density, kinetic energy density, potential energy density and Lagrangian energy density levels are given for the rocket noise field of Figure 5.1 at 4 kHz.

As we continue on to view results at 4 kHz in Figure 5.14, we see the shifting and contracting of the peak source region continue. It is interesting that the reactive intensity vectors in the source region all point away from the plume. If a time domain analysis of the reactive intensity

vector may be used, the vectors point in the direction of decreasing pressure and are perpendicular to surfaces of constant pressure; more like a monopole, less like a plate. It may be an interesting and worthwhile endeavor to pursue this topic in future research to learn more about the pressure gradients near a rocket noise source and why these arrays agree better at higher frequencies.

It should be noted again that as frequency increases, the estimation for each of these energy quantities begins to deteriorate. As we investigate the total levels of each of these quantities, it should be noted that these low and high-frequency errors will skew the overall result and may not represent the overall sound field completely accurately. To investigate overall trends, "band limited" overall sound energy level and intensity plots for the 300 Hz to 5 kHz range have been constructed in Figure 5.15.

The reactive intensity of Figure 5.15 is small relative to the active intensity and contributes much less to the noise field. Kinetic energy density is slightly higher than potential energy density which is suggestive of being in the near field for some frequencies between 300 Hz and 5 kHz. We must be careful in describing this entire range as a near-field measurement because the distance to which the near field extends is frequency dependant. Similar trends in level exist for each metric and the active intensity vectors provide a clear image of how noise is radiating from the plume in the 300 Hz to 5 kHz frequency range.

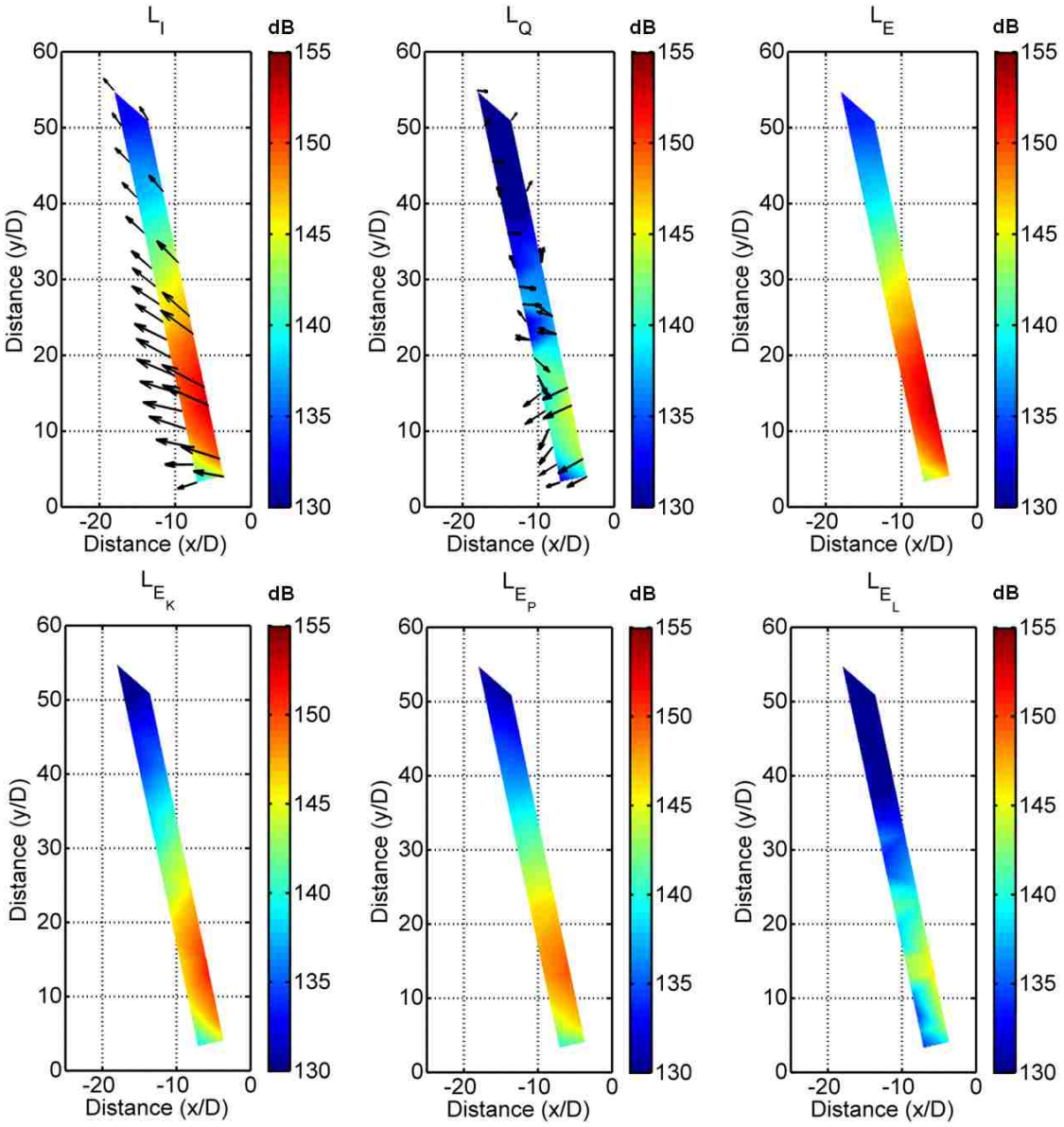

Figure 5.15. Overall sound energy level and intensity for the limited frequency range 300 Hz to 5 kHz.

Eldred[1], in his NASA SP-8072 monograph, states that the peak direction of radiation for a solid rocket motor is between 50°-70° for rocket noise (0° points down the line of fire, $+\hat{y}$, 90° points in the $-\hat{x}$ direction). In the frequency range of maximum intensity, i.e. 400 Hz as discussed in conjunction with Figure 5.9, the directivity agrees with what is predicted in the

monograph. The band-limited total intensity has components pointing from approximately 45° farther downstream to > 90° at the most upstream measurement position.. The peak radiation shown by the intensity vectors is along the 50°-70° direction. As we move upstream, the direction of radiation also turns more upstream and appears to not point downstream at all for one measurement location. This may be due to the rocket noise being refracted upstream in this location. Similar results are seen in Krueger's[7] thesis where he uses both intensity and near-field acoustical holography techniques to find the intensity vectors of an aeroacoustic jet.

5.5.1 Potential and kinetic energy densities

Being able to properly describe the acoustic field and source characteristics of a rocket plume is an ultimate goal in this area of research. Potential and kinetic energy density quantities can help us judge when we are in near or far field for certain types of acoustic sources. This information can be used to help describe the acoustic field and potential source characteristics of this particular rocket motor.

For the 12.7 cm CP test, we see in Figure 5.16 the difference between the potential energy density and kinetic energy density levels ($L_{E_P} - L_{E_K}$) for each sensor at its various downstream locations. As was the case for the active acoustic intensity vectors, the EF1 array results are not considered valid below 1 kHz. The SA array predicts the smallest difference between the quantities and shows that for frequencies less than 200 Hz the kinetic energy dominates. For a spherically spreading source, being close to a source, or measuring low frequencies will place one in the acoustic near-field and kinetic energy is expected to be higher. The other EF sensors also suggest that kinetic energy density is higher than potential energy density at low frequencies.

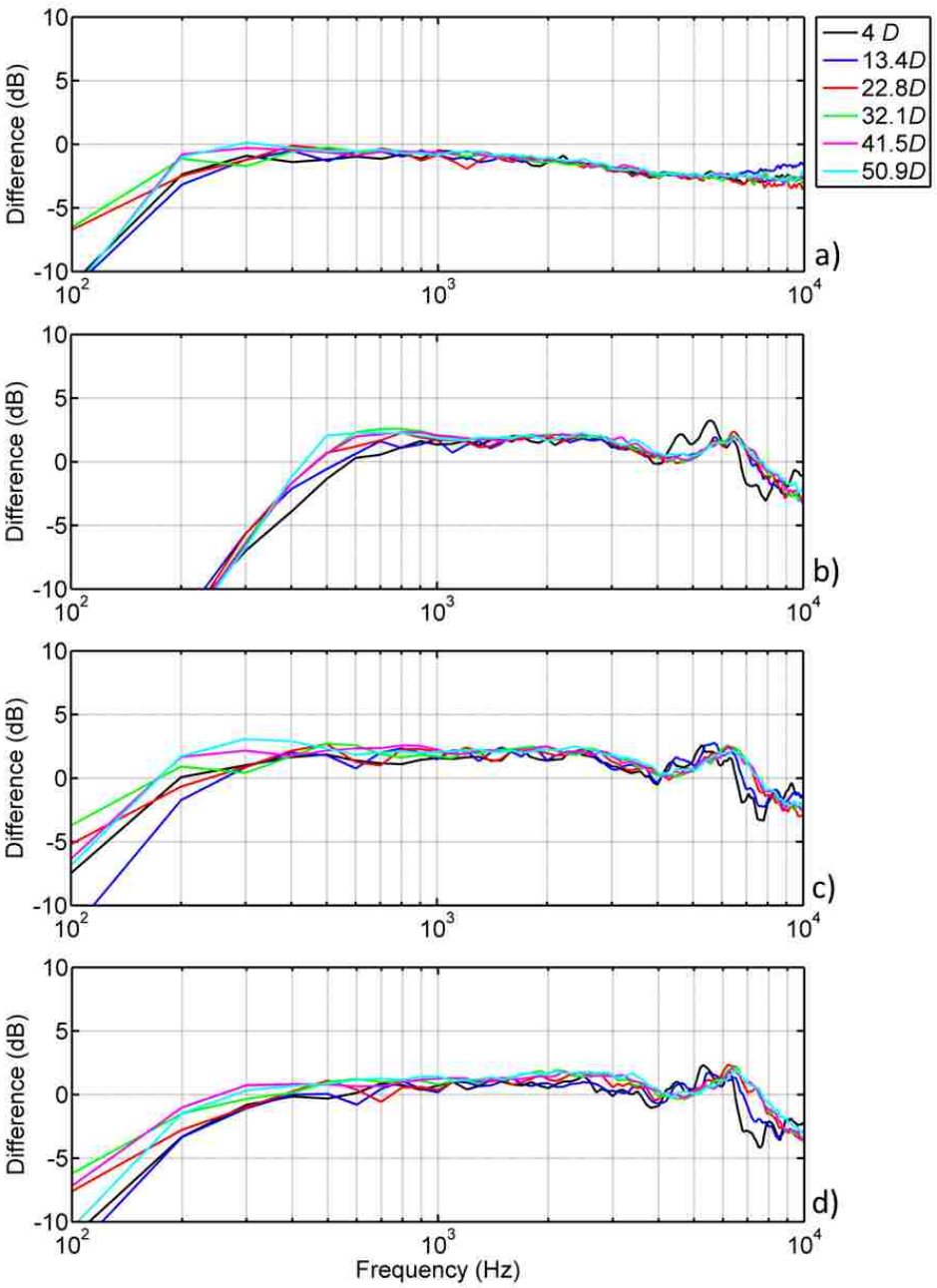

Figure 5.16. The difference between the potential and kinetic energy density levels are given for each of the four arrays in the 12.7 cm CP test: a) SA, b) EF1, c) EF3 and d) EF2. Each line represents a measurement made along the plume at a distance downstream given in the legend. The location given in the legend corresponds to where the SA array was during the measurement

A discrepancy between the two sensor types is that all three of the EF arrays show an approximate +2dB difference between the quantities in Figure 5.16 whereas the sphere shows about -1 dB. This is an unexpected result when compared with Figure 4.6 where laboratory tests showed that both the EF and SA array calculate this difference to be approximately the same over the 500 Hz to 4 kHz range. The cause for this discrepancy is unknown but it seems most readily attributable to uncertainty in the microphone spacing for the EF array. For the EF array to match the SA array and the laboratory experiments of Chapter 4, there would need to be a +20% error in setting the array size. This amount of error is possible considering the EF array was already set quite small using a 2.54 cm diameter; a placement error of 0.2 cm for each microphone may account for the difference. The SA array already includes a 3/2 scaling factor to account for acoustic diffraction around the hard sphere the microphones are mounted in; removal of this scaling factor would increase the difference between the arrays. Regardless of the difference between arrays, it is intriguing that in the case of the SA array, the rocket noise measured in the field matches that of a controlled laboratory experiment.

5.5.2 Acoustic intensity and energy density

The comparison of acoustic intensity and energy density may also be used to learn more about the nature of an acoustic field and/or source. For propagating fields, such as planar and spherical waves in the far field, we expect that the active acoustic intensity will be proportional to the total energy density multiplied by the sound speed of the medium,

$$I = cE. \tag{5.4}$$

Using this relationship, we are able to produce figures similar to those used as we looked at the potential and kinetic energy density relationship by plotting $L_I - L_E$.

In Figure 5.17 we see that the low-frequency range trends differently than the rest of the frequency range shown and there is little difference between the two quantities. The measurement made 4*D* downstream is the closest measurement to the nozzle, which may account for its uniqueness. Being near the source not only increases the probability of measuring more complicated acoustic fields with finer features, but also means being near the structure the rocket is housed in. There may have been standing waves influencing the actual measurement of the rocket motor at this 4*D* location.

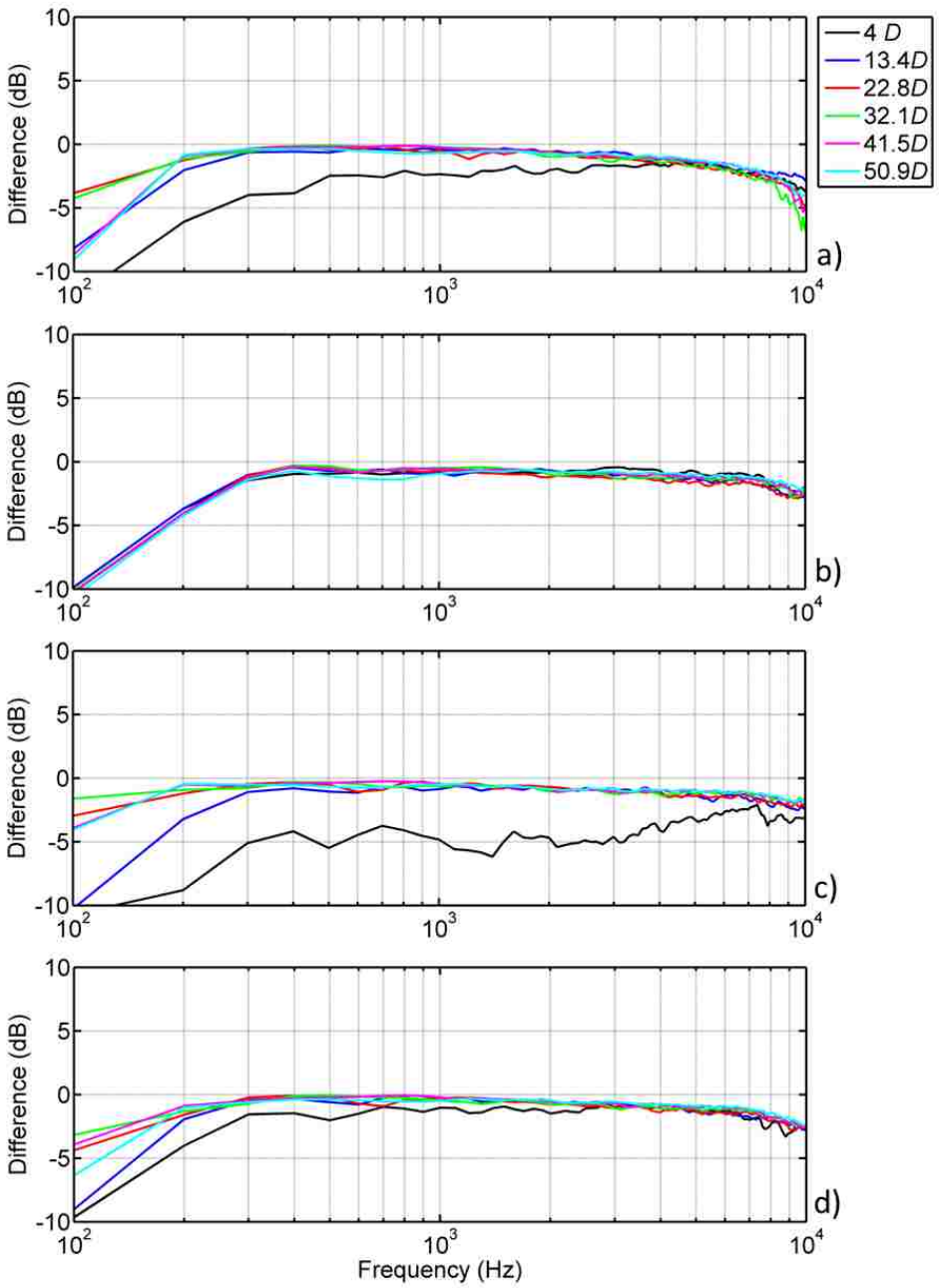

Figure 5.17. The difference of the intensity and energy density levels are given for each of the four arrays in the 12.7 cm CP test: a) SA, b) EF1, c) EF3 and d) EF2. Each line represents a measurement made along the plume at a distance downstream given in the legend. The downstream distances given refer to the location of the SA array.

Intensity and energy density appear to be good approximations of each other with the scaling factor of the sound speed. We are led to believe that there propagating waves in the region of 500 Hz to 3 kHz because the potential and kinetic energy densities are near matches and the relationship in Equation 1.4 appears to hold true. Other evidence is that the Lagrangian energy density is ~10dB less than kinetic or potential energy densities and the reactive intensity is also much lower in level.

5.5.3 Source location

In their work, Jaeger and Allen[6] used an array of sensors parallel to the axis of a small 10.1 cm jet to measure acoustic intensity, and performed ray tracing of the vectors to estimate where the sound had originated. This method helps visualize trends that are more difficult to see with the intensity plots previously shown in this chapter.

From the frequencies shown in Figure 5.18, we see convincingly that the source region moves upstream and contracts as frequency increases. We also notice that for lower frequencies, i.e., 100 Hz to 200 Hz, EF2 does not seem to point in the same direction as its neighbors. It may be that a calibration error was overlooked in the transfer function analysis. Similar to Jaeger and Allen's work, when there is a general convergence of the rays, the rays of Figure 5.18 converge on the opposite side, and outside, the plume. Lower frequencies appear to converge less tightly and farther outside the plume than do the higher frequencies. This is likely indicative that the source(s) is actually spread out or transient in the region spanned by the rays inside the plume. This suggests again that the low frequencies have much larger or more widely distributed noise sources than those sources which produce the higher frequencies.

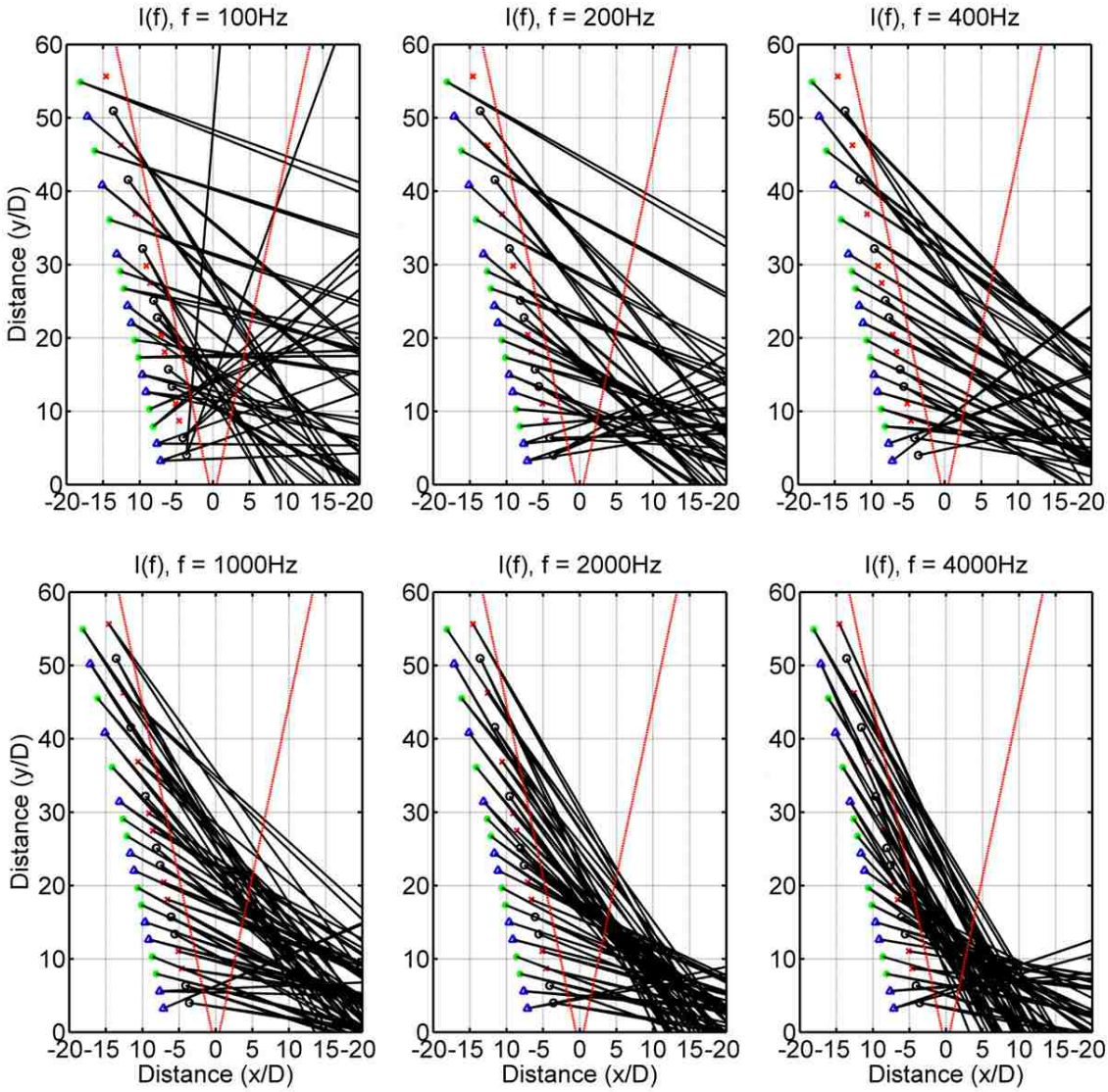

Figure 5.18. Ray tracing of vectors to find source locations of the 12.7 cm CP measurements.

5.6 Conclusion

From these measurements of the 12.7 cm CP data set, acoustic intensity and other energy metrics have been calculated for multiple similar rocket firings in a single test bay. By assuming that the acoustic fields generated are consistent between firings, we have created maps of these metrics along the length of the exhaust plume. Apart from providing an improved understanding

of the acoustic energy quantities near a solid rocket motor, these tests have also provided insight into the limitations of array designs for taking these types of measurements.

We have seen that sources contract and move upstream for noise generated by a rocket plume and that lower frequencies appear to have more distributed sources. The interaction of these sources causes directional radiation of the sound which has been seen to be consistent with measurements presented in the monograph SP-8072[1]. It is hoped that these types of measurements will provide a better understanding of noise generation by rocket motors and serve to improve prediction methods currently in use. Our ability to localize some sources, as in Figure 5.18, suggest that this is possible, at least for some frequencies of rocket motors this size.

The usefulness of plotting transfer function relationships between microphones in an array has also been seen in this analysis. We are able to decide, based on data, over what frequency range a sensor may be used with confidence. For these particular array types, frequencies below 2 kHz are considered to be the most accurate and this is consistent with the laboratory results of Chapter 3 and Chapter 4.

6 Analysis of a large test motor

6.1 Test setup

Another solid rocket motor, the graphite epoxy motor (GEM-60) represents a much larger source, having an exit nozzle of 1.1m diameter and is shown in Figure 6.1. Acoustic arrays nearly identical to those used in the 12.7 cm CP measurements were also placed in similar fashion for two separate motor test firings of a GEM-60 solid rocket motor.

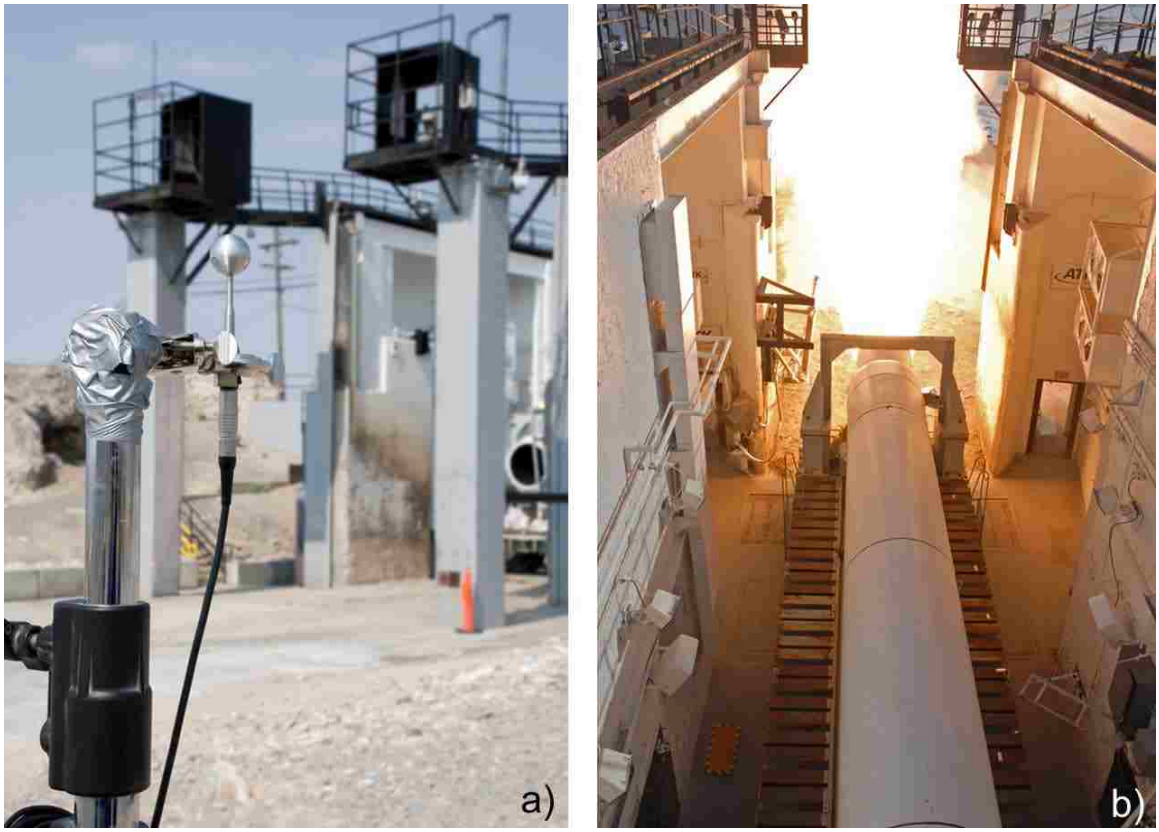

Figure 6.1. Two views of a GEM-60 solid rocket motor a) from the point of view of a SA array downstream (rocket nozzle is in the background) and b) during firing as viewed from above.

The first test occurred on June 26, 2008 and the second occurred on February 19, 2009. For these larger tests, a single recording was obtained for each rocket motor. Unlike the multiple

compact measurements taken with the 12.7 cm motor data and discussed in the previous chapter, the sensors in these tests were spread along the shear layer to cover a larger region for these two single individual measurements. Figure 6.2 shows the scale of the test and the general layout of the microphone arrays and test bay used in each firing.

Figure 6.2. A line of microphone arrays is set parallel to the shear layer of a GEM-60 solid rocket motor in preparation for the February 2009 test firing.

In each test, a line of arrays was set up along the shear layer of the exhaust plume. By examining spalling of the concrete of the test bay, it was determined that the plume had a spread of approximately 16° off of the axis of firing. For the June test, the motor was gimbaled by ± 5° towards and away from our sensors. For this reason, the sensors were set along a 22° radial from the centerline of the motor with an offset of 9.4*D* from the plume edge. The exception was a SA array which had an offset of 6.7*D* from the plume edge. For the February motor firing, the motor

was not gimbaled during firing and the arrays were safely set along a line of 20° off the plume axis with an offset of 8.3*D* from the presumed edge of the plume. There were two types of microphone arrays used during the February test: the 2.54 cm diameter sphere and the 5.08 cm EF array. The number of centimeters corresponds to the diameter of the sphere that circumscribes the centers of each microphone in the array. The June test used the 2.54 cm SA and 5.08 cm EF arrays. A comparison of Figure 6.3 with Figure 5.1 show that when scaled by nozzle diameter of the motor, *D*, the 12.7 cm CP test covers a wider range of distances, approximately 5*D*-55*D* downstream.

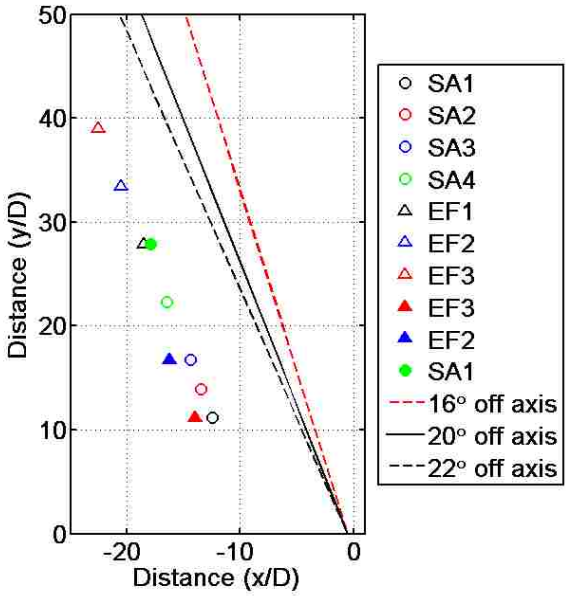

Figure 6.3. Intensity array locations for both GEM 60 static test firings. The plot markers for the June test are filled in solid and the open markers refer to the February test. Assessment of the February 2009 GEM-60 test

6.1.1 Sound pressure level

Sound pressure levels are shown in Figure 6.4 and Figure 6.5 for each microphone array in the Feburary 2009 GEM 60 motor firing. An interesting feature of each of the four SA arrays in Figure 6.4 is that 'Mic 2', see Figure 5.2 for orientation, exhibited a boosted low-frequency response, a response that seems to decrease with distance downstream. This response is due to a capacitive discharge effect of the data acquisition system that occurs when pressure fluctuations (registered as voltage fluctuations through transduction to the acquisition system) are extreme over very short time steps.[35] The primary impact of this effect is that we are unable to trust the results in the frequency range where this effect is noticed. It should be noted that this effect, although not seen in Figure 6.5, has been recorded using the EF array designs as on microphone 3; the microphone which most directly faces the plume. It is possible that there are more of the near-discontinuous shocks that produce this type of error in the region nearest the source; this would explain why they are only noticeable on the SA arrays.

Also common between each of the SA, as well as EF arrays, is a dip in the amplitude around 100 Hz seen in Figure 6.4 and Figure 6.5. These "nulls" correspond to interference between direct and ground-reflected noise from the rocket plume. They do not occur at exactly the same frequency for each array because the relative array and plume geometry is different for each sensor location. As was seen for the measurements of the smaller motor in Chapter 5, scattering errors create differences in the spectra of the microphones that are more noticeable above 2-3 kHz.

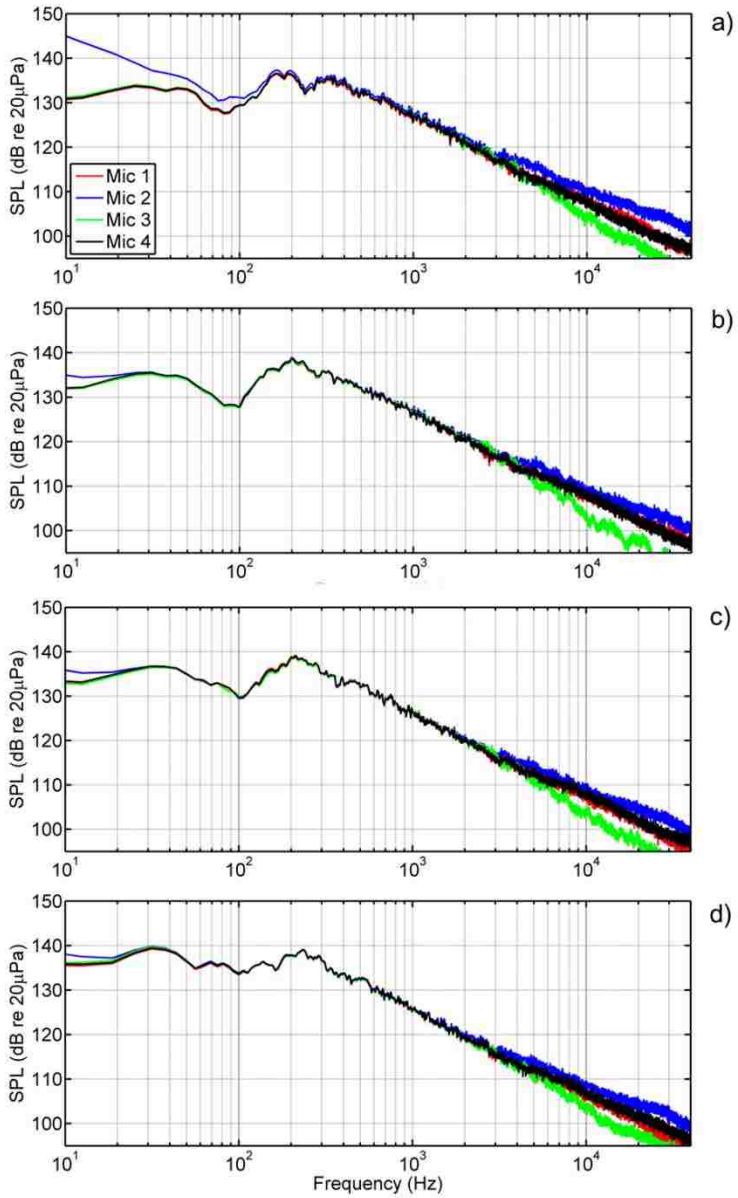

Figure 6.4. Sound pressure levels for the 4 microphones used in each of the 4 SA arrays during the GEM60 test firing in February 2009. The individual plots are for arrays a) 11.1, b) 13.9, c) 16.7, and d) 22.2 *D* downstream.

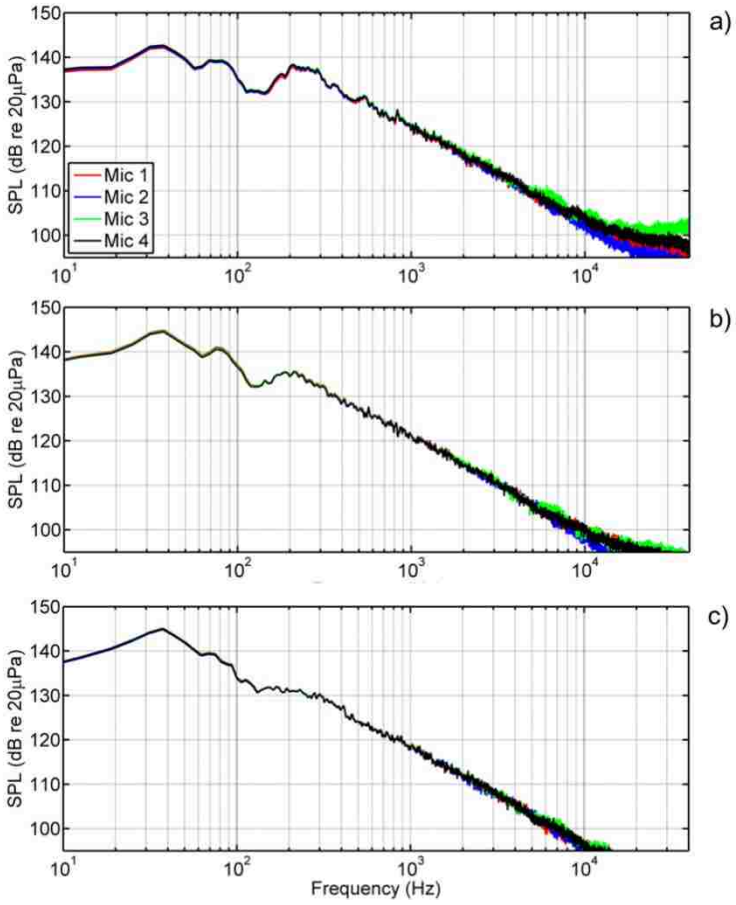

Figure 6.5. Sound pressure level for the a) EF 1, b) EF 2, and c) EF 3 arrays during the GEM60 test firing in February 2009. These measurements are taken at a) 27.8, b) 33.4, and c) 39 *D* downstream.

6.1.2 Transfer function

It is expected that the transfer function responses, shown in Figure 6.6, Figure 6.7, Figure 6.8 and Figure 6.9, have magnitude agreement approaching 1 and phase difference approaching 0° at low frequencies. These transfer functions are determined using in situ data samples and include all field effects present during the actual test. They are calculated by taking the ratio of the single-sided cross and auto correlation spectra. Factors including but not limited to, temperature, electrical contamination, venting and orientation of the microphone array will make the actual

transfer function response of the arrays non-ideal. These irregularities help us determine the effective bandwidth of the array.

In Figure 6.6a, microphone 2 on the SA1 array appears to have a magnitude response error which seems somewhat independent of frequency. This discrepancy is not smoothly varying and is likely not a simple calibration error but may suggest a problem with the signal acquired in the field. There is also some inconstancy at 100 Hz for plot c of Figure 6.6 which is likely attributed to interference patterns in the acoustic field. In Figure 6.7a there is a very slight calibration error with microphone 2 which may need to be adjusted for, depending upon what type of accuracy is deemed acceptable. These transfer function response spectra suggest again that the most reliable range of the arrays to be between approximately 50 Hz and 2 kHz.

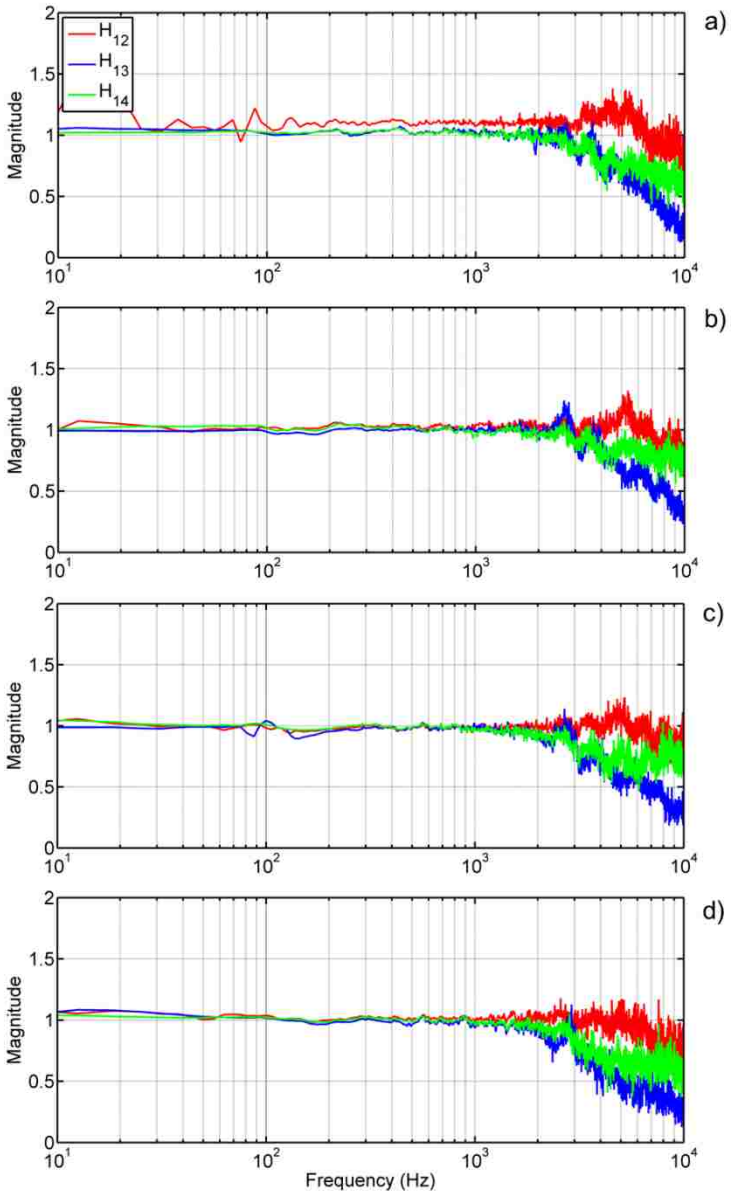

Figure 6.6. Transfer function magnitude for the microphones used in each of the 4 SA arrays during the GEM60 test firing in February 2009. The individual plots are for arrays a) 11.1, b) 13.9, c) 16.7, and d) 22.2 *D* downstream.

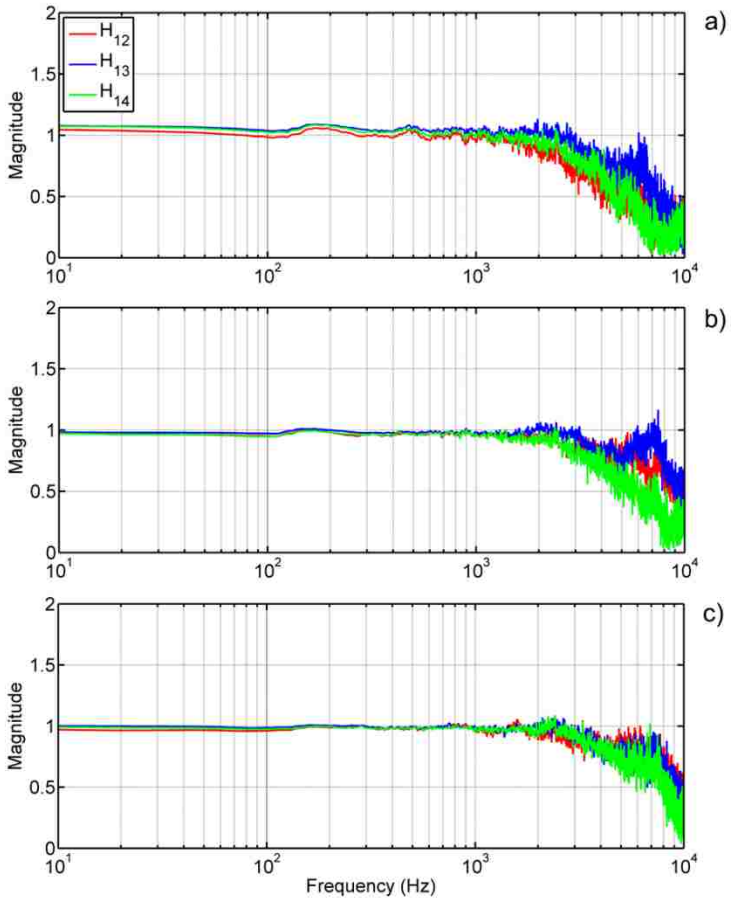

Figure 6.7. Transfer function magnitude for the a) 40BH array, b) Low sensitivity ICP array, and c)High sensitivity array during the GEM60 test firing in February 2009. These measurements are taken at locations a) 27.8, b) 33.4, and c) 39 *D* downstream.

At low frequencies, i.e. below 100 Hz, we expect the phase difference between sensors to be <2°. For a 100 Hz acoustic wave at standard conditions, 2° of phase is analogous to 0.02 m which is approximately the separation distance of our microphones. In Figure 6.8 we see that this is not generally the case for the SA arrays. Chapter 2 discusses the use of a transfer function calibration method to improve the low frequency response of the sensors. However, it may be noted that the irregular/wavy response in Figure 6.8a, is not consistent with typical phase

irregularities between sensors. It may be indicative of a problem with the microphone or preamplifier.

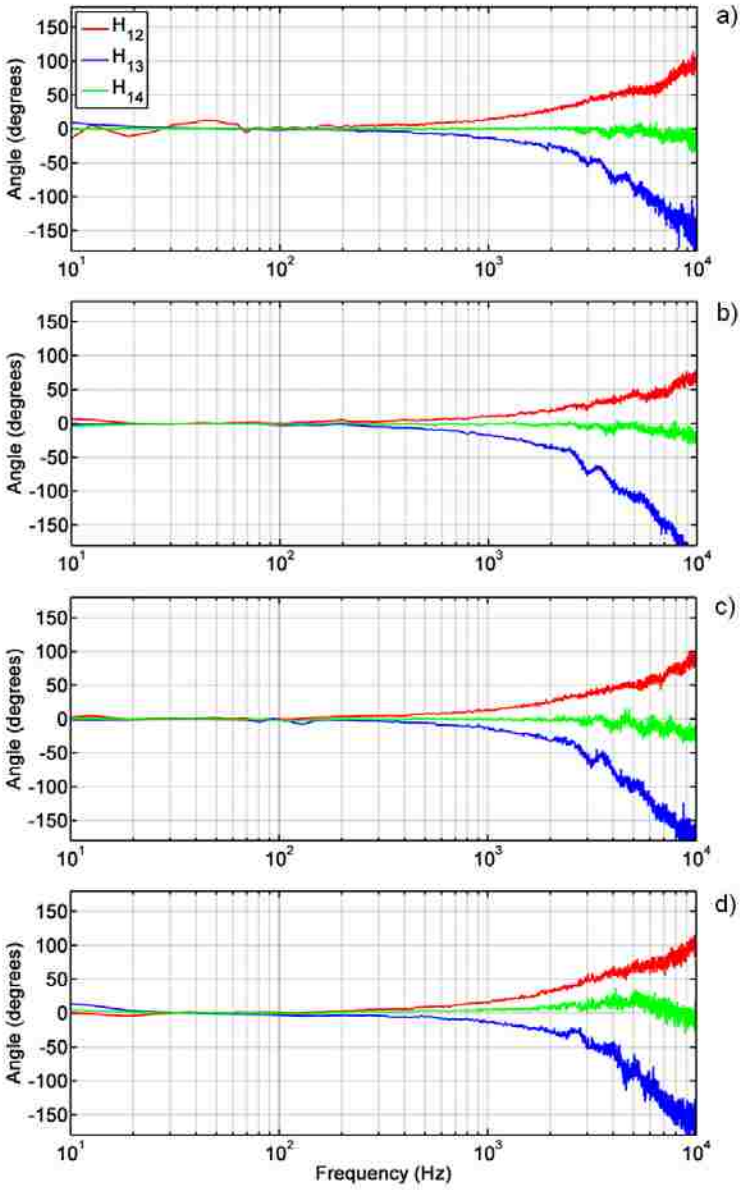

Figure 6.8. Transfer function phase for the microphones used in each of the 4 SA arrays during the GEM60 test firing in February 2009. The individual plots are for arrays a) 11.1, b) 13.9, c) 16.7, and d) 22.2 *D* downstream.

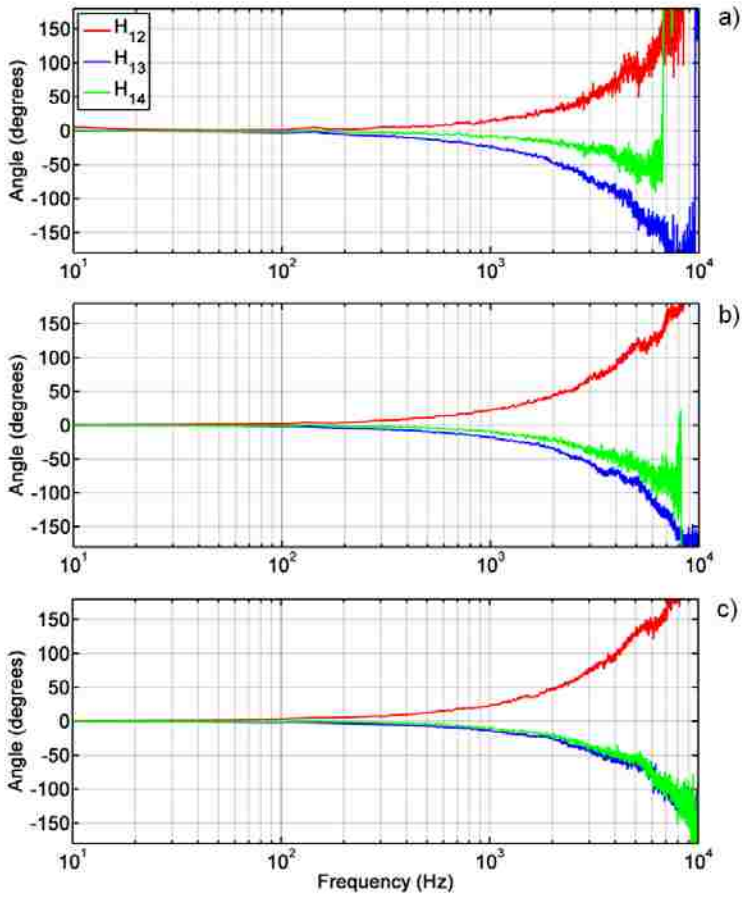

Figure 6.9. Transfer function phase for the a) 40BH array, b) Low sensitivity ICP array, and c)High sensitivity array during the GEM60 test firing in February 2009. These measurements are taken at locations a) 27.8, b) 33.4, and c) 39 *D* downstream.

For the EF arrays, we begin to notice that as the downstream distance increases from a) to b) to c) in Figure 6.9, H_{14} begins to have a phase response more similar to H_{13}. This trend suggests that microphones 3 and 4 begin to measure sound arriving at a similar phase relative to microphone 1, we know from our microphone orientation that the sound is arriving from farther upstream relative to the arrays. This is an expected result as we move downstream beyond the region of peak noise generation.

6.2 Assessment of the June 2008 GEM-60 test

6.2.1 Sound pressure level

The arrays for the GEM60 test in June of 2008 were set somewhat farther from the rocket plume and although both tests used the same data acquisition system, there is no evidence in the sound pressure level spectra of Figure 6.10 to suggest that the low-frequency capacitive roll-up was involved in the February 2009 test. We see clearly in Figure 6.10c that at frequencies above approximately 2 kHz, the SA array is exhibiting amplified levels due to scattering off microphone 2.3.

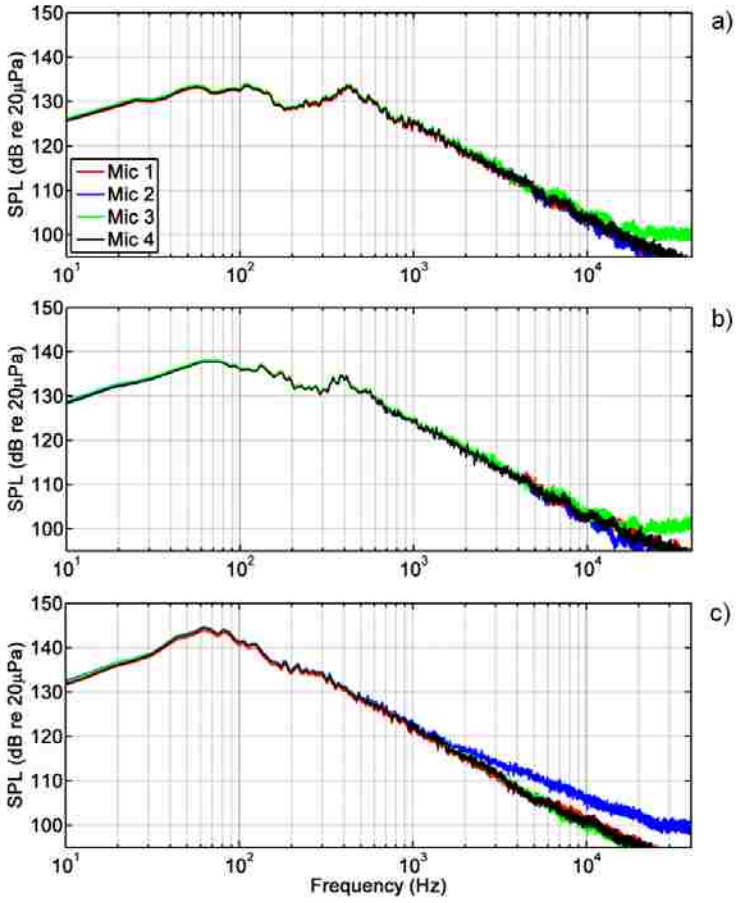

Figure 6.10. Sound pressure level for the a) EF3, b) EF2, and c) SA1 arrays during the GEM60 test firing n June 2008. The individual plots are for arrays a) 11.1, b) 16.7, and c) 27.8*D* downstream.

6.2.2 Transfer function

Similar to plots presented previously, scattering errors in Figure 6.11 are evidenced by the increasing "jitter" in the data above 2 kHz. It is expected that at 10 Hz the magnitude of the transfer function between any of the microphones should be 1. Some of the discrepancy seen in this figure is due to the fact that although the microphone response is "flat", it may be that there is up to 4dB difference between two microphones measuring the same acoustic pressure. Broadband calibration of the microphones as done in Chapter 2 should improve this result.

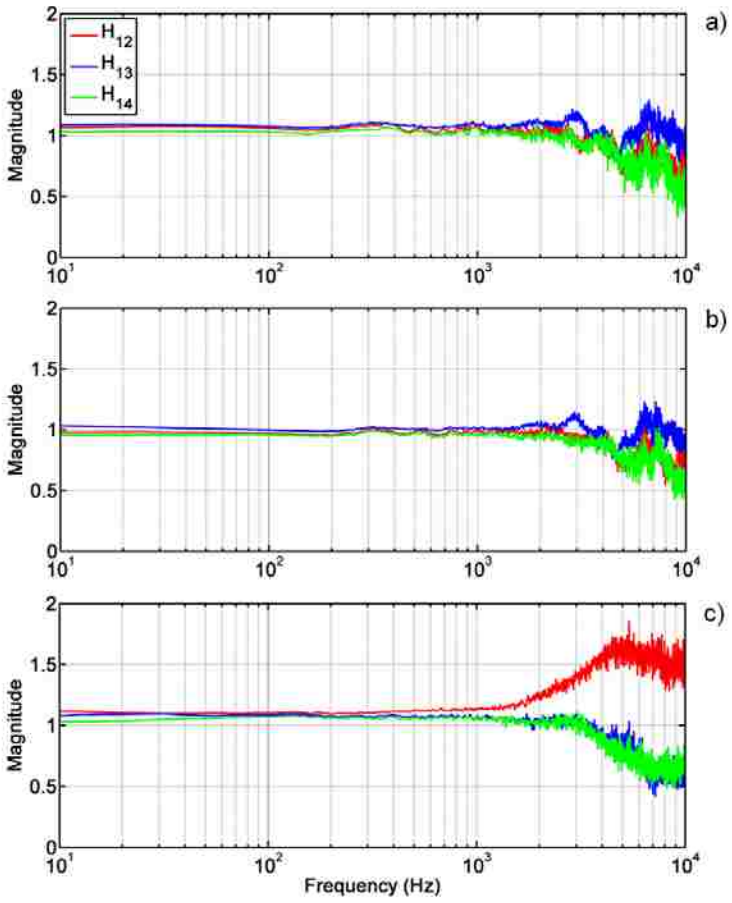

Figure 6.11. Transfer function magnitude for the a) EF3, b) EF2, and c) SA1 arrays during the GEM60 test firing in June 2008. The individual plots are for arrays a) 11.1, b) 16.7, and c) 27.8*D* downstream.

For the transfer function angle plots in Figure 6.12, all make sense and appear valid between 50 Hz and 2 kHz. We notice again that for the SA array (plot c), H_{13} and H_{14} are beginning to measure close to the same value which indicates that we are beyond the source generation region of the rocket motor above 3 kHz. At low frequencies, plot c does not have the expected 0° error, this suggests a phase calibration problem which may also be improved in future tests via a proper broadband calibration.

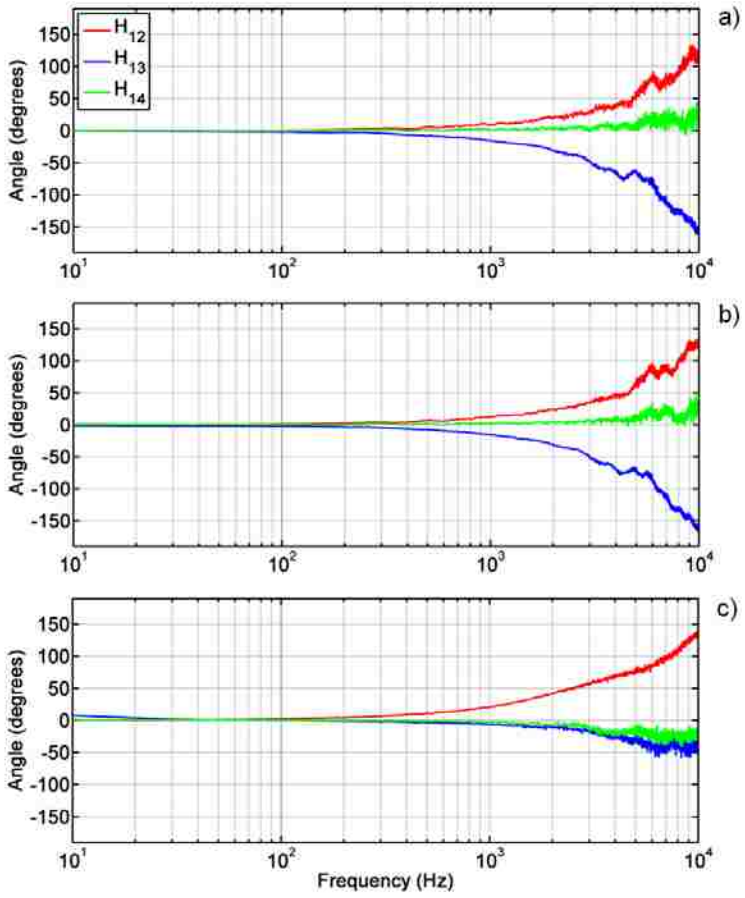

Figure 6.12. Transfer function magnitude for the a) EF3, b) EF2, and c) SA1 arrays during the GEM60 test firing in June 2008. The individual plots are for arrays a) 11.1, b) 16.7, and c) 27.8*D* downstream.

From these sound pressure level and transfer function plots, we are able to learn more about which sets of data are most reliable, as well as more information about the noise field itself. We were able to identify some channels that may produce spurious results due to improper calibration. Also seen was the impact that the capacitive discharge of the data acquisition system had (or did not have) on the transfer function response. We also notice that there was significant scattering affecting the transfer function between microphones in both magnitude and phase. As a result of scattering, the magnitude and phase response between microphones varies largely above a couple of kilohertz and likely limits our ability to calculate energy-based quantities accurately. It is recommended that these types of analysis be used as a part of routine processing of array-based measurements in the future.

6.3 GEM 60 Intensity plots

Similar to the analysis made in Chapter 5, we now consider the active acoustic intensity vectors for both GEM 60 static test firings. These measurements were taken farther (more nozzle diameters) away than any of the 12.7 cm CP measurements and may be more representative of the acoustic far-field. However, the limitation of nozzle diameter as a scaling factor is not well known and may not apply for these particular sources.

As was seen previously, as frequency increases the source region begins to appear to be moving upstream and contracting. We also see that the vectors tend to point in the 50° to 70° direction that is predicted by SP8072. The majority of the energy for this motor is below the kilohertz range and as the vectors shorten, they become less important to the overall intensity magnitude and direction.

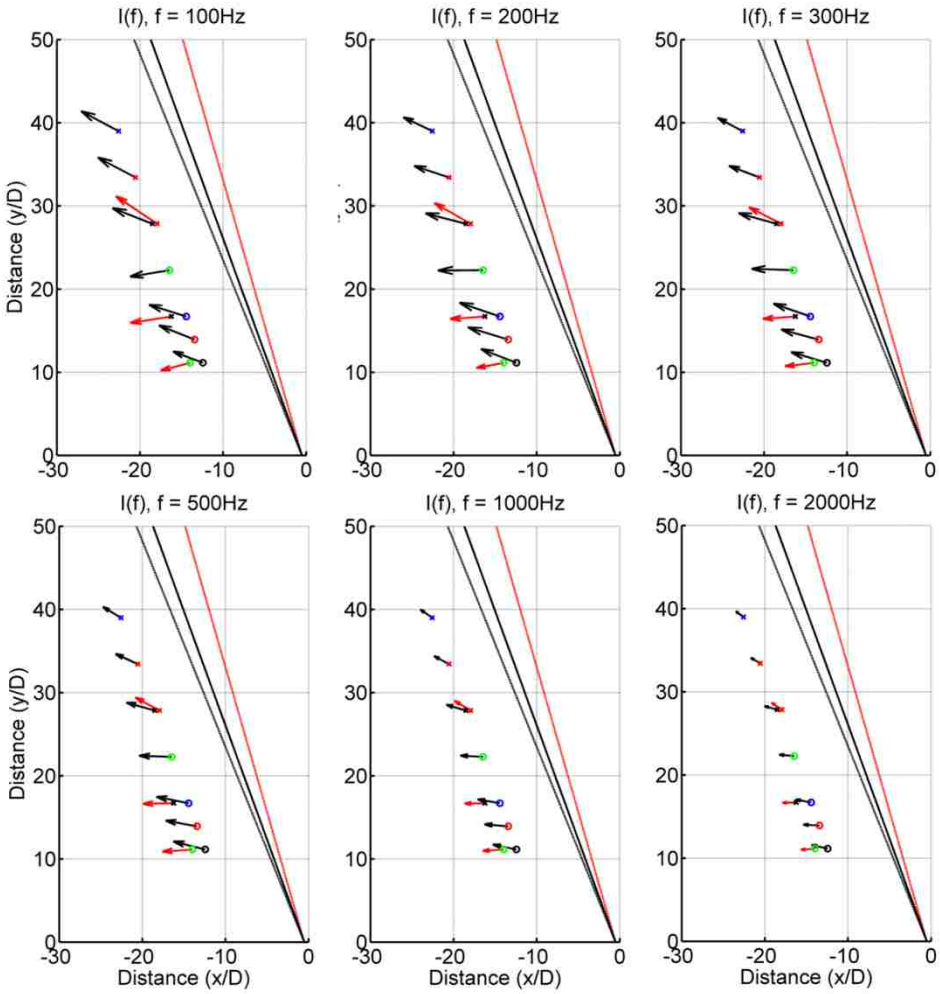

Figure 6.13. Active acoustic intensity vectors for a GEM 60 solid rocket motor static test in February 2009 (black vectors) and June 2008 (red vectors). The black lines are the presumed 20° and 22° angle of the spreading plume; the red line is the 16° where spalling of the concrete was apparent and indicative of a minimum angle of the plume.

The intensity vectors for the June GEM test are somewhat similar to the February test in relative level, but the directions are significantly different; the first two sensors point more upstream and the farther sensor points in a direction more consistent with the SA arrays of the February test. It may be that the gimbaling, or swinging, of the plume back and forth caused the closer sensors to point more upstream during the June test. This gimbaling may also account for

the difference in level. The June test shows lower levels at all locations, even at the ~28*D* downstream position where sensors were placed in nearly the same location. Some environmental factors may also play into the differences between firings. The temperature difference between the tests is significant, with the February test being ~50°F cooler. Also, in the region where these sensors are placed, there is a sloping hill that is snow-covered in February and rocky in June, which will modify the acoustic environment. A portion of that hillside had also been carved out between tests.

Another possibility for the variation directional variation between tests could be the difficultly of orienting the arrays, particularly the 2.54 cm diameter SA arrays, relative to the shear layer in the field. At the third-to-last microphone position downstream in Figure 6.13, we see that the EF1 array from the February 2009 test and the SA1 Array from the June 2008 appear to be off by a nearly constant angle from one another independent of frequency. It is uncertain if this offset is related to orientation of the microphones in the field (most likely), the structure of the acoustic field itself or some other phenomenon. Similar discrepancy exists between tests at the first and third most upstream location; the SA arrays suggest a source located farther upstream than the EF arrays. This is but one more uncertainty which exists for these types of measurements. Future measurements may benefit from the use of a laser alignment system or similar device to align the arrays with more confidence.

6.4 A comparative analysis

6.4.1 Potential and kinetic energy densities

For the small motor test in Chapter 5, we saw the difference between the potential energy density and kinetic energy density levels for each sensor at its various downstream locations. In both Figure 6.14 and Figure 6.15, we see multiple sensors (multiple locations) showing the

difference between the kinetic and potential energy density levels. Here we find that the kinetic energy dominates at low frequencies and for 200 Hz to 1.5 kHz we have nearly zero dB difference between quantities suggesting perhaps a nearly planar or spherical acoustic field. The surplus of kinetic energy at low frequencies appears to be less as we move downstream for the February test. The arrays in the legends in these figures are listed in order near-to-far from the source, top to bottom, i.e. SA1 is nearer the rocket motor than EF3 in Figure 6.14. The June test shows no such pattern in the low frequencies. The relative increase in low-frequency kinetic energy density seems to suggest that we are in the near-field of the source as we move farther upstream. This agrees with the result that farther downstream, the potential and kinetic energy are more equal. It is unexpected that the upstream location, which is approximately 3 wavelengths away at 100 Hz, would show this characteristic of an acoustic near field. Perhaps nonlinear propagation of the noise increases the apparent size of the near-field, or other field effects that are not well understood cause this phenomenon.

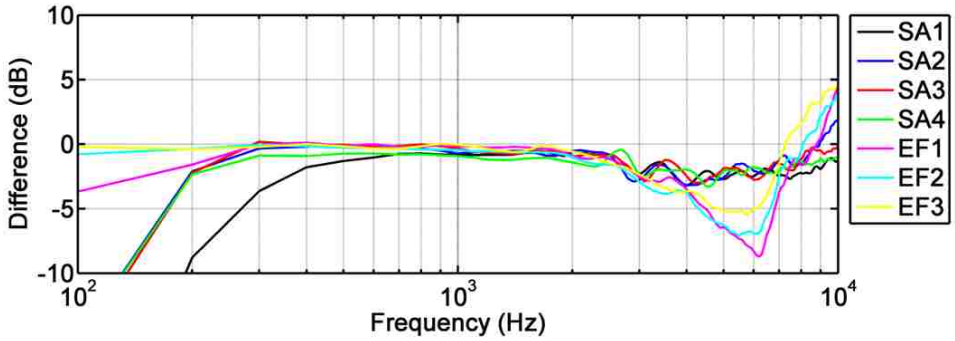

Figure 6.14. The difference of the potential and kinetic energy density levels are given for each array during the February GEM test.

The relationship of these quantities is again interesting in that the results are not consistent. In Chapter 5 we saw that the EF array calculated the potential energy density to be higher than

the kinetic energy density over mid-range frequencies. In Figure 6.14 for the February test, we see that the EF and SA arrays agree and then again in Figure 6.15 the arrays do not agree for the June test. It was suggested in Chapter 5 that perhaps slight errors in setting the size of the EF arrays account for this difference. The diameter of the EF array was 2.54 cm, 3.81 cm and 5.08 cm for the CP, June GEM, and February GEM tests (respectively). Notice that the amount by which the EF array overestimates this difference decreases proportional to array diameter (the largest discrepancy was for the CP test and the least discrepancy was for the February GEM test). If there was a consistent user error in assembling the arrays it may be less significant for larger diameters. This slight difference in array spacing would be expected to be more noticeable in the calculation of the kinetic energy density because it is calculated to be proportional to the square of the radius, as opposed to intensity whose magnitude is inversely proportional to the radius alone. Using the relationship of kinetic and potential energy densities as a verification of array diameter may be of interest for future research.

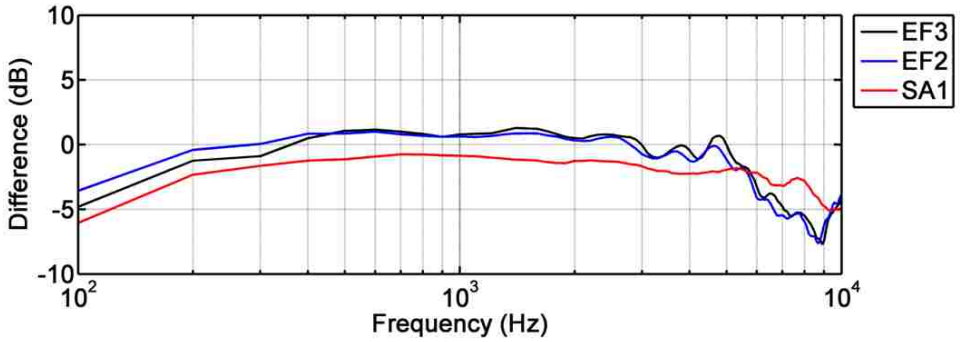

Figure 6.15. The difference of the potential and kinetic energy density levels are given for each array during the June GEM test.

6.4.2 Acoustic intensity and energy density

As we plot the difference between acoustic intensity and energy density in Figure 6.15 and Figure 6.16, we see similar trends as were found comparing kinetic and potential energy densities, with intensity dominating near the source and at low frequency for the February test.

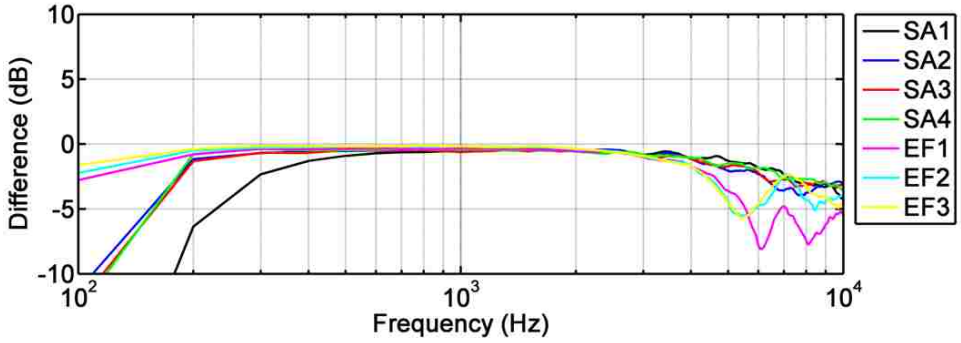

Figure 6.16. The difference of the intensity and energy density levels are given for each array during the February GEM test.

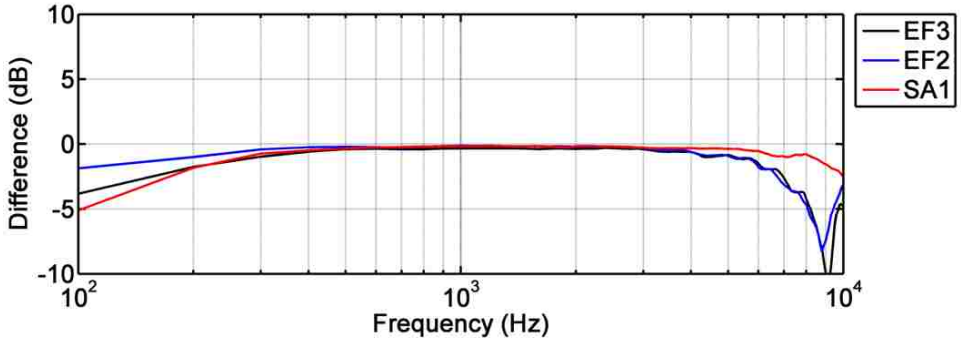

Figure 6.17. The difference of the intensity and energy density levels are given for each array during the June GEM test.

The results for the GEM test compare much better with the 12.7 cm CP measurements of Chapter 5 on this metric than they did with the kinetic and potential energy densities. Because the intensity and energy density appear to be good approximations of each other with the scaling factor of sound speed, we are led to believe that there are planar or "locally planar" spherical

waves in the region of 500 Hz to 3 kHz. This correlates with what we saw with the kinetic and potential energy density figures as well. It may be that below 500 Hz, these sensors are in the geometric near-field of the noise-generating structures inside the plume.

In the particular case of the February GEM test (Figure 6.16), we find that moving downstream is measured as being more planar or far-field, (using the arguments of this section) and the high frequencies become less planar with downstream distance. This may indicate that farther downstream there are larger structures generating the low-frequency noise and they appear more locally planar due to their size. We know the low frequencies are generated farther downstream. Therefore, disregarding directivity of sources, we would expect the arrays nearest the nozzle (most upstream) to also have very planar low-frequency wavefronts. This idea of large low-frequency structures is consistent with the model of jet noise presented by Tam et al.[36] which talks of fine-scale turbulence and large turbulent structures being responsible for high and low-frequency noise generation, respectively.

6.4.3 Source location

Using the ray tracing method of Chapter 5, we are able to attempt to determine source locations for this much larger rocket motor in Figure 6.18. The results of the two GEM tests are not quite so dramatic, yet the same trends are present. The source region moves upstream (slightly) with increasing frequency and becomes more compact. The change does not happen as readily either. All the frequencies shown seem to have preferred radiation in essentially the same direction. This may be related to having a highly extended source region in the plume.

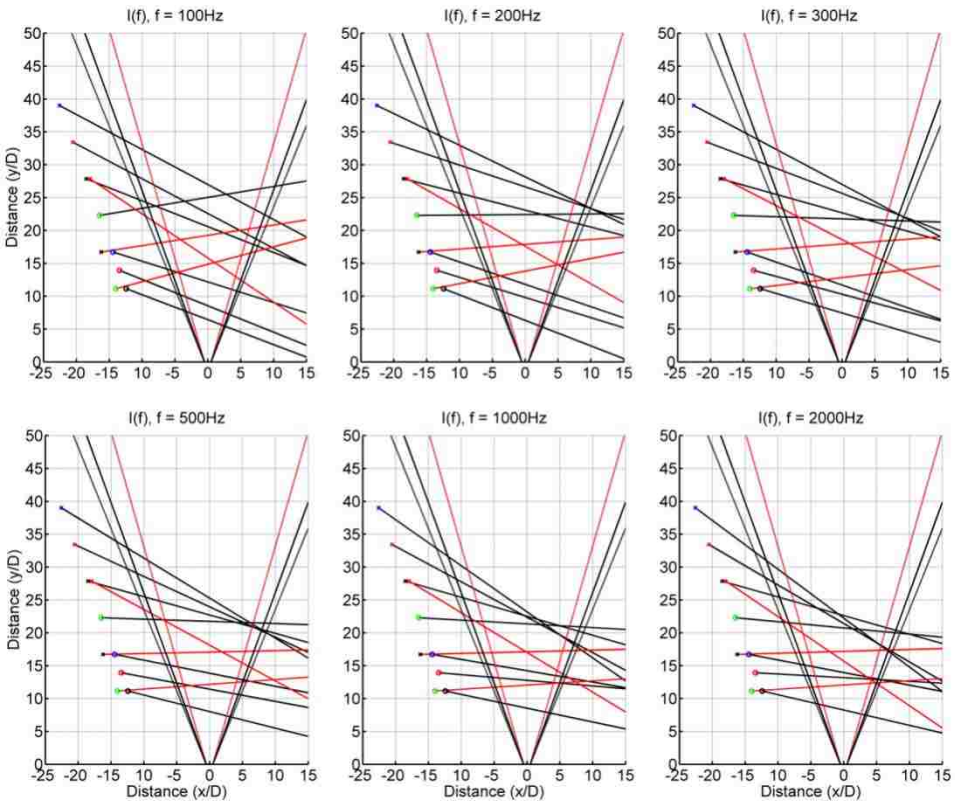

Figure 6.18. Ray tracing of vectors to find source locations of the February (black) and June (red) GEM measurements. As in previous figures, the rays stemming from the origin correspond to angular plume widths of 16°, 20° and 22° measured from the y-axis.

If we focus on only the June test, it is difficult to say if the direction of the microphone array farthest downstream is correct. It appears to be out of line with the only other two sensors, yet agrees well with the two farther downstream measurements of the February GEM test. For the February test at the sphere 4 array position, we see agreement with the two June test arrays most upstream. This microphone position is approaching the location of peak intensity and that may account for its tendency to point more downstream than the other vectors.

Jaeger and Allen's work seems to agree best with the measurements of the 12.7 cm CP data set with assumed source locations and general trends. It is unclear whether it is because Jaeger's

0.1016 m nozzle is similar in size, the CP plume had a more similar mach number, or because the size of the data sets were similar and gave a better resolution map. It may be an important consideration that using smaller scale rockets to predict what will happen acoustically for larger ones, such as the GEM 60, may be inappropriate. In general, the conditions between large and small rocket motor tests are vastly different in duration, intensity, nonlinearity and other field and source characteristics. Without extensive knowledge of all the scalable differences, it is best not to equate the two.

6.5 Conclusion

The conclusions here are essentially the same as that for Chapter 5. However, the analysis of the GEM-60 has also shown that it is more difficult to pinpoint the source regions using only a few, well-spaced arrays near a large rocket. Future work in this area might include finding the optimal location for the sensors to capture the defining characteristics of the rocket as economically as possible.

7 Conclusions

7.1 Overview of results

This thesis has been concerned with improving our ability to measure and understand energy metrics in a rocket noise environment. We have approached this task through field measurements and analysis in Chapter 5 and Chapter 6 and have created maps of these metrics along the length of the exhaust plume. We have seen that sources contract and move upstream for noise generated by a rocket plume and that lower frequencies appear to have more distributed sources. The analysis of the GEM-60 has also shown that it is more difficult to pinpoint the source regions using only a few, well-spaced arrays near a large rocket. For all three rocket tests, we saw that the peak direction of acoustic radiation is between 50° and 70° as was expected from the literature. Apart from providing us with an improved understanding of the acoustic energy quantities near a solid rocket motor, these tests have also provided us with insight into the limitations of the array designs for taking these types of measurements.

Chapter 3 and Chapter 4 were focused on comparing theoretical limitations of the arrays in an ideal plane wave environment with simulated plane wave experiments in an anechoic chamber. For these controlled measurements it was shown that the magnitude of the active acoustic intensity may be theoretically determined within 2-3 dB accuracy between 500 Hz and 10 kHz for the rotation about $\theta = 0$. The error in estimating the direction of the active intensity vector has been shown to be theoretically calculable to varying precision (based on frequency) and a second orientation of the arrays was chosen in an attempt to highlight/explore the omnidirectionality of the sensors and illustrated how orientation and frequency of interest impact the performance of the array.

For the two designs presented, the 2.54 cm PA array consistently out-performs the 2.54 cm SA array in un-calibrated measurement of the active acoustic intensity vector magnitude and direction with the exception of the low-frequency end of the acoustic intensity vector where the PA design actually over-estimates the intensity by approximately 0.5 dB. Chapter 4 focused on qualifying our plane wave experiment as well as looking for the regions where the energy metrics were no longer valid.

It is recommended that care be exercised when discussing the interpretation of the energy-based metrics of Chapter 3 and Chapter 4 or with future measurements using these sensors. On average we find that the SA array performs best in the region 500 Hz to 5 kHz and the EF is (at best) 333 Hz to 3.33 kHz for measurement of active intensity. Total energy density appears valid over this same region, perhaps more. Kinetic and potential energy densities show more discrepancies than are expected for a plane wave field and appear to have an accuracy of ~±3dB over the 500 Hz to 5 kHz region. The cause of error in the components of energy density is not well understood for these particular designs and perhaps serve best as qualitative assessments of a noise field. From Figure 3.4 we see that a high-frequency cutoff of around 2 kHz would limit errors due to scattering which may be better or worse depending upon angle of incidence of the wave. Assuming this analysis translates to the high-amplitude, shock-laden, rocket noise environment of Chapter 5 and Chapter 6, the results are most reliable in the region below 2 kHz but may be shown with reasonable reliability up to 5 kHz based on these laboratory measurements.

The use of the switching technique to calibrate microphones in an array has also been experimentally shown to be effective at low frequencies and is discussed in some detail in Chapter 4.

7.2 Overview of recommendations

An essential part of these array measurements is verifying that the sensors in the array are properly matched for both phase and magnitude. Calibrations may be performed as discussed in Chapter 2 but should still be verified by means of transfer function analysis as done in Chapter 5 and Chapter 6 before trying to interpret the metrics measured. It is also recommended that phase and magnitude calibrations become a regular part of testing; not only does it improve the low-frequency response/reliability, it keeps track of the sensors should they fall into error as was the case with the EF1 array of the 12.7 cm CP test. Also, as array designs are built, they should be qualified through anechoic chamber testing; this will allow for development of a magnitude calibration array and account for some of the inherent high-frequency error

Chapter 3 and Chapter 4 looked at the high-frequency response of SA, EF and PA arrays. Based on that analysis, it was recommended that for two equal-size SA and PA type arrays, the PA array should be pursued for future development if frequencies greater than 4 kHz are of interest. The ease of calibration for the PA type array is also desirable. The limited scattering of the PA array is what gives it naturally lower measurement error for a similarly sized SA array; however, what qualifies as a "similarly sized" SA array is still debatable.

As more of these types of energy-based measurements of rocket fields are taken, we should be able to see correlations between data sets that will direct future research efforts. In particular, the correct interpretation of the time-averaged reactive intensity vector is still not understood. A more extended map, using all similar microphone arrays may give more physical insight into the field. Our understanding of the active intensity vector may also be enhanced by combining near and far-field measurements to describe the field.

References

[1] K. Eldred, in *Acoustic Loads Generated by the Propulsion System, NASA SP-8072* (1971).

[2] J. Haynes and R. Kenny, "Modifications to the nasa sp-8072 distributed source method ii for ares i lift-off environment predictions," Proceedings of 15th AIAA/CEAS Aeroacoustics Conference, Miami, Florida, 2009, pp.

[3] K. Fukuda, S. Tsutsumi, K. Fujii, K. Ui, T. Ishii, H. Oinuma, J. Kazawa and K. Minesugi, "Acoustic measurement and prediction of solid rockets in static firing tests," Proceedings of 15th AIAA/CEAS Aeroacoustics Conference, Miami, Florida, 2009, pp.

[4] C. Yu, Z. Zhou and M. Zhuang, "An acoustic intensity-based method for reconstruction of radiated fields," J. Acoust. Soc. Am **123**, 1892-1901 (2008).

[5] S. R. Venkatesh, D. R. Poak and S. Narayanan, "Beamforming algorithm for distributed source localization and its application to jet noise," AIAAJ **41**, 1238-1246 (2003).

[6] S. M. Jaeger and C. S. Allen, "Two-dimensional sound intensity analysis of jet noise," AIAA Paper **93-4342**, (1993).

[7] D. W. Krueger, *Array-based characterization of military jet aircraft noise*, Brigham Young University 2012).

[8] C. Wiederhold, *Design and implementation of multi-microphone probes*, Brigam Young University 2011).

[9] J. Y. Chung and D. A. Blaser, "Transfer function method of measuring in-duct acoustic properties. I. Theory," J. Acoust. Soc. Am **68**, 907-913 (1980).

[10] G. Pavic, "Measurement of sound intensity," J. Sound Vib. **51**, 533-545 (1977).

[11] F. Fahy, "Measurmet of acoustic intensity using the cross-spectral density of two microphone signals," J. Acoust. Soc. Am **62**, (1977).

[12] ANSI, "Instruments for the measurement of sound intensity, s1.9-1996," (1996).

[13] *Sound intensity* (Brüel and Kjær, Denmark, 1993).

[14] *Microphone handbook* (Brüel & Kjær, 1996).

[15] (G.R.A.S., http://www.grasinfo.dk/documents/pd_40BI_ver_07_09_05.PDF), Vol. 2012.

[16] S. Gade, *Sound intensity (theory)* (Brüel & Kjaer, 1982).

[17] J. Y. Chung and D. A. Blaser, "Transfer function method of measuring acoustic intensity in a duct system with flow," J. Acoust. Soc. Am **68**, 1570-1577 (1980).

[18] K. H. Miah and E. L. Hixon, "Design and performance evaluation of a broadband three dimensional acoustic intensity measuring system," J. Acoust. Soc. Am **127**, 2338-2346 (2010`).

[19] J. Y. Chung, "Cross-spectral method of measuring acoustic intensity without error caused by instrument phase mismatch," J. Acoust. Soc. Am **64**, 1613-1616 (1978).

[20] G. Krishnappa, "Cross-spectral method of measuring acoustic intensity by correcting phase and gain mismatch errors by microphone calibration," J. Acoust. Soc. Am **69**, 307-310 (1981).

[21] P. Kitech and J. Tichy, "Intensity probe obstacle effects and error of the transfer function technique to calibrate acoustic intensity measurements," Proceedings of Inter-noise 82, 1982, pp. 695-698.

[22] J. Park, M. Garces and B. Thigpen, "The rotary subwoofer: A controllable infrasound source," J. Acoust. Soc. Am **125**, 2006-2012 (2009).

[23] J. K. Thompson and D. R. Tree, "Finite difference approximation errors in acoustic intensity measurements," J. Sound Vib. **75**, 229-238 (1981).

[24] J.-C. Pascal and J.-F. Li, "A systematic method to obtain 3d finite-difference formulations for acoustic intensity and other energy quantities," J. Sound Vib. **310**, 1093-1111 (2008).

[25] B. S. Cazzolato and C. H. Hansen, "Errors in the measurement of acoustic energy density in one-dimensional sound fields," J. Sound Vib. **236**, 801-831 (2000).

[26] H. Suzuki, S. Oguro, M. Anzai and T. Ono, "Performance evaluation of a three dimensional intensity probe," J. Acoust. Soc. Japan **16**, 233-238 (1995).

[27] G. W. Elko, "An acoustic vector-field probe with calculable obstacle bias," Proceedings of National Conference on Noise Control Engineering, 1991, pp. 525-532.

[28] J. W. Parkins, S. D. Sommerfeldt and J. Tichy, "Error analysis of a practical energy density sensor," J. Acoust. Soc. Am **108**, 211-222 (2000).

[29] J. A. Mann and J. Tichy, "Acoustic intensity analysis: Distinguishing energy propagation and wave-front propagation," J. Acoust. Soc. Am **90**, 20-25 (1991).

[30] K. L. Gee, J. H. Giraud, J. D. Blotter and S. D. Sommerfeldt, "Near-field vector intensity measurements of a small solid rocket motor," J. Acoust. Soc. Am **128**, EL69-EL74 (2010).

[31] M. R. Shepherd, K. L. Gee and M. S. Wochner, "Short-range shock formation and coalescence in numerical simulation of broadband noise propagation," J. Acoust. Soc. Am **126**, 2886-2893 (2009).

[32] D. C. Thomas, *Theory and estimation of acoustic intensity and energy density*, Brigham Young University 2008).

[33] J. A. Mann, J. Tichy and A. J. Romano, "Instantaneous and time-averaged energy transfer in acoustic fields," J. Acoust. Soc. Am **82**, 17-30 (1987).

[34] J. A. Mann and J. Tichy, "Near-field identification of vibration sources, resonant cavities, and diffraction using acoustic intensity measurements," J. Acoust. Soc. Am **90**, 720-729 (1991).

[35] T. Taylor, *Microphone system response in high amplitude noise environments*, Brigham Young University 2011).

[36] K. W. Tam, K. Viswanathan, K. K. Ahuja and J. Panda, "The sources of jet noise: Experimental evidence," J. Fluid Mech. **615**, 253-292 (2008).

Appendix A: Energy-based measurements

Multiple microphones in an array may be used to measure many useful acoustic quantities apart from pressure. Herein is given a derivation of the calculations for acoustic quantities: active intensity, reactive intensity, kinetic energy density, potential energy density, total energy density and Lagrangian energy density for four microphones set with their diaphragm centers at the vertices of a regular tetrahedron. Each of these acoustic metrics is estimated for the acoustic/geometric center of the regular tetrahedron. In order to better acquaint the reader with the methodologies and fundamental concepts of this procedure, acoustic intensity is first defined for the simple one-dimensional case.

A.1 Frequency-domain analysis

This section follows the evolution of the time series output of a calibrated microphone (having units in Pa) to the weighted Fast Fourier Transform (FFT) which will be used to obtain the desired metrics.

For a measured pressure x, the sampling frequency fs, number of samples ns, and frequency resolution is df. Also, let the equivalent noise bandwidth, w (not to be confused with angular frequency, ω) account for the effect of windowing the data. The frequency domain pressure used for each channel in this analysis is then

$$\boldsymbol{P}(\omega) = \sqrt{\frac{2df}{ns\ fs\ w}}\, FFT\big(x(t)\big). \tag{A.1}$$

The scaling factor of $\sqrt{2}$ properly weights $\boldsymbol{P}(\omega)$ so that when an auto/cross spectrum is calculated a factor of 2 results and describes only the positive (single sided) frequencies. Using

this scaling factor, the analysis in this appendix is only valid for single sided FFTs. Also, the auto, cross and power spectral *densities* may be determined by not including the $\sqrt{df}$ factor in the scaling.

To simplify expressions, the auto (a=b) and cross spectral (a≠b) terms are utilized, they are defined here as

$$\boldsymbol{G}_{ab}(\omega) = \boldsymbol{P}_a^*(\omega)\boldsymbol{P}_b(\omega), \tag{A.2}$$

where the superscripted '*' denotes the complex conjugate of the signal and ω is the angular frequency dependence. For the remainder of this appendix, it is implied that all equations are functions of frequency and the ω term is dropped. Also important to note is that this analysis assumes a zero-mean process and implies that

$$\boldsymbol{G}(0) = 0. \tag{A.3}$$

The process of taking the analysis to the frequency domain is inherently time-averaged and the following relationships also apply for the cross spectra

$$\begin{gathered}\boldsymbol{S}_{ab} = \boldsymbol{p}_a^*\boldsymbol{p}_b = \frac{1}{2}\boldsymbol{P}_a^*\boldsymbol{P}_b \\ \boldsymbol{G}_{ab} = 2\boldsymbol{S}_{ab}\,, \omega > 0,\end{gathered} \tag{A.4}$$

where S_{ab} and G_{ab} represent double sided and single sided cross spectra, respectively. We will also refer to the real and imaginary parts of the auto/cross spectrum as the "cospectrum", C, and "quadspectrum", Q, respectively and have the following properties.

$$\boldsymbol{G}_{ab}(\omega) = C_{ab}(\omega) + jQ_{ab}(\omega)$$

$$C_{ab} = C_{ba}$$

$$Q_{ab} = -Q_{ba} \tag{A.5}$$

$$Im(j * \boldsymbol{G}_{ab}) = C_{ab}$$

$$Re(j * \boldsymbol{G}_{ab}) = -Q_{ab}$$

A.2 1-D Active acoustic intensity ($\hat{I}$)

An estimation of the acoustic intensity at a point in space may be performed by means of the p-p method[1,2] which employs the use of a finite-difference approximation of the pressure gradient between two microphones. The simplest example is a one-dimensional case using two microphones.

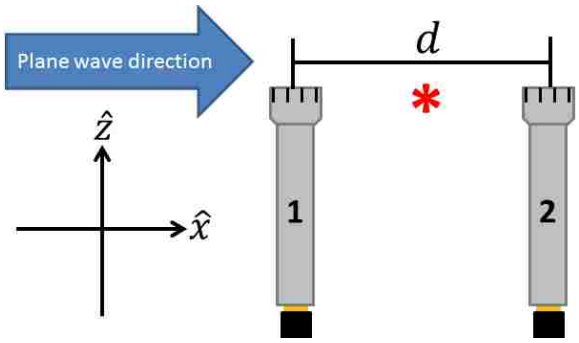

Figure A.1. One possible configuration for the p-p method for measuring acoustic intensity. Often times, the microphones are rotated to face each other and are separated by a spacer. The mathematical derivation of either orientation is the same.

Assume a time-harmonic plane wave propagates in the $+\hat{\boldsymbol{x}}$ -direction. Two microphones are located along this same dimension at $x = \frac{d}{2}$ and $x = -\frac{d}{2}$ such that the acoustic and geometric center of the two microphones is at $x = 0$ and the separation between the two microphones is a distance d. We may then approximate the acoustic intensity at the point $x = 0$ in the following manner:

Active acoustic intensity may be defined as the real part of the time averaged value of the product of the pressure and the complex conjugate of the particle velocity at a point in space.

$$\boldsymbol{I} = Re[< \boldsymbol{p}\hat{\boldsymbol{u}}^* >] \tag{A.6}$$

Let the complex pressure measured at $x = \frac{d}{2}$ be $\boldsymbol{p}_a$ and $\boldsymbol{p}_b$ at $x = -\frac{d}{2}$. Then the pressure at $x = 0$ is

$$\boldsymbol{p} = \frac{\boldsymbol{p}_a + \boldsymbol{p}_b}{2}, \tag{A.7}$$

and the particle velocity is obtained from Euler's equation in one dimension as

$$\hat{\boldsymbol{u}} = \frac{j}{\rho\omega}\frac{d\boldsymbol{p}}{dx}. \tag{A.8}$$

The quantity $\frac{d\boldsymbol{p}}{dx}$ is approximated by a finite difference of

$$\frac{d\boldsymbol{p}}{dx} = \frac{\boldsymbol{p}_a - \boldsymbol{p}_b}{d}, \tag{A.9}$$

which then allows us to write Equation A.6 as

$$\hat{\boldsymbol{I}} = Re\left\{< \frac{-j}{2\rho\omega d}(\boldsymbol{p}_a\boldsymbol{p}_a^* - \boldsymbol{p}_a\boldsymbol{p}_b^* + \boldsymbol{p}_b\boldsymbol{p}_a^* - \boldsymbol{p}_b\boldsymbol{p}_b^*)\right\}\hat{\boldsymbol{x}}. \tag{A.10}$$

It is common to re-write this expression in terms of two-sided frequency domain cross-spectra.

$$\hat{\boldsymbol{I}} = \frac{1}{2\rho\omega d} Im\{2\boldsymbol{S}_{ab}\}\hat{\boldsymbol{x}}, \tag{A.11}$$

which is equivalent to

$$\hat{\boldsymbol{I}} = \frac{1}{2\rho\omega d} Im\{\boldsymbol{G}_{ab}\}\hat{\boldsymbol{x}}. \tag{A.12}$$

This formulation for acoustic intensity utilizes the single-sided cross spectrum and is not consistent through the literature. For example, in Fahy's[1] book (pg. 97), he gives the acoustic intensity as twice the value reported in Equation A.12. Gade[2] reports the same relationship as Fahy, however there appears to be a mathematical discrepancy between his equations D.12 and D.13 which should have resulted in Equation A.12. Chung[3] reports the same expression as Equation A.12. Although seemingly inconsistent, it may be that Fahy, Gade and Chung are each correct and there is simply a difference in the definition and variable notation of cross-spectral terms in terms of full and half spectrum analysis.

This result in Equation A.12 is commonly used to measure acoustic intensity in one-dimension. The limitations associated with this calculation are discussed in current literature[2,4] and it behooves the reader to become familiar with these limitations before performing the method. One of the error sources was discussed in Chapter 2 and is related to phase mismatch between the microphones at low frequencies. Other error sources at high frequencies include finite sum and finite difference errors which modify the pressure and particle velocity estimates resulting in underestimation of the active intensity vector.

A.3 3-D Acoustic intensity ($\hat{\boldsymbol{I}}_{\boldsymbol{T}}$)

For a tetrahedron that may be circumscribed by a sphere of radius a, with a microphone set at each vertex as in Figure A.2, the three-dimensional pressure gradient according to the finite-difference approximation is given by

$$\boldsymbol{\nabla p} = \begin{bmatrix} \boldsymbol{\nabla p}_x \\ \boldsymbol{\nabla p}_y \\ \boldsymbol{\nabla p}_z \end{bmatrix} = \frac{1}{4a} \begin{bmatrix} \sqrt{2}(\boldsymbol{p}_2 + \boldsymbol{p}_4 - 2\boldsymbol{p}_3) & \hat{\boldsymbol{x}} \\ \sqrt{6}(\boldsymbol{p}_4 - \boldsymbol{p}_2) & \hat{\boldsymbol{y}} \\ -(\boldsymbol{p}_2 + \boldsymbol{p}_3 + \boldsymbol{p}_4 - 3\boldsymbol{p}_1) & \hat{\boldsymbol{z}} \end{bmatrix}. \tag{A.13}$$

Alternate mathematical rotations of the same physical setup will result in slightly different weightings for each dimension[5-7]. In this analysis, we consider the orientation used by Thomas[8] in his thesis.

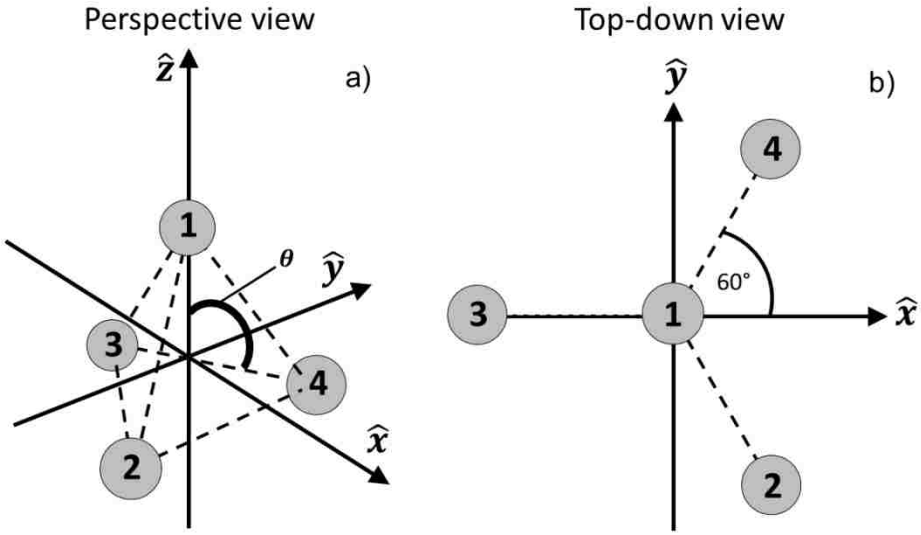

Figure A.2. This is the orientation of the regular tetrahedron used in this analysis. The tetrahedral angle of the regular tetrahedron is $\boldsymbol{\theta \approx 109.4°}$, or $\boldsymbol{\cos^{-1}(-1/3)}$.

From $\boldsymbol{\nabla p}$, we can then calculate the particle velocity

$$\hat{\boldsymbol{u}} = \begin{bmatrix} \hat{\boldsymbol{u}}_x \\ \hat{\boldsymbol{u}}_y \\ \hat{\boldsymbol{u}}_z \end{bmatrix} = \frac{j}{\rho_0 \omega} \boldsymbol{\nabla p}, \tag{A.14}$$

and the estimated pressure at the acoustic center of the microphone array is simply

$$\boldsymbol{p} = \sum_{n=1}^{4} \frac{\boldsymbol{p}_n}{4}. \tag{A.15}$$

This corresponds to an average of the pressure at each of the four microphones. For this orientation, we are attempting to calculate the acoustic intensity (and other metrics) at the acoustic "center of mass" of the microphones.

The total acoustic intensity may be defined as

$$\widehat{\boldsymbol{I}_T} = \langle \boldsymbol{p}\widehat{\boldsymbol{u}}^* \rangle, \tag{A.16}$$

where ⟨ ⟩ denotes a time-averaged quantity. The time averaging will be accounted for in the transformation of our data into the frequency domain.

Substituting Equations A.14 and A.15 into Equation A.16 yields

$$\widehat{\boldsymbol{I}_T} = \begin{bmatrix} \hat{\boldsymbol{I}}_{T_x} \\ \hat{\boldsymbol{I}}_{T_y} \\ \hat{\boldsymbol{I}}_{T_z} \end{bmatrix} = \frac{1}{j16\rho_0\omega a} \sum_{n=1}^{4} \boldsymbol{p}_n \begin{bmatrix} \sqrt{2}(\boldsymbol{p}_2^* + \boldsymbol{p}_4^* - 2\boldsymbol{p}_3^*) & \hat{\boldsymbol{x}} \\ \sqrt{6}(\boldsymbol{p}_4^* - \boldsymbol{p}_2^*) & \hat{\boldsymbol{y}} \\ -(\boldsymbol{p}_2^* + \boldsymbol{p}_3^* + \boldsymbol{p}_4^* - 3\boldsymbol{p}_1^*) & \hat{\boldsymbol{z}} \end{bmatrix}. \tag{A.17}$$

Expanding Equation A.17 and converting the products of the pressures to auto and cross spectral quantities via Equations A.3 and A.4, we arrive at

$$\begin{aligned} \widehat{\boldsymbol{I}_T} &= \begin{bmatrix} \hat{\boldsymbol{I}}_{T_x} \\ \hat{\boldsymbol{I}}_{T_y} \\ \hat{\boldsymbol{I}}_{T_z} \end{bmatrix} \\ &= \frac{1}{j16\rho_0\omega a} \left(\begin{bmatrix} 2\sqrt{2}(\boldsymbol{G}_{31} + \boldsymbol{G}_{32} + \boldsymbol{G}_{33} + \boldsymbol{G}_{34})\hat{\boldsymbol{x}} \\ \sqrt{6}(\boldsymbol{G}_{21} + \boldsymbol{G}_{22} + \boldsymbol{G}_{23} + \boldsymbol{G}_{24})\,\hat{\boldsymbol{y}} \\ 3(\boldsymbol{G}_{11} + \boldsymbol{G}_{12} + \boldsymbol{G}_{13} + \boldsymbol{G}_{14})\;\;\hat{\boldsymbol{z}} \end{bmatrix} \right. \\ &\left. - \begin{bmatrix} \sqrt{2}(\boldsymbol{G}_{21} + \boldsymbol{G}_{41} + \boldsymbol{G}_{22} + \boldsymbol{G}_{42} + \boldsymbol{G}_{23} + \boldsymbol{G}_{43} + \boldsymbol{G}_{24} + \boldsymbol{G}_{44}) & \hat{\boldsymbol{x}} \\ \sqrt{6}(\boldsymbol{G}_{41} + \boldsymbol{G}_{42} + \boldsymbol{G}_{43} + \boldsymbol{G}_{44}) & \hat{\boldsymbol{y}} \\ \boldsymbol{G}_{21} + \boldsymbol{G}_{22} + \boldsymbol{G}_{23} + \boldsymbol{G}_{24} + \boldsymbol{G}_{31} + \boldsymbol{G}_{32} + \boldsymbol{G}_{33} + \boldsymbol{G}_{34} + \boldsymbol{G}_{41} + \boldsymbol{G}_{42} + \boldsymbol{G}_{43} + \boldsymbol{G}_{44} & \hat{\boldsymbol{z}} \end{bmatrix} \right). \end{aligned} \tag{A.18}$$

A.3.1 Active intensity ($\hat{\boldsymbol{I}}$)

The real part of Equation A.17 is the active intensity and may be more simply written as

$$\hat{\boldsymbol{I}} = \begin{bmatrix} \hat{\boldsymbol{I}}_x \\ \hat{\boldsymbol{I}}_y \\ \hat{\boldsymbol{I}}_z \end{bmatrix} = \frac{1}{16\rho_0\omega a} \begin{bmatrix} \sqrt{2}(-Q_{12} + 2Q_{13} - Q_{14} + 3Q_{23} - 3Q_{34})\ \hat{\boldsymbol{x}} \\ \sqrt{6}(Q_{12} - Q_{14} - Q_{23} - 2Q_{24} - Q_{34})\ \ \hat{\boldsymbol{y}} \\ 4(Q_{12} + Q_{13} + Q_{14}) \qquad\qquad \hat{\boldsymbol{z}} \end{bmatrix}. \tag{A.19}$$

A.3.2 Reactive intensity ($\hat{\boldsymbol{Q}}$)

The imaginary part of Equation A.17 is the reactive intensity and may be written as

$$\hat{\boldsymbol{Q}} = \begin{bmatrix} \hat{\boldsymbol{Q}}_x \\ \hat{\boldsymbol{Q}}_y \\ \hat{\boldsymbol{Q}}_z \end{bmatrix}$$

$$= \frac{1}{16\rho_0\omega a} \tag{A.20}$$

$$* \begin{bmatrix} \sqrt{2}(-C_{12} + 2C_{13} - C_{14} - C_{22} + C_{23} - 2C_{24} + 2C_{33} + C_{34} - C_{44}) \quad \hat{\boldsymbol{x}} \\ \sqrt{6}(C_{12} - C_{14} + C_{22} + C_{23} - C_{34} - C_{44}) \qquad\qquad \hat{\boldsymbol{y}} \\ (3C_{11} + 2C_{12} + 2C_{13} + 2C_{14} - C_{22} - 2C_{23} - 2C_{24} - C_{33} - 2C_{34} - C_{44})\hat{\boldsymbol{z}} \end{bmatrix}.$$

A.4 Other energy-based metrics

The energy of a sound field can also be expressed in terms of the potential energy density, the kinetic energy density or a combination of the two. These quantities can be derived in a manner similar to how the expressions for active and reactive intensity were found earlier.

A.4.1 Potential energy density (E_p)

We begin with the common expression for potential energy density

$$E_P = \frac{\boldsymbol{p}^2}{2\rho_0 c^2}. \tag{A.21}$$

and substitute in Equation A.15 to find

$$E_P = \frac{1}{32\rho_0 c^2}[\boldsymbol{p}_1 + \boldsymbol{p}_2 + \boldsymbol{p}_3 + \boldsymbol{p}_4][\boldsymbol{p}_1^* + \boldsymbol{p}_2^* + \boldsymbol{p}_3^* + \boldsymbol{p}_4^*]. \tag{A.22}$$

Considering the real part of this quantity and using the auto and cross spectral relationships we can further simplify this relationship to be

$$E_P = \frac{1}{32\rho_0 c^2}[G_{11} + G_{22} + G_{33} + G_{44} + 2(C_{12} + C_{13} + C_{14} + C_{23} + C_{24} + C_{34})]. \tag{A.23}$$

A.4.2 Kinetic energy density (E_K)

The kinetic energy is based on the finite difference approximation of the particle velocity

$$E_K = \frac{\rho_0 \hat{\boldsymbol{u}}^2}{2}, \tag{A.24}$$

and as such maintains the three Cartesian components

$$\widehat{\boldsymbol{E}}_K = \begin{bmatrix} \widehat{\boldsymbol{E}}_{K_x} \\ \widehat{\boldsymbol{E}}_{K_y} \\ \widehat{\boldsymbol{E}}_{K_z} \end{bmatrix} = \frac{\rho_0}{2}\left(\frac{1}{4a\rho_0\omega}\right)^2 * \begin{bmatrix} 2(p_2 - 2p_3 + p_4) * (p_2^* - 2p_3^* + p_4^*) & \hat{\boldsymbol{x}} \\ 6(p_2 - p_4) * (p_2^* - p_4^*) & \hat{\boldsymbol{y}} \\ (p_2 + p_3 + p_4 - 3p_1) * (p_2^* + p_3^* + p_4^* - 3p_1^*) & \hat{\boldsymbol{z}} \end{bmatrix}. \tag{A.25}$$

The real part, may be expressed as

$$\widehat{\boldsymbol{E}}_K = \begin{bmatrix} \widehat{\boldsymbol{E}}_{K_x} \\ \widehat{\boldsymbol{E}}_{K_y} \\ \widehat{\boldsymbol{E}}_{K_z} \end{bmatrix} = \langle \hat{\boldsymbol{x}} \quad \hat{\boldsymbol{y}} \quad \hat{\boldsymbol{z}} \rangle \frac{\rho_0}{2}\left(\frac{1}{4a\rho_0\omega}\right)^2 * \begin{bmatrix} 2(G_{22} + 4G_{33} + G_{44} + 2C_{24} - 4C_{23} - 4C_{34}) & \hat{\boldsymbol{x}} \\ 6(G_{22} + G_{44} - 2C_{24}) & \hat{\boldsymbol{y}} \\ 9G_{11} + G_{22} + G_{33} + G_{44} - 6C_{12} + 2C_{13} + 2C_{14} + 2C_{23} + 2C_{24} + 2C_{34} & \hat{\boldsymbol{z}} \end{bmatrix}, \tag{A.26}$$

and the total kinetic energy may be found as the sum of each of the components $\widehat{\boldsymbol{E}}_{K_x}$, $\widehat{\boldsymbol{E}}_{K_y}$ and $\widehat{\boldsymbol{E}}_{K_z}$,

$$E_K = \frac{1}{32a^2\rho_0\omega^2}[9(G_{11} + G_{22} + G_{33} + G_{44}) - 6(C_{12} + C_{13} + C_{14} + C_{23} + C_{24} + C_{34})]. \quad \text{(A.27)}$$

A.4.3 Total energy density (E)

The energy density , E, of a sound field is found to be the sum of the kinetic and potential energy densities and is written as

$$E = \frac{\rho_0\hat{\boldsymbol{u}}^2}{2} + \frac{\boldsymbol{p}^2}{2\rho_0 c^2}. \quad \text{(A.28)}$$

It is simple addition of Equations A.27 and A.23 which yields

$$E = \left[\frac{1}{32\rho_0 c^2} + \frac{9}{32a^2\rho_0\omega^2}\right] * [G_{11} + G_{22} + G_{33} + G_{44}] + \left[\frac{1}{16\rho_0 c^2} - \frac{3}{16a^2\rho_0\omega^2}\right] * [C_{12} + C_{13} + C_{14} + C_{23} + C_{24} + C_{34}]. \quad \text{(A.29)}$$

A.4.4 Lagrangian energy density (E_L)

The Lagrangian energy density, E_L, is the difference between kinetic and potential energy densities and may be written simply as

$$E_L = \frac{\rho_0\hat{\boldsymbol{u}}^2}{2} - \frac{\boldsymbol{p}^2}{2\rho_0 c^2}, \quad \text{(A.30)}$$

or expanded by use of Equations A.27 and A.23 to yield

$$E_L = \left[\frac{9}{32a^2\rho_0\omega^2} - \frac{1}{32\rho_0 c^2}\right] * [G_{11} + G_{22} + G_{33} + G_{44}] - \left[\frac{1}{16\rho_0 c^2} + \frac{3}{16a^2\rho_0\omega^2}\right] * [C_{12} + C_{13} + C_{14} + C_{23} + C_{24} + C_{34}]. \quad \text{(A.31)}$$

A.5 Irregular tetrahedron spherical array

Throughout this thesis, there is made mention of a 2.54 cm spherical "SA" array. The arrangement of the microphones is slightly irregular, $\theta = 120°$, when it ought to have been $\theta = \cos^{-1}\left(-\frac{1}{3}\right) \approx 109.4°$ to be considered a "regular" tetrahedron. This slight variation modifies the approximated pressure gradient to be

$$\nabla \boldsymbol{p} = \begin{bmatrix} \nabla \boldsymbol{p}_x \\ \nabla \boldsymbol{p}_y \\ \nabla \boldsymbol{p}_z \end{bmatrix} = \frac{2}{3a} \begin{bmatrix} \left(\frac{1}{\sqrt{3}}\right)(\boldsymbol{p}_2 + \boldsymbol{p}_4 - 2\boldsymbol{p}_3)\,\hat{\boldsymbol{x}} \\ (\boldsymbol{p}_4 - \boldsymbol{p}_2)\hat{\boldsymbol{y}} \\ \left(-\frac{1}{3}\right)(\boldsymbol{p}_2 + \boldsymbol{p}_3 + \boldsymbol{p}_4 - 3\boldsymbol{p}_1)\hat{\boldsymbol{z}} \end{bmatrix} \tag{A.32}$$

To derive the full expressions for the SA array, we simply change the weighting of each; the cross-spectral terms are unchanged from the regular tetrahedral array. The resulting intensity equation is

$$\widehat{\boldsymbol{I}_T} = \begin{bmatrix} \hat{\boldsymbol{I}}_{T_x} \\ \hat{\boldsymbol{I}}_{T_y} \\ \hat{\boldsymbol{I}}_{T_z} \end{bmatrix} =$$

$$\frac{\langle \hat{x} \quad \hat{y} \quad \hat{z} \rangle}{j6\rho_0\omega a}\left(\begin{bmatrix} \left(\frac{2}{\sqrt{3}}\right)(\boldsymbol{G}_{31} + \boldsymbol{G}_{32} + \boldsymbol{G}_{33} + \boldsymbol{G}_{34})\hat{\boldsymbol{x}} \\ \boldsymbol{G}_{21} + \boldsymbol{G}_{22} + \boldsymbol{G}_{23} + \boldsymbol{G}_{24} \quad \hat{\boldsymbol{y}} \\ \boldsymbol{G}_{11} + \boldsymbol{G}_{12} + \boldsymbol{G}_{13} + \boldsymbol{G}_{14} \quad \hat{\boldsymbol{z}} \end{bmatrix} - \right. \tag{A.33}$$

$$\left. 13(\boldsymbol{G}21+\boldsymbol{G}41+\boldsymbol{G}22+\boldsymbol{G}42+\boldsymbol{G}23+\boldsymbol{G}43+\boldsymbol{G}24+\boldsymbol{G}44)\boldsymbol{G}41+\boldsymbol{G}42+\boldsymbol{G}43+\boldsymbol{G}4413(\boldsymbol{G}21+\boldsymbol{G}22 \right.$$

$$\left. +\boldsymbol{G}23+\boldsymbol{G}24+\boldsymbol{G}31+\boldsymbol{G}32+\boldsymbol{G}33+\boldsymbol{G}34+\boldsymbol{G}41+\boldsymbol{G}42+\boldsymbol{G}43+\boldsymbol{G}44)\boldsymbol{xyz}, \right.$$

with active intensity

$$\hat{\boldsymbol{I}} = \begin{bmatrix} \hat{\boldsymbol{I}}_{\boldsymbol{x}} \\ \hat{\boldsymbol{I}}_{\boldsymbol{y}} \\ \hat{\boldsymbol{I}}_{\boldsymbol{z}} \end{bmatrix} = \frac{1}{3\rho_0\omega a} \begin{bmatrix} \left(\frac{1}{2\sqrt{3}}\right)(-Q_{12} + 2Q_{13} - Q_{14} + 3Q_{23} - 3Q_{34})\hat{\boldsymbol{x}} \\ \left(\frac{1}{2}\right)(Q_{12} - Q_{14} - Q_{23} - 2Q_{24} - Q_{34})\hat{\boldsymbol{y}} \\ \left(\frac{2}{3}\right)(Q_{12} + Q_{13} + Q_{14})\hat{\boldsymbol{z}} \end{bmatrix}, \tag{A.34}$$

reactive intensity

$$\widehat{\boldsymbol{Q}} = \begin{bmatrix} \widehat{\boldsymbol{Q}}_x \\ \widehat{\boldsymbol{Q}}_y \\ \widehat{\boldsymbol{Q}}_z \end{bmatrix}$$

$$= \frac{1}{3\rho_0 \omega a} * \begin{bmatrix} \left(\frac{1}{2\sqrt{3}}\right)(-C_{12} + 2C_{13} - C_{14} - C_{22} + C_{23} - 2C_{24} + 2C_{33} + C_{34} - C_{44})\hat{\boldsymbol{x}} \\ \left(\frac{1}{2}\right)(C_{12} - C_{14} + C_{22} + C_{23} - C_{34} - C_{44})\hat{\boldsymbol{y}} \\ \left(\frac{1}{6}\right)(-3C_{11} - 2C_{12} - 2C_{13} - 2C_{14} + C_{22} + 2C_{23} + 2C_{24} + C_{33} + 2C_{34} + C_{44})\hat{\boldsymbol{z}} \end{bmatrix}, \tag{A.35}$$

potential energy density

$$E_P = \frac{1}{32\rho_0 c^2}[G_{11} + G_{22} + G_{33} + G_{44} + 2(C_{12} + C_{13} + C_{14} + C_{23} + C_{24} + C_{34})], \tag{A.36}$$

kinetic energy density

$$E_K = \frac{2}{81a^2\rho_0\omega^2}[9G_{11} + 13(G_{22} + G_{33} + G_{44}) - 6(C_{12} + C_{13} + C_{14}) - 10(C_{23} + C_{24} + C_{34})], \tag{A.37}$$

energy density

$$E = \frac{2}{81a^2\rho_0\omega^2}[9G_{11} + 13(G_{22} + G_{33} + G_{44}) - 6(C_{12} + C_{13} + C_{14}) - 10(C_{23} + C_{24} + C_{34})] + \frac{1}{32\rho_0 c^2}[G_{11} + G_{22} + G_{33} + G_{44} + 2(C_{12} + C_{13} + C_{14} + C_{23} + C_{24} + C_{34})], \tag{A.38}$$

and Lagrangian energy density

$$E_L = \frac{2}{81a^2\rho_0\omega^2}[9G_{11} + 13(G_{22} + G_{33} + G_{44}) - 6(C_{12} + C_{13} + C_{14}) - 10(C_{23} + C_{24} + C_{34})] - \frac{1}{32\rho_0 c^2}[G_{11} + G_{22} + G_{33} + G_{44} + 2(C_{12} + C_{13} + C_{14} + C_{23} + C_{24} + C_{34})]. \quad \text{(A.39)}$$

A.6 External frame array

Another style of microphone array used during solid rocket motor firings is the external frame array, or "EF". This design is a regular tetrahedron with the z-axis pointing the opposite direction of that in Figure 2. To modify the intensity expressions for this orientation, simply multiply the $\hat{\boldsymbol{z}}$ components by -1. The energy expressions remain unchanged.

A.7 Plane wave assumption

For a perfectly planar field, there are some simplifying relationships that apply. The particle velocity is equivalent to

$$\hat{\boldsymbol{u}} = \frac{\boldsymbol{p}}{\rho_0 c}; \quad \text{(A.40)}$$

this relationship implies that

$$E_{L-(plane\ wave)} = 0 \quad \text{(A.41)}$$

and

$$E_{(plane\ wave)} = \frac{\boldsymbol{p}^2}{\rho_0 c^2}, \quad \text{(A.42)}$$

which is related to the acoustic intensity of a plane wave by

$$I_{(plane\ wave)} = cE_{(plane\ wave).} \quad \text{(A.43)}$$

These relationships can be useful in determining whether or not a plane progressive wave field or an approximation thereof may exist. Approximations of these fields include far-field spherical and cylindrical wave fields where the curvature of the field appears to be "locally planar" relative to the size of the measurement apparatus. In known plane wave environment these relationships may be used to verify correct implementation of the expressions and discuss limitations of the array response.

References for appendix

[1] F. Fahy, *Sound intensity*, 2nd ed. (Spon, London ; New York, 1995).

[2] S. Gade, *Sound intensity (theory)* (Brüel & Kjaer, 1982).

[3] J. Y. Chung, "Cross-spectral method of measuring acoustic intensity without error caused by instrument phase mismatch," J. Acoust. Soc. Am **64**, 1613-1616 (1978).

[4] M. J. Crocker and J. P. Arenas, "Fundamentals of the direct measurement of sound intensity and practical applications," Acoust. Phys+ **49**, 163-175 (2003).

[5] B. S. Cazzolato and J. Ghan, "Frequency domain expressions for the estimation of time-averaged acoustic energy density," J. Acoust. Soc. Am **117**, 3750-3756 (2005).

[6] J.-C. Pascal and J.-F. Li, "A systematic method to obtain 3d finite-difference formulations for acoustic intensity and other energy quantities," J. Sound Vib. **310**, 1093-1111 (2008).

[7] C. Wiederhold, *Design and implementation of multi-microphone probes*, Brigam Young University 2011).

[8] D. C. Thomas, *Theory and estimation of acoustic intensity and energy density*, Brigham Young University 2008).

A Matlab script

This script reads data, calculates energy metrics and suggests how a calibration may be applied to the data. Proper scaling for the intensity vectors is also given.

```
clc
clear all;
close all;

% load('Calibration.mat') % Load the calibration file

fs=204800;  %sampling frequency of the data
rho=1.21;   %density of air
c=343;      %sound speed in air
numsamp=2^11; %number of samples to read in

%% This portion of the code does the main processing

for ID =[1] %Test to run, data are typically recorded as ID###_###
    for sensor=1
        %this will run ID001_000, ID001_001, ID001_002 and ID001_003
        %an entire 4-microphone array

        CH=[0+4*(sensor-1):3+4*(sensor-1)];

        testname='ID';
        for n=1:length(CH)
            histbins=101;

            if ID<10
                IDstring='00';
            elseif ID<100
                IDstring='0';
            else
                IDstring='';
            end

            if CH(n)<10
                CHstring='00';
            elseif CH(n)<100
                CHstring='0';
            else
                CHstring='';
            end

            pathname='C:\JuneGemData \';
            N=10*fs;            %How long of data set to read
            Nstart=4*(360)*fs;  %This is where the June GEM data begins
```

```
filename=[pathname,testname,IDstring,int2str(ID),'_',CHstring,int2str(CH(n)),
'.bin'];

                fid=fopen(filename,'r');
                fseek(fid,Nstart,'bof');
                x=fread(fid,N,'single');
                fclose(fid);

                N = 2^floor(log2(length(x))); %number of samples to nearest
lower power of 2
                x = x(1:N); % makes length a power of 2

                %For the spherical and 40BH arrays, the voltage must be
                %inverted
                if sensor==3||sensor==4
                    x=-x;
                end


                x=x-mean(x);

                xarr(n,:)=x;

                %                  %This portion of code can be used to check
if the data read in is valid
                %                                       t = linspace(0,(N-1)/fs,N);
                %                                       figure
                %                                       plot(t,x)
                %                                       pause

                clear x;


            end

            x1=xarr(1,:);
            x2=xarr(2,:);
            x3=xarr(3,:);
            x4=xarr(4,:);
            xavg = (x1+x2+x3+x4)/4;

            clear xarr;

            f=linspace(0,fs,numsamp);
            fss = fs*(0:numsamp/2-1)/numsamp; % freq. scale for ss fft.
ss="sigle sided";
            df = f(2) - f(1); % width of frequency bins

            wind=hann(numsamp);
```

```
            W = mean(wind.*conj(wind)); % used to scale the psd restores what
was %lost due to windowing

            numblocks=2*N/numsamp-1;

            x1block=zeros(numblocks,numsamp);
            x2block=x1block;
            x3block=x1block;
            x4block=x1block;
            xavgblock=x1block;

            x1block(1,:)=wind'.*x1(1:numsamp);
            x2block(1,:)=wind'.*x2(1:numsamp);
            x3block(1,:)=wind'.*x3(1:numsamp);
            x4block(1,:)=wind'.*x4(1:numsamp);
            xavgblock(1,:)=wind'.*xavg(1:numsamp);

            for n=2:numblocks
                x1block(n,:)=wind'.*x1((n-1)/2*numsamp:(n+1)/2*numsamp-1); %
%50 percent overlap
                x2block(n,:)=wind'.*x2((n-1)/2*numsamp:(n+1)/2*numsamp-1);
                x3block(n,:)=wind'.*x3((n-1)/2*numsamp:(n+1)/2*numsamp-1);
                x4block(n,:)=wind'.*x4((n-1)/2*numsamp:(n+1)/2*numsamp-1);
                xavgblock(n,:)=wind'.*xavg((n-1)/2*numsamp:(n+1)/2*numsamp-1);
            end

            X1=fft(x1block,numsamp,2);
            X2=fft(x2block,numsamp,2);
            X3=fft(x3block,numsamp,2);
            X4=fft(x4block,numsamp,2);

            Xmean=(X1+X2+X3+X4)/4;

            Xavg=fft(xavgblock,numsamp,2);


            X1ss=X1(:,1:floor(numsamp/2)); %takes the first half of the fft
            X2ss=X2(:,1:floor(numsamp/2));
            X3ss=X3(:,1:floor(numsamp/2));
            X4ss=X4(:,1:floor(numsamp/2));
            Xavgss=Xavg(:,1:floor(numsamp/2));

            % Here we define some values to aid in calibration
            %              fss=fss(:,1:1000);%%%%%%%%%%%%%%%%%%
            %              Cals=Cals(:,1:1000);
            %              X1ss=X1ss(:,1:1000);%%%%%%%%%%%%%%%%%%5
            %              X2ss=X2ss(:,1:1000);%%%%%%%%%%%%%%%%%%%5
            %              X3ss=X3ss(:,1:1000);%%%%%%%%%%%%%%%%%%5
            %              X4ss=X4ss(:,1:1000);%%%%%%%%%%%%%%%%%%
            %              Xavgss=Xavgss(:,1:1000);%%%%%%%%%%%%%%%%%5

            %     for n=1:size(X1ss,1)
            %         X1ssC=X1ss;
```

```
%         X2ssC(n,:)=X2ss(n,:);
%         X3ssC(n,:)=X3ss(n,:);
%         X4ssC(n,:)=X4ss(n,:);
%         XavgssC(n,:)=Xavgss(n,:);
%     end


%%%%%%%%%%%%%%%%%%%%%%%%%%%%%%%%%%%%%%%%%%%%
%%%%%%%%%%%%%%%%%%%%%%%%%%%%%%%%%%%%%%%%%%%%


mean_Xss_sq1 = mean(X1ss.*conj(X1ss),1); % Finds the mean of the
magnitude squared.
mean_Xss_sq2 = mean(X2ss.*conj(X2ss),1);
mean_Xss_sq3 = mean(X3ss.*conj(X3ss),1);
mean_Xss_sq4 = mean(X4ss.*conj(X4ss),1);
%             mean_Xss_sq1C = mean(X1ssC.*conj(X1ssC),1); % Finds
the mean of the magnitude squared.
%             mean_Xss_sq2C = mean(X2ssC.*conj(X2ssC),1);
%             mean_Xss_sq3C = mean(X3ssC.*conj(X3ssC),1);
%             mean_Xss_sq4C = mean(X4ssC.*conj(X4ssC),1);


Xssrms1 = sqrt(mean_Xss_sq1); % Finds the rms average of the
single sided ffts.
Xssrms2 = sqrt(mean_Xss_sq2);
Xssrms3 = sqrt(mean_Xss_sq3);
Xssrms4 = sqrt(mean_Xss_sq4);
%             Xssrms1C = sqrt(mean_Xss_sq1C); % Finds the rms
average of the single sided ffts.
%             Xssrms2C = sqrt(mean_Xss_sq2C);
%             Xssrms3C = sqrt(mean_Xss_sq3C);
%             Xssrms4C = sqrt(mean_Xss_sq4C);

psd1 = 2*mean_Xss_sq1/numsamp/fs/W;% See MATLAB help for
periodogram algorithm. Units are (rms amp)^2/Hz
psd2 = 2*mean_Xss_sq2/numsamp/fs/W;
psd3 = 2*mean_Xss_sq3/numsamp/fs/W;
psd4 = 2*mean_Xss_sq4/numsamp/fs/W;
psdArray(sensor,1,:)=psd1;
psdArray(sensor,2,:)=psd2;
psdArray(sensor,3,:)=psd3;
psdArray(sensor,4,:)=psd4;
%             psd1C = 2*mean_Xss_sq1C/numsamp/fs/W;%
%             psd2C = 2*mean_Xss_sq2C/numsamp/fs/W;
%             psd3C = 2*mean_Xss_sq3C/numsamp/fs/W;
%             psd4C = 2*mean_Xss_sq4C/numsamp/fs/W;
%             psdArrayC(sensor,1,:)=psd1C;
%             psdArrayC(sensor,2,:)=psd2C;
%             psdArrayC(sensor,3,:)=psd3C;
%             psdArrayC(sensor,4,:)=psd4C;
%
%             if sensor==2
%
```

```
%                 semilogx(fss,log10(mean(psd1,1)),'r')
%                 hold on;
%                 semilogx(fss,log10(mean(psd2,1)),'y')
%                 semilogx(fss,log10(mean(psd3,1)),'g')
%                 semilogx(fss,log10(mean(psd4,1)),'b')
%                 legend('X1','X2','X3','X4')
%
%                 xlim([0 10000])
%                 pause
%             end

          OASPL1 = 20*log10(sqrt(sum(psd1*df))/2e-5); %%Multiplying by df
makes the psd a power spectrum
          OASPL2 = 20*log10(sqrt(sum(psd2*df))/2e-5);
          OASPL3 = 20*log10(sqrt(sum(psd3*df))/2e-5);
          OASPL4 = 20*log10(sqrt(sum(psd4*df))/2e-5);
          OASPLArray(sensor,ID,:)=OASPL1;
          %             OASPL1C = 20*log10(sqrt(sum(psd1C*df))/2e-5);
          %             OASPL2C = 20*log10(sqrt(sum(psd2C*df))/2e-5);
          %             OASPL3C = 20*log10(sqrt(sum(psd3C*df))/2e-5);
          %             OASPL4C = 20*log10(sqrt(sum(psd4C*df))/2e-5);
          %             OASPLArrayC(sensor,ID,:)=OASPL1C;

          scale=2*df/numsamp/fs/W;

          Mic1PSq=scale*mean(conj(X1ss).*X1ss,1);
          Mic2PSq=scale*mean(conj(X2ss).*X2ss,1);
          Mic3PSq=scale*mean(conj(X3ss).*X3ss,1);
          Mic4PSq=scale*mean(conj(X4ss).*X4ss,1);
          MicAvgPSq=scale*mean(conj(Xavgss).*Xavgss,1);

MicAvgPSq2=scale*mean(sqrt(((conj(X1ss).*X1ss).^2+(conj(X2ss).*X2ss).^2+(conj
(X3ss).*X3ss).^2+(conj(X4ss).*X4ss).^2)/4));

          G11=scale*mean(conj(X1ss).*X1ss,1);
          G22=scale*mean(conj(X2ss).*X2ss,1);
          G33=scale*mean(conj(X3ss).*X3ss,1);
          G44=scale*mean(conj(X4ss).*X4ss,1);
          G12=scale*mean(conj(X1ss).*X2ss,1);
          G13=scale*mean(conj(X1ss).*X3ss,1);
          G14=scale*mean(conj(X1ss).*X4ss,1);
          G21=scale*mean(conj(X2ss).*X1ss,1);
          G23=scale*mean(conj(X2ss).*X3ss,1);
          G24=scale*mean(conj(X2ss).*X4ss,1);
          G31=scale*mean(conj(X3ss).*X1ss,1);
          G32=scale*mean(conj(X3ss).*X2ss,1);
          G34=scale*mean(conj(X3ss).*X4ss,1);
          G41=scale*mean(conj(X4ss).*X1ss,1);
          G42=scale*mean(conj(X4ss).*X2ss,1);
          G43=scale*mean(conj(X4ss).*X3ss,1);

          %             G11C=scale*mean(conj(X1ssC).*X1ssC,1);
          %             G22C=scale*mean(conj(X2ssC).*X2ssC,1);
          %             G33C=scale*mean(conj(X3ssC).*X3ssC,1);
```

```
%             G44C=scale*mean(conj(X4ssC).*X4ssC,1);
%             G12C=scale*mean(conj(X1ssC).*X2ssC,1);
%             G13C=scale*mean(conj(X1ssC).*X3ssC,1);
%             G14C=scale*mean(conj(X1ssC).*X4ssC,1);
%             G21C=scale*mean(conj(X2ssC).*X1ssC,1);
%             G23C=scale*mean(conj(X2ssC).*X3ssC,1);
%             G24C=scale*mean(conj(X2ssC).*X4ssC,1);
%             G31C=scale*mean(conj(X3ssC).*X1ssC,1);
%             G32C=scale*mean(conj(X3ssC).*X2ssC,1);
%             G34C=scale*mean(conj(X3ssC).*X4ssC,1);
%             G41C=scale*mean(conj(X4ssC).*X1ssC,1);
%             G42C=scale*mean(conj(X4ssC).*X2ssC,1);
%             G43C=scale*mean(conj(X4ssC).*X3ssC,1);


            Gavg=1/4*(G11+G22+G33+G44);
            AvgPSq=Gavg;

            a=.0254/2*3/2;  % (approximate) radius of External Frame and
spherical probe
            %% Finite Difference approximations.
            % From this point on, we won't follow the calibrated values
            % to calculate them, simply run the following equations using the
            % modified auto and cross spectrums

            %%%%% Finite Difference Method for External frame regular
            %%%%% tetrahedrons
            if sensor==1||sensor==2||sensor==4
   %active intensity
                Ixfd=1./(16*rho*(2*pi*fss)*a).*sqrt(2).*imag(-G12+2*G13-
G14+3*G23-3*G34);
                Iyfd=1./(16*rho*(2*pi*fss)*a).*sqrt(6).*imag(G12-G14-G23-
2*G24-G34);
                Izfd=1./(16*rho*(2*pi*fss)*a).*imag(-4*(G12+G13+G14));
   %reactive intensity
                Jxfd=1./(16*rho*(2*pi*fss)*a).*sqrt(2).*real(-G12+2*G13-G14-
G22+G23-2*G24+2*G33+G34-G44);
                Jyfd=1./(16*rho*(2*pi*fss)*a).*sqrt(6).*real(G12-G14+G22+G23-
G34-G44);
                Jzfd=1./(16*rho*(2*pi*fss)*a).*real(3*G11+2*G12+2*G13+2*G14-
G22-2*G23-2*G24-G33-2*G34-G44);
   %total intensity (redundant by this point)
                TIxfd=-j*sqrt(2)./(16*rho*2*pi*fss*a).*(G21-2*G31+G41+G22-
2*G32+G42+G23-2*G33+G43+G24-2*G34+G44);
                TIyfd=j*sqrt(6)./(16*rho*2*pi*fss*a).*(G21+G22+G23+G24-G41-
G42-G43-G44);
                TIzfd=-
j./(16*rho*2*pi*fss*a).*(G21+G22+G23+G24+G31+G32+G33+G34+G41+G42+G43+G44-
3*(G11+G12+G13+G14));
   %kinetic energy density
                KEx=1./(16*a^2*rho*(2*pi*fss).^2).*(G22-2*G32+G42-2*G23+4*G33-
2*G43+G24-2*G34+G44);
                KEy=6./(32*a^2*rho*(2*pi*fss).^2).*(G22-G24-G42+G44);
```

```
                KEz=1./(32*a^2*rho*(2*pi*fss).^2).*(9*G11-3*G21-3*G31-
3*G41+G22-3*G12+G32+G42-3*G13+G23+G33+G43-3*G14+G24+G34+G44);

                KE=KEx+KEy+KEz;
   %potential energy density

PE=1/(32*rho*c^2).*(G11+G12+G13+G14+G21+G22+G23+G24+G31+G32+G33+G34+G41+G42+G
43+G44);

           end

           if sensor==3 %irregular tetrahedron matching spherical arrays

                Ixfd=1./(36*rho*(2*pi*fss)*a).*2*sqrt(3).*imag(-G12+2*G13-
G14+3*G23-3*G34);
                Iyfd=1./(36*rho*(2*pi*fss)*a).*(6).*imag(G12-G14-G23-2*G24-
G34);
                Izfd=-1./(9*rho*(2*pi*fss)*a)*2.*imag((G12+G13+G14));

                Jxfd=1./(36*rho*(2*pi*fss)*a).*2*sqrt(3).*real(-G12+2*G13-G14-
G22+G23-2*G24+2*G33+G34-G44);
                Jyfd=1./(36*rho*(2*pi*fss)*a).*(6).*real(G12-G14+G22+G23-G34-
G44);
                Jzfd=1./(18*rho*(2*pi*fss)*a).*real(3*G11+2*G12+2*G13+2*G14-
G22-2*G23-2*G24-G33-2*G34-G44);

                TIxfd=-j*sqrt(3)./(18*rho*2*pi*fss*a).*(G21-2*G31+G41+G22-
2*G32+G42+G23-2*G33+G43+G24-2*G34+G44);
                TIyfd=j*3./(18*rho*2*pi*fss*a).*(G21+G22+G23+G24-G41-G42-G43-
G44);
                TIzfd=-
j*1./(18*rho*2*pi*fss*a).*(G21+G22+G23+G24+G31+G32+G33+G34+G41+G42+G43+G44-
3*(G11+G12+G13+G14));

                KEx=2./(27*a^2*rho*(2*pi*fss).^2).*(G22-2*G32+G42-2*G23+4*G33-
2*G43+G24-2*G34+G44);
                KEy=2./(9*a^2*rho*(2*pi*fss).^2).*(G22-G24-G42+G44);
                KEz=2./(81*a^2*rho*(2*pi*fss).^2).*(9*G11-3*G21-3*G31-
3*G41+G22-3*G12+G32+G42-3*G13+G23+G33+G43-3*G14+G24+G34+G44);

                KE=KEx+KEy+KEz;


PE=1/(32*rho*c^2).*(G11+G12+G13+G14+G21+G22+G23+G24+G31+G32+G33+G34+G41+G42+G
43+G44);

           end


           IfdArray(1,sensor,ID,:)=Ixfd;
           IfdArray(2,sensor,ID,:)=Iyfd;
           IfdArray(3,sensor,ID,:)=Izfd;
```

```
            JfdArray(1,sensor,ID,:)=Jxfd;
            JfdArray(2,sensor,ID,:)=Jyfd;
            JfdArray(3,sensor,ID,:)=Jzfd;

            TIfdArray(1,sensor,ID,:)=TIxfd;
            TIfdArray(2,sensor,ID,:)=TIyfd;
            TIfdArray(3,sensor,ID,:)=TIzfd;

            KExArray(sensor,ID,:)=KEx;
            KEyArray(sensor,ID,:)=KEy;
            KEzArray(sensor,ID,:)=KEz;

            KEArray(sensor,ID,:)=KE;

            PEArray(sensor,ID,:)=PE;

        end
    end
    EDArray=KEArray+PEArray;
    LEDArray=KEArray-PEArray;

    ang=22; %assumed angle of the plume that mics 2 and 4 are parallel to.
            %this rotates the angle so that plotting x and y gives the correct
            %direction

            %The total magnitude is calculated using x, y and z components of
            %acoustic intensity. For plotting vectors, I have only us the x
and
            %y components, thus giving a more accurate projection for my 2-D
            %figures. Look before you leap making 3D plots, I'm not including
            %that here.
    IfdMag=sqrt(IfdArray(1,:,:,:).^2+IfdArray(2,:,:,:).^2+IfdArray(3,:,:,:).^2
);
    IfdMag2=sqrt(IfdArray(1,:,:,:).^2+IfdArray(2,:,:,:).^2);
    JfdMag=sqrt(JfdArray(1,:,:,:).^2+JfdArray(2,:,:,:).^2+JfdArray(3,:,:,:).^2
);
    JfdMag2=sqrt(JfdArray(1,:,:,:).^2+JfdArray(2,:,:,:).^2);

    IfdAng=atan2(IfdArray(2,:,:,:), IfdArray(1,:,:,:));
    Ifdx=(IfdMag2).^(1/4).*cos(IfdAng+ang*pi/180);
    Ifdy=(IfdMag2).^(1/4).*sin(IfdAng+ang*pi/180);

    JfdAng=atan2(JfdArray(2,:,:,:), JfdArray(1,:,:,:));
    Jfdx=(JfdMag2).^(1/4).*cos(JfdAng+ang*pi/180);
    Jfdy=(JfdMag2).^(1/4).*sin(JfdAng+ang*pi/180);
```